Faculty of Science and Technology

MASTER'S THESIS

Study program/Specialization: Petroleum Engineering / Well Engineering	Spring semester, 2016 Open / ~~Restricted access~~
Writer: Trygve Alexander Carlsen Kjørslevik	………………………………………… (Writer's signature)
Faculty supervisor: Steinar Evje External supervisor(s):	
Thesis title: How to apply a two-phase model from fluid mechanics to study cell migration mechanisms	
Credits (ECTS): 30	
Key words: Chemotaxis, Keller-Segel, Cancer, Cell, Two-Phase, Numerical, Migration, Viscous, Fluid Mechanics	Pages: 84 + enclosure: 16 Stavanger, 15/06-2016 Date/year

Master's Thesis

How to apply a two-phase model from fluid mechanics to study cell migration mechanisms

Universitetet
i Stavanger

Trygve Alexander Carlsen Kjørslevik

Faculty of Science and Technology
University of Stavanger

This thesis is submitted for the degree of
Master of Science

June 2016

Acknowledgements

I would like to thank my supervisor Steinar Evje, Professor at The Department of Petroleum Engineering, not only for presenting me with a very interesting topic, but also for his excellent guidance during the writing of this thesis. Thank you!

Abstract

The classical Keller-Segel model of cell migration due to random motion and chemotaxis, has, as a result of its intuitive simplicity and ability to replicate key behavior of chemotactic populations, provided a foundation for much of the work with respect to mathematical modeling of chemotaxis. In this thesis, a generalized two-fluid version of this model, based on the works of Evje and Wen [16] and Byrne and Owen [6] will be derived using a multiphase modeling approach proposed in [6], describing how a population of cells moves through a fluid containing a diffusible chemical to which the cells are attracted. In the proposed multiphase setting, the cell and fluid are viewed upon as components of a two-phase system, and principles of mass and momentum balance are then applied to each phase, in addition to appropriate closure laws. The characteristic behavior of the model and its ability to replicate experimental observations of cancer cells made by Cheng et al. in [9] has then been investigated by performing numerical simulations with varying input parameters. Some of the key findings include that the model shows a good ability to generate spatial patterns, but compared to the experimental data in [9], the kinematic viscosity and cell compressibility had to be chosen unrealistically high and low, respectively, in order to get a good match to the experimental results. The model also shows a high sensitivity to initial data, while the choice of boundary geometry (circle or square) does not seem to have any impact on the computed solution, given that the cell phase not comes in direct contact with the boundary. Further, we found that the shear stress terms play an important role in how the solution will evolve with time, both with respect to shape and rate of change. The information attributed to these terms are however lost when using numerical solution methods such as dimensional splitting.

Table of contents

List of figures xi

List of tables xiii

Nomenclature xv

1 Introduction 1

1.1 Background 1
1.2 Objectives 2
1.3 Structure of this thesis 3

2 Mathematical Model 5

2.1 Mass Balance Equations 6
2.2 Viscous Stress Tensor 7
2.3 Momentum Balance Equations 10
2.4 The Model 13
    2.4.1 Simplified versions of the model 14
2.5 Closure laws and useful relations 15
2.6 Relation to Keller-Segel type of models 17

3 Numerical Solutions 21

3.1 Solution methods and steps in the numerical solution 21
    3.1.1 Discretization of space and time 21
    3.1.2 Steps in the numerical procedure 22
    3.1.3 Solution methods 31
3.2 Base Case 34
    3.2.1 Simulated results in one dimension 35
    3.2.2 Base case in two dimensions 38

4 Characteristic behavior of the model 43

4.1 Effect of shear stress 43

4.2 Effects of boundary geometry 47

4.3 Effect of viscosity 54

5 Relating the mathematical model to physical experiments 59

5.1 Key experimental observations 59

5.2 Non-dimensionalization 60

5.3 Input parameters and initial data 63

5.4 Simulations in 1D 65

5.5 Simulations in 2D 66

5.5.1 Method III 66

5.5.2 Method II 67

6 Discussion 71

6.1 Model characteristics 71

6.1.1 Viscous effects 71

6.1.2 Shear stress 72

6.1.3 Effect of boundary geometry 73

6.1.4 Solution methods for the 2D model 74

6.2 Observations relative to Chapter 5 74

6.2.1 Cell volume fraction 74

6.2.2 Pressure 76

7 Conclusion 79

7.1 Concluding remarks 79

7.2 Suggestions for future work 80

References 81

List of figures

2.1 Force acting on a surface element. Figure modified from [44]. 7
2.2 Illustration of the stresses in three dimensions. 8

3.1 Illustration of the domain in both space (a) and time (b) divided into smaller grid blocks. 22
3.2 Figures illustrating the numbering of **(a)** grid blocks, and **(b)** phase velocities. 23
3.3 Sparsity pattern of the coefficient matrix A for the momentum equations. . . 27
3.4 Sparsity pattern of the coefficient matrix A for the diffusion equation. 29
3.5 Illustration of the solution procedure for the dimensional splitting method. . 32
3.6 A plot of the cell volume fraction (α_c) for the base case. 35
3.7 A plot of the base case for the simplified Keller-Segel version of (2.31), found in (2.44). 36
3.8 A plot of α_c for the base case where $\varepsilon_{c,reg} = \varepsilon_{w,reg} = 0$, and where the number of time steps is $1.25 \cdot 10^7$. 37
3.9 Figures showing the evolution of α_c using the model in polar coordinates. . 38
3.10 A plot of the initial data (α_{c0}) for the two-dimensional base case. 39
3.11 Figures showing the evolution of α_c in two dimensions using Method I. . . 40
3.12 Figures showing the evolution of α_c in two dimensions using Method II. . . 41
3.13 Figures showing the evolution of α_c in two dimensions using Method III. . 42

4.1 A plot of the initial cell volume fraction given by (4.1). 44
4.2 Figures showing the evolution of α_c using Method III (no shear stresses present). 45
4.3 Figures showing the evolution of α_c using Method II (with shear stress). . . 46
4.4 Distance between circular shaped data and square boundary. 47
4.5 A plot of the circular initial data given by (4.2). 48
4.6 Figures showing the evolution of α_c for the initial data given in (4.2) on a square boundary geometry. 49

4.7 Figures showing the evolution in a for the initial data given in (4.2) on a square boundary geometry. 50
4.8 Figures showing the evolution of α_c for the initial data given in (4.2) on a circular boundary geometry. 51
4.9 A plot of the initial cell volume fraction given in (4.3). 52
4.10 Figures showing the evolution of α_c in for the initial data given in (4.3) using Method I. 53
4.11 A plot of the initial cell volume fraction for the circular case. 54
4.12 Plots for times $t = 1500\,\mathrm{s}$ (left) and $t = 2100\,\mathrm{s}$ (right) using Method I on a square domain. 56
4.13 Plots for times $t = 180\,\mathrm{s}$ (left) and $t = 240\,\mathrm{s}$ (right) using Method I with reduced viscosity on a square domain with. 56
4.14 Plots for times $t = 1500\,\mathrm{s}$ (left) and $t = 2100\,\mathrm{s}$ (right) using Method I on a circular domain. 57
4.15 Plots for times $t = 2400\,\mathrm{s}$ (left) and $t = 3000\,\mathrm{s}$ (right) using Method II on a square domain. 57
4.16 Plots for times $t = 2400\,\mathrm{s}$ (left) and $t = 3000\,\mathrm{s}$ (right) using Method II without shear stress terms, on a square domain. 58

5.1 A growing spheroid (green) and its surrounding micro-beads (red). Scale bar = 100 μm. Figure from [9]. 60
5.2 Figure showing the evolution in α_c over a time span of 30 days. 65
5.3 Figures showing the evolution in pressure, visualized in 2D (left) and 3D (right). 65
5.4 Figures showing cell migration over a time span of 30 days using Method III. 67
5.5 Figures showing the corresponding pressures after 12, 17, and 30 days using Method III. 68
5.6 Figures showing the evolution in α_c after 12, 17 and 30 days using Method II. 69
5.7 Figures showing the corresponding pressures after 12, 17, and 30 days using Method II. 70

6.1 Figures where $k = 10^3$ (left) and $k = 10^{15}$ (right). 76
6.2 Sparsity pattern of the momentum coefficient matrix, where the crosses represents elements containing ε_c or ε_w, and circles represent elements containing k. 76

List of tables

3.1 Input parameters for the base case: 34

4.1 Input parameters: 55

5.1 Characteristic parameters: 63
5.2 Physical input parameters: 64

Nomenclature

α_i	Volume fraction of phase i
$\boldsymbol{\sigma}_i$	Viscous stress tensor of phase i
$\delta\vec{F}$	Force vector
δA	Infinitesimal surface area
δ_{ij}	Kronecker delta
λ	Parameter in (2.36)
Λ_0	Parameter in (2.36)
Λ_1	Parameter in (2.36)
μ_i	Dynamic viscosity of phase i
ρ_i	Density of phase i
$\tilde{\rho}_{i0}$	Density constant for phase i
ε_i	Kinematic viscosity of phase i
$\varepsilon_{i,reg}$	Regularization parameter for phase i
$\vec{\sigma}$	Stress vector
$\vec{n}$	Unit normal vector
$\vec{u}_i$	Velocity vector for phase i
a	Chemical agent to which the cells are sensitive
c_1	Constant in (4.6)

C_i	Compressibility coefficient for phase i
D_a	Diffusion coefficient
k	Interfacial friction constant
m	Water mass
n	Cell mass
P	Pressure
s_0	Parameter in (2.37)
s_1	Parameter in (2.37)

Chapter 1

Introduction

1.1 Background

The migratory behavior of many cells and organisms in response to chemical gradients, known as *chemotaxis*, has attracted significant interest due to its critical role in a wide range of biological phenomena (see for instance [13]). In multicellular organisms, such behavior plays a crucial role [11, 21, 40, 52], for example in the healing of tumors and wounds where endothelial cells from intact vasculature migrate towards low oxygen regions, where the migratory speed and direction of motion is modulated by chemicals [3, 19].

The development of theoretical and mathematical models of chemotaxis can be dated back to the works of Patlak in the 1950s [41] and Keller and Segel in the 1970s [27, 28]. A more detailed introduction into the mathematics of the Keller–Segel (K-S) model of cell migration due to random motion and chemotaxis can be found in the paper by Horstmann [24].

As discussed by Hillen and Painter in their review article [23], the general K-S model takes the form

$$\begin{aligned} \frac{\partial u}{\partial t} &= \nabla\left(k_1(u,v)\nabla u - k_2(u,v)u\nabla v\right) + k_3(u,v) \\ \frac{\partial v}{\partial t} &= D_v\nabla^2 v + k_4(u,v) - k_5(u,v)v \end{aligned} \tag{1.1}$$

where u represents the cell (or organism) density on a given domain $\Omega \subset \mathbb{R}^n$ and v denotes the concentration of the chemical agent to which the cells are sensitive. The coefficient k_1 controls the diffusive motion of the cells (also known as *motility*), whereas k_2 and the gradient of the chemical agent ∇v controls the advective flux, describing the chemotaxis effect. Cell growth and death is controlled by k_3, whereas the production and degradation of the chemical agent v is accounted for by k_4 and k_5.

Over the years, a number of versions of the Keller-Segel model has been proposed, among others, stochastic and discrete approaches such as those in [10, 25, 35, 36, 39, 46]. It is, however, the deterministic Keller-Segel model that has become the most used method for describing chemotactic behavior in biological systems [23]. In the review by Horstmann [24], a total of five methods are considered in detail. These methods are:

- **i.** arguments based on Fourier's law and Fick's law [28],
- **ii.** biased random walk approaches [37],
- **iii.** interacting particle systems [45],
- **iv.** transport equations [1] or [22], and
- **v.** stochastic processes [41].

A more recent approach is the derivation of Keller-Segel type of models from multi-phase flow modeling, as proposed by Byrne and Owen in [6].

As the Keller-Segel type of equations exhibits the ability to capture key phenomena, intuitive nature and relative tractability compared to discrete or individual based approaches, they have become widely utilized in models for chemotaxis [23]. For example, K-S type of models have been used in situations where chemotaxis has been incorporated into the modeling of different phases of tumor growth, such as the migration of invasive cancer cells [42], tumor-induced angiogenesis [8, 34] and macrophage invasion into tumors [38].

In this thesis, a two-phase fluid version of the Keller-Segel model proposed by Evje and Wen in [16] will be investigated, and matched to experimental data of growing cancer cells in [9]. The model in [16] is based on the works of Byrne and Owen [6] (see also [4, 26]), but differs slightly as it assumes the two phases (cell and water) to be weakly compressible fluids, and also includes viscous effects.

1.2 Objectives

The main objectives of this thesis can be divided into four bullet points. These are:

- Analytically derive a mathematical two-fluid model for cell migration in $\mathbb{R}^3$, in both Cartesian and cylindrical coordinate systems.
- Relate this model to a simplified Keller-Segel type of model, taking the form of (1.1).

- Perform numerical simulations in order to study characteristic behavior of the model, as a response to change in parameters such as viscosity, shear stress[1], boundary geometry, and initial data.

- Investigate to what extent the model is able to simulate experimental behavior observed in [9], where, among other things, the growth of single cancer cells in 0.5% agarose gel and pressure estimations were recorded over a time span of 30 days.

1.3 Structure of this thesis

In the next chapter, *Mathematical Model*, the mathematical model from [16] is derived and further extended, along with listing of the associated assumptions.

In chapter 3, the procedures and methods used for numerically solving the mathematical model derived in Chapter 2 are presented, in addition to an established base case, used to compare different solution approaches to each other.

The model characteristics are then further investigated in Chapter 4 by looking at effects caused by shear stress, viscosity, boundary geometry, and initial data.

Following the analysis done in Chapter 4, the model is then rewritten in dimensionless form and fitted to experimental data from [9] in Chapter 5.

The results and observations made in Chapters 4 and 5 are then discussed in Chapter 6, before the concluding remarks and suggestions for future work are highlighted in Chapter 7.

---

[1] The term *shear stress* is further explained in section 2.2.

Chapter 2

Mathematical Model

In this chapter, the mathematical model for growth and movement of a colony of cells is derived. The derivations are based on the work of [16], although here, the model in [16] is expanded from a one dimensional case to a more general case in three dimensions, presented both in Cartesian and cylindrical coordinate systems. In addition, a more in detail description of the fundamentals and underlaying assumptions of the model are presented, along with a comprehensive comparison to other published works.

For the full model in three dimensions, a system of eight governing equations are obtained by applying mass and momentum balances to both the cell and water phase. In this system we have one mass balance equation and three momentum balance equations for each phase, where each of the momentum balance equations corresponds to one of the three spatial directions. To complete the model, a ninth equation describing the evolution of the chemical agent to which the cells are sensitive (represented by a) is added. The evolution of this chemical agent is assumed to take place only by diffusion in the water phase.

Another essential assumption in the model is that the concentration of the chemical agent affects the normal stresses[1] of the cell phase. This approach is similar to that presented in [6].

At last, the model is compared to the classical Keller-Segel type of models [27], by imposing simplifying assumptions such as no viscosity terms and incompressible fluids.

---

[1] The term *normal stress* is further explained in section 2.2

2.1 Mass Balance Equations

By applying mass balance to the cell and water phase, and assuming that mass is conserved at all times (i.e. no source/sink term), we obtain

$$\frac{\partial}{\partial t}(\alpha_c\rho_c) + \nabla \cdot (\alpha_c\rho_c\vec{u}_c) = 0 \tag{2.1}$$

for the cell phase, and

$$\frac{\partial}{\partial t}(\alpha_w\rho_w) + \nabla \cdot (\alpha_w\rho_w\vec{u}_w) = 0 \tag{2.2}$$

for the water phase. Here, α_c and α_w is the volume fraction of the cell and water phase respectively, ρ_c and ρ_w are the corresponding densities, and $\vec{u}_c$, $\vec{u}_w$ the corresponding velocity vectors, each with components in the x, y, and z-direction, $\vec{u}_c = [u_c^x, u_c^y, u_c^z]$, $\vec{u}_w = [u_w^x, u_w^y, u_w^z]$.

By introducing the notation

$$n = \alpha_c\rho_c, \qquad m = \alpha_w\rho_w,$$

Equations (2.1) and (2.2) can be written as

$$\frac{\partial n}{\partial t} + \nabla \cdot (n\vec{u}_c) = 0 \tag{2.3}$$

$$\frac{\partial m}{\partial t} + \nabla \cdot (m\vec{u}_w) = 0. \tag{2.4}$$

In addition, we assume that the cells and water form a continuous material with no void space, leading to the fundamental relation

$$\alpha_c + \alpha_w = 1, \tag{2.5}$$

which is consistent with, among others, [4, 5, 7, 49].

For the chemical agent (a), we suppose that, once it is in the water phase, it can not cross the cells' membranes, and that it moves by diffusion in the water phase only. An appropriately chosen source term also has to be added, in order to account for production of the chemical by the cells. The evolution of the diffusible chemical can then be described by the following equation

$$\frac{\partial a}{\partial t} = D_a\nabla^2 a + S_a(a,n), \tag{2.6}$$

where D_a is the diffusion coefficient of the chemical in water, and S_a is the source term, which in other words describe the net rate at which the chemical is produced by the cells.

2.2 Viscous Stress Tensor

In short, stress can be described as a physical quantity that expresses the internal forces that neighboring particles of a continuous material (here, a fluid) exert on each other [51]. For instance, consider Fig. 2.1, where a small fluid surface element which is centered at the point $\vec{r}$, defined by its outward unit normal vector $\vec{n}$ and by its area δA, where the prefix δ indicates a very small but finite quantity, has been sketched. The resulting stress that is exerted by the fluid particles on the surface element, is then defined as

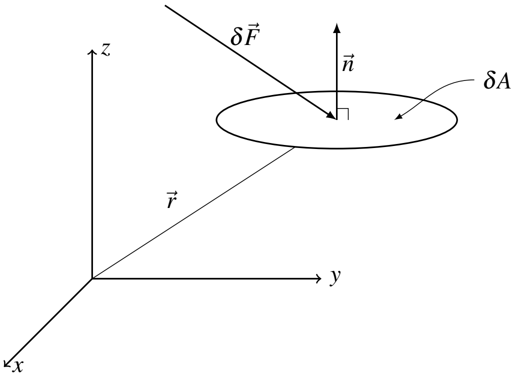

Fig. 2.1. Force acting on a surface element. Figure modified from [44].

$$\vec{\sigma} = \lim_{\delta A \to 0} \frac{\delta \vec{F}}{\delta A} \tag{2.7}$$

where $\vec{\sigma}$ is the stress vector and $\delta\vec{F}$ is the force exerted onto the surface element by the fluid [44]. Note that here, only one side of the surface element is involved, and that is the side towards which $\vec{n}$ points.

In order to fully describe the stress state at a point in each of the two phases, cell and water, the viscous stress tensor ($\boldsymbol{\sigma}$) is introduced. In three dimensions this tensor consists of nine components, and can be written as

$$\boldsymbol{\sigma} = \begin{pmatrix} \tau_{xx} & \tau_{xy} & \tau_{xz} \\ \tau_{yx} & \tau_{yy} & \tau_{yz} \\ \tau_{zx} & \tau_{zy} & \tau_{zz} \end{pmatrix},$$

where the components on the main diagonal, i.e. τ_{xx}, τ_{yy}, and τ_{zz} are known as *normal* stresses, while all the other components are *shear* stresses. By applying Newton's law to an infinitesimal fluid particle and neglecting external body forces, we find that the stress tensor is symmetric, i.e. that, $\tau_{ij} = \tau_{ji}$ for $i \neq j$, and hence, the stress tensor only has *six independent components*. Using tensor notation, each component in the stress tensor can be written as τ_{ij}, where the subscripts i and j can take any of the values 1, 2, or 3, corresponding to the x, y, and z-axis, respectively. The subscript i identifies the axis normal to the respective surface, while the subscript j corresponds to the direction of the force [18]. This is illustrated in Fig. 2.2 where the nine components of the stress tensor are sketched.

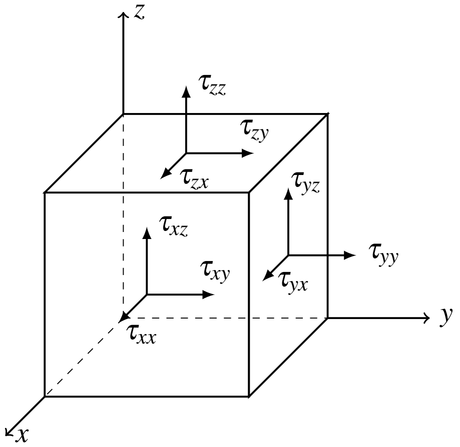

Fig. 2.2. Illustration of the stresses in three dimensions.

An essential assumption in this model is that the normal stresses in the cell phase are influenced by the concentration of the chemical agent. Similarly to [6], this is done by introducing the term $\Lambda = \Lambda(a)$, which describes more precisely how the cells will be affected by the presence of the chemical a.

Assuming that the fluids are weakly compressible, and that they exert behavior similar to that of Newtonian fluids, the components of the stress tensor can, in Cartesian coordinates, be written as

$$\tau_{ij} = -(P+\Lambda)\delta_{ij} + \mu_c \left(\frac{\partial u_c^i}{\partial x_j} + \frac{\partial u_c^j}{\partial x_i} \right) \tag{2.8}$$

for the cell phase, and

$$\tau_{ij} = -P\delta_{ij} + \mu_w \left(\frac{\partial u_w^i}{\partial x_j} + \frac{\partial u_w^j}{\partial x_i} \right) \tag{2.9}$$

for the water phase, where P is the pressure, μ_c and μ_w is the dynamic viscosity of cells and water respectively, and δ_{ij} is the Kronecker delta.

It should be noted, however, that choosing to identify the cell fluid as a Newtonian fluid is arbitrary, and that other rheology models (e.g. the Bingham model) might be more physically correct (see discussion in [17] on page 40).

In a cylindrical coordinate system (r, θ, z) the viscous stress tensor takes the form

$$\boldsymbol{\sigma} = \begin{pmatrix} \tau_{rr} & \tau_{r\theta} & \tau_{rz} \\ \tau_{\theta r} & \tau_{\theta\theta} & \tau_{\theta z} \\ \tau_{zr} & \tau_{z\theta} & \tau_{zz} \end{pmatrix}$$

where the components are

$$\begin{aligned} \tau_{rr} &= -(P+\Lambda) + 2\mu_c \frac{\partial u_c^r}{\partial r} \\ \tau_{\theta\theta} &= -(P+\Lambda) + 2\mu_c \left(\frac{1}{r}\frac{\partial u_c^\theta}{\partial \theta} + \frac{u_c^r}{r} \right) \\ \tau_{zz} &= -(P+\Lambda) + 2\mu_c \frac{\partial u_c^z}{\partial z} \\ \tau_{r\theta} = \tau_{\theta r} &= \mu_c \left[r \frac{\partial}{\partial r}\left(\frac{u_c^\theta}{r} \right) + \frac{1}{r}\frac{\partial u_c^r}{\partial \theta} \right] \\ \tau_{\theta z} = \tau_{z\theta} &= \mu_c \left(\frac{\partial u_c^\theta}{\partial z} + \frac{1}{r}\frac{\partial u_c^z}{\partial \theta} \right) \\ \tau_{rz} = \tau_{zr} &= \mu_c \left(\frac{\partial u_c^r}{\partial z} + \frac{\partial u_c^z}{\partial r} \right) \end{aligned} \tag{2.10}$$

for the cell phase, and

$$
\begin{aligned}
\tau_{rr} &= -P + 2\mu_w \frac{\partial u_w^r}{\partial r} \\
\tau_{\theta\theta} &= -P + 2\mu_w \left(\frac{1}{r}\frac{\partial u_w^\theta}{\partial \theta} + \frac{u_w^r}{r} \right) \\
\tau_{zz} &= -P + 2\mu_w \frac{\partial u_w^z}{\partial z} \\
\tau_{r\theta} = \tau_{\theta r} &= \mu_w \left[r\frac{\partial}{\partial r}\left(\frac{u_w^\theta}{r} \right) + \frac{1}{r}\frac{\partial u_w^r}{\partial \theta} \right] \\
\tau_{\theta z} = \tau_{z\theta} &= \mu_w \left(\frac{\partial u_w^\theta}{\partial z} + \frac{1}{r}\frac{\partial u_w^z}{\partial \theta} \right) \\
\tau_{rz} = \tau_{zr} &= \mu_w \left(\frac{\partial u_w^r}{\partial z} + \frac{\partial u_w^z}{\partial r} \right)
\end{aligned}
\tag{2.11}
$$

for the water phase.

For a more in depth discussion of the viscous stress tensor and its components, see for example [2, 31, 32].

2.3 Momentum Balance Equations

Assuming that no external body forces are present, and by neglecting inertial effects, the general momentum equations for the cell and water phase can be written as

$$\nabla \cdot (\alpha_c \boldsymbol{\sigma_c}) + \vec{F}_{cw} + P\nabla\alpha_c = 0 \tag{2.12}$$

$$\nabla \cdot (\alpha_w \boldsymbol{\sigma_w}) - \vec{F}_{cw} + P\nabla\alpha_w = 0 \tag{2.13}$$

where $\vec{F}_{cw}$ represents the drag force exerted by the water phase on the cells, alternatively expressed as

$$\vec{F}_{cw} = \hat{k}(\vec{u}_w - \vec{u}_c).$$

In the following, the drag coefficient $\hat{k}$ is chosen to take the general form[2]

$$\hat{k} = k\frac{nm}{n+m}, \qquad k > 0 \tag{2.14}$$

where k is a positive constant. This choice of $\hat{k}$ is consistent with that used in [6, 26]. The terms $P\nabla\alpha_c$ and $P\nabla\alpha_w$ are interfacial forces that arise from the averaging process (see [12]

---

[2] As far as the choice of $\hat{k}$ goes, many options seems possible, depending on the setting of the model. The idea in this case is simply to make sure that $\hat{k}$ will become zero as one of the phases vanishes.

for details). Combining (2.12) and (2.13) with the corresponding stress tensors from Section 2.2, and by assuming that the dynamic viscosity depend linearly on densities as given by

$$\mu_c = \varepsilon_c \rho_c, \qquad \mu_w = \varepsilon_w \rho_w,$$

where the kinematic viscosities ε_c and ε_w are positive constants, we get the following momentum equations

$$\begin{aligned} \alpha_c \frac{\partial P}{\partial x} + \frac{\partial}{\partial x}[\alpha_c \Lambda] = \hat{k}(u_w^x - u_c^x) + 2\varepsilon_c \frac{\partial}{\partial x}\left(n \frac{\partial u_c^x}{\partial x}\right) + \varepsilon_c \frac{\partial}{\partial y}\left(n\left(\frac{\partial u_c^x}{\partial y} + \frac{\partial u_c^y}{\partial x}\right)\right) \\ + \varepsilon_c \frac{\partial}{\partial z}\left(n\left(\frac{\partial u_c^x}{\partial z} + \frac{\partial u_c^z}{\partial x}\right)\right) \end{aligned} \tag{2.15}$$

$$\begin{aligned} \alpha_c \frac{\partial P}{\partial y} + \frac{\partial}{\partial y}[\alpha_c \Lambda] = \hat{k}(u_w^y - u_c^y) + 2\varepsilon_c \frac{\partial}{\partial y}\left(n \frac{\partial u_c^y}{\partial y}\right) + \varepsilon_c \frac{\partial}{\partial x}\left(n\left(\frac{\partial u_c^x}{\partial y} + \frac{\partial u_c^y}{\partial x}\right)\right) \\ + \varepsilon_c \frac{\partial}{\partial z}\left(n\left(\frac{\partial u_c^y}{\partial z} + \frac{\partial u_c^z}{\partial y}\right)\right) \end{aligned} \tag{2.16}$$

$$\begin{aligned} \alpha_c \frac{\partial P}{\partial z} + \frac{\partial}{\partial z}[\alpha_c \Lambda] = \hat{k}(u_w^z - u_c^z) + 2\varepsilon_c \frac{\partial}{\partial z}\left(n \frac{\partial u_c^z}{\partial z}\right) + \varepsilon_c \frac{\partial}{\partial x}\left(n\left(\frac{\partial u_c^x}{\partial z} + \frac{\partial u_c^z}{\partial x}\right)\right) \\ + \varepsilon_c \frac{\partial}{\partial y}\left(n\left(\frac{\partial u_c^y}{\partial z} + \frac{\partial u_c^z}{\partial y}\right)\right) \end{aligned} \tag{2.17}$$

for the cell phase, and

$$\begin{aligned} \alpha_w \frac{\partial P}{\partial x} = -\hat{k}(u_w^x - u_c^x) + 2\varepsilon_w \frac{\partial}{\partial x}\left(m \frac{\partial u_w^x}{\partial x}\right) + \varepsilon_w \frac{\partial}{\partial y}\left(m\left(\frac{\partial u_w^x}{\partial y} + \frac{\partial u_w^y}{\partial x}\right)\right) \\ + \varepsilon_w \frac{\partial}{\partial z}\left(m\left(\frac{\partial u_w^x}{\partial z} + \frac{\partial u_w^z}{\partial x}\right)\right) \end{aligned} \tag{2.18}$$

$$\begin{aligned} \alpha_w \frac{\partial P}{\partial y} = -\hat{k}(u_w^y - u_c^y) + 2\varepsilon_w \frac{\partial}{\partial y}\left(m \frac{\partial u_w^y}{\partial y}\right) + \varepsilon_w \frac{\partial}{\partial x}\left(m\left(\frac{\partial u_w^x}{\partial y} + \frac{\partial u_w^y}{\partial x}\right)\right) \\ + \varepsilon_w \frac{\partial}{\partial z}\left(m\left(\frac{\partial u_w^y}{\partial z} + \frac{\partial u_w^z}{\partial y}\right)\right) \end{aligned} \tag{2.19}$$

$$\begin{aligned} \alpha_w \frac{\partial P}{\partial z} = -\hat{k}(u_w^z - u_c^z) + 2\varepsilon_w \frac{\partial}{\partial z}\left(m \frac{\partial u_w^z}{\partial z}\right) + \varepsilon_w \frac{\partial}{\partial x}\left(m\left(\frac{\partial u_w^x}{\partial z} + \frac{\partial u_w^z}{\partial x}\right)\right) \\ + \varepsilon_w \frac{\partial}{\partial y}\left(m\left(\frac{\partial u_w^y}{\partial z} + \frac{\partial u_w^z}{\partial y}\right)\right) \end{aligned} \tag{2.20}$$

for the water phase.

Performing the same operation as above, but now using the cylindrical stress tensor components along with the del operator in cylindrical coordinates, we obtain the following momentum balance equations:

$$\begin{aligned}\frac{\partial}{\partial r}[\alpha_c\Lambda(a)]+\alpha_c\frac{\partial P}{\partial r}&=\hat{k}(u_w^r-u_c^r)+2\varepsilon_c\frac{\partial}{\partial r}\left(n\frac{\partial u_c^r}{\partial r}\right)+\frac{\varepsilon_c}{r}\frac{\partial}{\partial\theta}\left(n\left[r\frac{\partial}{\partial r}\left(\frac{u_c^\theta}{r}\right)+\frac{1}{r}\frac{\partial u_c^r}{\partial\theta}\right]\right)\\&\quad+\varepsilon_c\frac{\partial}{\partial z}\left(n\left[\frac{\partial u_c^r}{\partial z}+\frac{\partial u_c^z}{\partial r}\right]\right)+\frac{2\varepsilon_c n}{r}\left(r\frac{\partial}{\partial r}\left(\frac{u_c^r}{r}\right)-\frac{1}{r}\frac{\partial u_c^\theta}{\partial\theta}\right)\end{aligned}\tag{2.21}$$

$$\begin{aligned}\frac{1}{r}\frac{\partial}{\partial\theta}[\alpha_c\Lambda(a)]+\frac{\alpha_c}{r}\frac{\partial P}{\partial\theta}&=\hat{k}(u_w^\theta-u_c^\theta)+\frac{2\varepsilon_c}{r}\frac{\partial}{\partial\theta}\left(n\left[\frac{1}{r}\frac{\partial u_c^\theta}{\partial\theta}+\frac{u_c^r}{r}\right]\right)\\&\quad+\varepsilon_c\frac{\partial}{\partial r}\left(n\left[r\frac{\partial}{\partial r}\left(\frac{u_c^\theta}{r}\right)+\frac{1}{r}\frac{\partial u_c^r}{\partial\theta}\right]\right)+\varepsilon_c\frac{\partial}{\partial z}\left(n\left[\frac{\partial u_c^\theta}{\partial z}+\frac{1}{r}\frac{\partial u_c^z}{\partial\theta}\right]\right)\\&\quad+\frac{2\varepsilon_c n}{r}\left(r\frac{\partial}{\partial r}\left(\frac{u_c^\theta}{r}\right)+\frac{1}{r}\frac{\partial u_c^r}{\partial\theta}\right)\end{aligned}\tag{2.22}$$

$$\begin{aligned}\frac{\partial}{\partial z}[\alpha_c\Lambda(a)]+\alpha_c\frac{\partial P}{\partial z}&=\hat{k}(u_w^z-u_c^z)+2\varepsilon_c\frac{\partial}{\partial z}\left(n\frac{\partial u_c^z}{\partial z}\right)+\varepsilon_c\frac{\partial}{\partial r}\left(n\left[\frac{\partial u_c^r}{\partial z}+\frac{\partial u_c^z}{\partial r}\right]\right)\\&\quad+\frac{\varepsilon_c}{r}\frac{\partial}{\partial\theta}\left(n\left[\frac{\partial u_c^\theta}{\partial z}+\frac{1}{r}\frac{\partial u_c^z}{\partial\theta}\right]\right)+\frac{\varepsilon_c n}{r}\left(\frac{\partial u_c^r}{\partial z}+\frac{\partial u_c^z}{\partial r}\right)\end{aligned}\tag{2.23}$$

for the cell phase, and

$$\begin{aligned}\alpha_w\frac{\partial P}{\partial r}&=-\hat{k}(u_w^r-u_c^r)+2\varepsilon_w\frac{\partial}{\partial r}\left(m\frac{\partial u_w^r}{\partial r}\right)+\frac{\varepsilon_w}{r}\frac{\partial}{\partial\theta}\left(m\left[r\frac{\partial}{\partial r}\left(\frac{u_w^\theta}{r}\right)+\frac{1}{r}\frac{\partial u_w^r}{\partial\theta}\right]\right)\\&\quad+\varepsilon_w\frac{\partial}{\partial z}\left(m\left[\frac{\partial u_w^r}{\partial z}+\frac{\partial u_w^z}{\partial r}\right]\right)+\frac{2\varepsilon_w m}{r}\left(r\frac{\partial}{\partial r}\left(\frac{u_w^r}{r}\right)-\frac{1}{r}\frac{\partial u_w^\theta}{\partial\theta}\right)\end{aligned}\tag{2.24}$$

$$\begin{aligned}\frac{\alpha_w}{r}\frac{\partial P}{\partial\theta}&=-\hat{k}(u_w^\theta-u_c^\theta)+\frac{2\varepsilon_w}{r}\frac{\partial}{\partial\theta}\left(m\left[\frac{1}{r}\frac{\partial u_w^\theta}{\partial\theta}+\frac{u_w^r}{r}\right]\right)+\varepsilon_w\frac{\partial}{\partial r}\left(m\left[r\frac{\partial}{\partial r}\left(\frac{u_w^\theta}{r}\right)+\frac{1}{r}\frac{\partial u_w^r}{\partial\theta}\right]\right)\\&\quad+\varepsilon_w\frac{\partial}{\partial z}\left(m\left[\frac{\partial u_w^\theta}{\partial z}+\frac{1}{r}\frac{\partial u_w^z}{\partial\theta}\right]\right)+\frac{2\varepsilon_w m}{r}\left(r\frac{\partial}{\partial r}\left(\frac{u_w^\theta}{r}\right)+\frac{1}{r}\frac{\partial u_w^r}{\partial\theta}\right)\end{aligned}\tag{2.25}$$

$$\begin{aligned}\alpha_w\frac{\partial P}{\partial z}&=-\hat{k}(u_w^z-u_c^z)+2\varepsilon_w\frac{\partial}{\partial z}\left(m\frac{\partial u_w^z}{\partial z}\right)+\varepsilon_w\frac{\partial}{\partial r}\left(m\left[\frac{\partial u_w^r}{\partial z}+\frac{\partial u_w^z}{\partial r}\right]\right)\\&\quad+\frac{\varepsilon_w}{r}\frac{\partial}{\partial\theta}\left(m\left[\frac{\partial u_w^\theta}{\partial z}+\frac{1}{r}\frac{\partial u_w^z}{\partial\theta}\right]\right)+\frac{\varepsilon_w m}{r}\left(\frac{\partial u_w^r}{\partial z}+\frac{\partial u_w^z}{\partial r}\right)\end{aligned}\tag{2.26}$$

for the water phase.

2.4 The Model

As a summary of the sections above, the full model for a three dimensional case in Cartesian coordinates can be written as

$$
\begin{gathered}
\frac{\partial n}{\partial t} + \nabla \cdot (n\vec{u}_c) = 0 \\
\frac{\partial m}{\partial t} + \nabla \cdot (m\vec{u}_w) = 0 \\
\frac{\partial}{\partial x}[\alpha_c \Lambda] + \alpha_c \frac{\partial P}{\partial x} = \hat{k}(u_w^x - u_c^x) + 2\varepsilon_c \frac{\partial}{\partial x}\left(n \frac{\partial u_c^x}{\partial x}\right) + \varepsilon_c \frac{\partial}{\partial y}\left(n\left(\frac{\partial u_c^x}{\partial y} + \frac{\partial u_c^y}{\partial x}\right)\right) + \varepsilon_c \frac{\partial}{\partial z}\left(n\left(\frac{\partial u_c^x}{\partial z} + \frac{\partial u_c^z}{\partial x}\right)\right) \\
\frac{\partial}{\partial y}[\alpha_c \Lambda] + \alpha_c \frac{\partial P}{\partial y} = \hat{k}(u_w^y - u_c^y) + 2\varepsilon_c \frac{\partial}{\partial y}\left(n \frac{\partial u_c^y}{\partial y}\right) + \varepsilon_c \frac{\partial}{\partial x}\left(n\left(\frac{\partial u_c^x}{\partial y} + \frac{\partial u_c^y}{\partial x}\right)\right) + \varepsilon_c \frac{\partial}{\partial z}\left(n\left(\frac{\partial u_c^y}{\partial z} + \frac{\partial u_c^z}{\partial y}\right)\right) \\
\frac{\partial}{\partial z}[\alpha_c \Lambda] + \alpha_c \frac{\partial P}{\partial z} = \hat{k}(u_w^z - u_c^z) + 2\varepsilon_c \frac{\partial}{\partial z}\left(n \frac{\partial u_c^z}{\partial z}\right) + \varepsilon_c \frac{\partial}{\partial x}\left(n\left(\frac{\partial u_c^x}{\partial z} + \frac{\partial u_c^z}{\partial x}\right)\right) + \varepsilon_c \frac{\partial}{\partial y}\left(n\left(\frac{\partial u_c^y}{\partial z} + \frac{\partial u_c^z}{\partial y}\right)\right) \\
\alpha_w \frac{\partial P}{\partial x} = -\hat{k}(u_w^x - u_c^x) + 2\varepsilon_w \frac{\partial}{\partial x}\left(m \frac{\partial u_w^x}{\partial x}\right) + \varepsilon_w \frac{\partial}{\partial y}\left(m\left(\frac{\partial u_w^x}{\partial y} + \frac{\partial u_w^y}{\partial x}\right)\right) + \varepsilon_w \frac{\partial}{\partial z}\left(m\left(\frac{\partial u_w^x}{\partial z} + \frac{\partial u_w^z}{\partial x}\right)\right) \\
\alpha_w \frac{\partial P}{\partial y} = -\hat{k}(u_w^y - u_c^y) + 2\varepsilon_w \frac{\partial}{\partial y}\left(m \frac{\partial u_w^y}{\partial y}\right) + \varepsilon_w \frac{\partial}{\partial x}\left(m\left(\frac{\partial u_w^x}{\partial y} + \frac{\partial u_w^y}{\partial x}\right)\right) + \varepsilon_w \frac{\partial}{\partial z}\left(m\left(\frac{\partial u_w^y}{\partial z} + \frac{\partial u_w^z}{\partial y}\right)\right) \\
\alpha_w \frac{\partial P}{\partial z} = -\hat{k}(u_w^z - u_c^z) + 2\varepsilon_w \frac{\partial}{\partial z}\left(m \frac{\partial u_w^z}{\partial z}\right) + \varepsilon_w \frac{\partial}{\partial x}\left(m\left(\frac{\partial u_w^x}{\partial z} + \frac{\partial u_w^z}{\partial x}\right)\right) + \varepsilon_w \frac{\partial}{\partial y}\left(m\left(\frac{\partial u_w^y}{\partial z} + \frac{\partial u_w^z}{\partial y}\right)\right) \\
\frac{\partial a}{\partial t} = D_a \nabla^2 a + S_a(a,n)
\end{gathered}
\tag{2.27}
$$

where the domain in consideration is $[0,0,0] \times [L_x, L_y, L_z]$.

The boundary conditions are given as no-flux conditions:

$$
\begin{aligned}
u_l(x=0,y,z,t) = u_l(x,y=0,z,t) = u_l(x,y,z=0,t) = 0 \\
u_l(x=L_x,y,z,t) = u_l(x,y=L_y,z,t) = u_l(x,y,z=L_z,t) = 0, \qquad l = c,w \\
\frac{\partial}{\partial x}a(x=0,y,z,t) = \frac{\partial}{\partial y}a(x,y=0,z,t) = \frac{\partial}{\partial z}a(x,y,z=0,t) = 0 \\
\frac{\partial}{\partial x}a(x=L_x,y,z,t) = \frac{\partial}{\partial y}a(x,y=L_y,z,t) = \frac{\partial}{\partial z}a(x,y,z=L_z,t) = 0
\end{aligned}
\tag{2.28}
$$

with the corresponding initial data

$$
\begin{aligned}
&n(x,y,z,t=0) = n_0(x,y,z), \qquad m(x,y,z,t=0) = m_0(x,y,z), \\
&a(x,y,z,t=0) = a_0(x,y,z).
\end{aligned}
\tag{2.29}
$$

2.4.1 Simplified versions of the model

In Chapters 3 to 5, numerical simulations are performed using simplified versions of (2.27). The model is simplified in the sense that it is reduced to one and two dimensions in the Cartesian coordinate system (x, y), and to one dimension in the cylindrical coordinate system (r). For reference, the model in two-dimensional Cartesian coordinates can be written as

$$\begin{aligned}
\frac{\partial n}{\partial t} + \nabla \cdot (n\vec{u}_c) &= 0\\
\frac{\partial m}{\partial t} + \nabla \cdot (m\vec{u}_w) &= 0\\
\frac{\partial}{\partial x}[\alpha_c \Lambda(a)] + \alpha_c \frac{\partial P}{\partial x} &= \hat{k}(u_w^x - u_c^x) + 2\varepsilon_c \frac{\partial}{\partial x}\left(n\frac{\partial u_c^x}{\partial x}\right) + \varepsilon_c \frac{\partial}{\partial y}\left(n\left(\frac{\partial u_c^x}{\partial y} + \frac{\partial u_c^y}{\partial x}\right)\right)\\
\frac{\partial}{\partial y}[\alpha_c \Lambda(a)] + \alpha_c \frac{\partial P}{\partial y} &= \hat{k}(u_w^y - u_c^y) + 2\varepsilon_c \frac{\partial}{\partial y}\left(n\frac{\partial u_c^y}{\partial y}\right) + \varepsilon_c \frac{\partial}{\partial x}\left(n\left(\frac{\partial u_c^x}{\partial y} + \frac{\partial u_c^y}{\partial x}\right)\right)\\
\alpha_w \frac{\partial P}{\partial x} &= -\hat{k}(u_w^x - u_c^x) + 2\varepsilon_w \frac{\partial}{\partial x}\left(m\frac{\partial u_w^x}{\partial x}\right) + \varepsilon_w \frac{\partial}{\partial y}\left(m\left(\frac{\partial u_w^x}{\partial y} + \frac{\partial u_w^y}{\partial x}\right)\right)\\
\alpha_w \frac{\partial P}{\partial y} &= -\hat{k}(u_w^y - u_c^y) + 2\varepsilon_w \frac{\partial}{\partial y}\left(m\frac{\partial u_w^y}{\partial y}\right) + \varepsilon_w \frac{\partial}{\partial x}\left(m\left(\frac{\partial u_w^x}{\partial y} + \frac{\partial u_w^y}{\partial x}\right)\right)\\
\frac{\partial a}{\partial t} &= D_a \nabla^2 a + S_a(a,n)
\end{aligned} \tag{2.30}$$

where $\vec{u}_l = [u_l^x, u_l^y]$, $l = c, w$.

The model in one dimension takes the form

$$\begin{aligned}
\frac{\partial n}{\partial t} + \frac{\partial}{\partial x}(nu_c) &= 0\\
\frac{\partial m}{\partial t} + \frac{\partial}{\partial x}(mu_w) &= 0\\
\frac{\partial}{\partial x}[\alpha_c \Lambda(a)] + \alpha_c \frac{\partial P}{\partial x} &= \hat{k}(u_w - u_c) + 2\varepsilon_c \frac{\partial}{\partial x}\left(n\frac{\partial u_c}{\partial x}\right)\\
\alpha_w \frac{\partial P}{\partial x} &= -\hat{k}(u_w - u_c) + 2\varepsilon_w \frac{\partial}{\partial x}\left(m\frac{\partial u_w}{\partial x}\right)\\
\frac{\partial a}{\partial t} &= D_a \frac{\partial^2 a}{\partial x^2} + S_a(a,n)
\end{aligned} \tag{2.31}$$

in Cartesian coordinates, and

$$\begin{aligned}
\frac{\partial n}{\partial t} + \frac{1}{r}\frac{\partial}{\partial r}(r n u_c) &= 0 \\
\frac{\partial m}{\partial t} + \frac{1}{r}\frac{\partial}{\partial r}(r m u_w) &= 0 \\
\frac{\partial}{\partial r}\left[\alpha_c \Lambda(a)\right] + \alpha_c \frac{\partial P}{\partial r} &= \hat{k}(u_w^r - u_c^r) + 2\varepsilon_c \frac{\partial}{\partial r}\left(n \frac{\partial u_c^r}{\partial r}\right) + 2\varepsilon_c n \frac{\partial}{\partial r}\left(\frac{u_c^r}{r}\right) \\
\alpha_w \frac{\partial P}{\partial r} &= -\hat{k}(u_w^r - u_c^r) + 2\varepsilon_w \frac{\partial}{\partial r}\left(m \frac{\partial u_w^r}{\partial r}\right) + 2\varepsilon_w m \frac{\partial}{\partial r}\left(\frac{u_w^r}{r}\right) \\
\frac{\partial a}{\partial t} &= D_a \frac{1}{r}\frac{\partial}{\partial r}\left(r \frac{\partial a}{\partial r}\right) + S_a(a,n)
\end{aligned} \tag{2.32}$$

in cylindrical coordinates.
The boundary conditions and initial state are equivalent to those in (2.28) and (2.29).

2.5 Closure laws and useful relations

In order to be able to solve the models listed in the previous section, we need to add some closure laws so that the number of unknowns and equations is the same.

The cells and water are modeled as weakly compressible fluids represented by pressure-density relations of the form

$$\rho_c - \tilde{\rho}_{c0} = \frac{P}{C_c}, \qquad \rho_w - \tilde{\rho}_{w0} = \frac{P}{C_w} \tag{2.33}$$

where C_c and C_w are cell and water compressibility coefficients, and $\tilde{\rho}_{c0}$, $\tilde{\rho}_{w0}$ are cell and water density constants at a given reference pressure. Compared to equivalent pressure-density relations in [14, 15], the compressibility coefficients C_w and C_c can be related to the speed of sound as

$$\begin{aligned}
C_c &= c_c^2, \\
C_w &= c_w^2,
\end{aligned} \tag{2.34}$$

where c_c and c_w are the speed of sound in the cell and water phase respectively, and to the isentropic compressibility factor β_s as

$$\beta_{s,l} = \frac{1}{\rho_l c_l^2}, \qquad l = c, w. \tag{2.35}$$

Similarly to the studies in [6], the expression chosen to represent $\Lambda(a)$, which takes into account how cells are sensitive to the chemical agent a, is given by

$$\Lambda = \Lambda(a) = \Lambda_0 + \Lambda_1 e^{-\lambda a}, \tag{2.36}$$

where Λ_0, Λ_1, and λ are positive parameters.

With regards to the source term S_a in (2.6), a standard expression for the Keller-Segel type of models (see [6, 23]) will be used, i.e.

$$S_a = s_0 n - s_1 a, \tag{2.37}$$

where s_0 and s_1 are known constants.

In addition to the closure relations above, useful and necessary observations with respect to the pressure function $P(n,m)$ are made in the following:

First, from (2.33) we find that

$$P = C_c(\rho_c - \tilde{\rho}_{c0}) = C_w(\rho_w - \tilde{\rho}_{w0}). \tag{2.38}$$

From (2.38) we get

$$\rho_w = \frac{C_c}{C_w}\rho_c - \frac{C_c}{C_w}\tilde{\rho}_{c0} + \tilde{\rho}_{w0} = \frac{C_c}{C_w}\rho_c + D, \qquad D = -\frac{C_c}{C_w}\tilde{\rho}_{c0} + \tilde{\rho}_{w0} > 0. \tag{2.39}$$

From (2.5) we then get the relation

$$m\rho_c + n\rho_w = \rho_w\rho_c, \tag{2.40}$$

and by substituting (2.39) into (2.40), we get

$$\frac{C_c}{C_w}\rho_c^2 - b\rho_c - c = 0, \tag{2.41}$$

where

$$\begin{cases} b \doteq b(m,n) = m + \frac{C_c}{C_w}n - D, \\ c \doteq c(n) = nD. \end{cases} \tag{2.42}$$

From (2.41), we obtain

$$\rho_c = \frac{C_w}{2C_c}\left[b \pm \sqrt{b^2 + \frac{4nDC_c}{C_w}}\right].$$

In order for ρ_c to become non-negative and unique, we recall that since $D > 0$, then $c = nD \geq 0$, and thus

$$\begin{cases} \rho_c = \rho_c(m,n) = \frac{C_w}{2C_c}\left[b + \sqrt{b^2 + \frac{4cC_c}{C_w}}\right], & \alpha_c = \frac{n}{\rho_c} \\ \rho_w = \rho_w(m,n) = \frac{C_c}{C_w}\rho_c + D, & \alpha_w = \frac{m}{\rho_w}. \end{cases} \tag{2.43}$$

2.6 Relation to Keller-Segel type of models

In order to relate the model given in (2.27) to the classical Keller-Segel type of models, this model must first be reduced from 3D to 1D, as done in (2.31).
We then impose the simplifying assumptions that:

- the water and cell phases are incompressible, i.e. ρ_c and ρ_w are taken to be constants, and
- that there are no viscous effects, i.e. $\varepsilon_c = \varepsilon_w = 0$.

The following simplified version of (2.31) is then obtained:

$$\begin{aligned} \frac{\partial \alpha_c}{\partial t} + \frac{\partial}{\partial x}(\alpha_c u_c) &= 0 \\ \frac{\partial \alpha_w}{\partial t} + \frac{\partial}{\partial x}(\alpha_w u_w) &= 0 \\ \frac{\partial}{\partial x}[\alpha_c \Lambda(a)] + \alpha_c \frac{\partial P}{\partial x} &= \hat{k}(u_w - u_c) \\ \alpha_w \frac{\partial P}{\partial x} &= -\hat{k}(u_w - u_c) \\ \frac{\partial a}{\partial t} &= D_a \frac{\partial^2 a}{\partial x^2} + S_a(a, \alpha_c). \end{aligned} \tag{2.44}$$

By adding the two momentum equations, $(2.44)_3$ and $(2.44)_4$, we get

$$\frac{\partial P}{\partial x} = -\frac{\partial}{\partial x}[\alpha_c \Lambda(a)], \tag{2.45}$$

and hence,

$$P = -\alpha_c \Lambda(a) + \tilde{P}(t),$$

where $\tilde{P}(t)$ is some function independent of x. Since only the pressure-gradient has an impact on the system, there is no need to specify $\tilde{P}(t)$.
Adding $(2.44)_1$ and $(2.44)_2$, integrating with respect to x, and applying boundary conditions

specified in (2.28) we get

$$u_w = -\frac{\alpha_c}{\alpha_w} u_c. \tag{2.46}$$

By combining (2.45) and (2.46) with $(2.44)_4$ we then get

$$-\alpha_w \frac{\partial}{\partial x}[\alpha_c \Lambda(a)] = \hat{k}\left(\frac{\alpha_c}{\alpha_w} + 1\right) u_c$$

which again leads to

$$\begin{aligned} u_c &= -\frac{\alpha_w^2}{\hat{k}} \frac{\partial}{\partial x}[\alpha_c \Lambda(a)] \\ u_w &= \frac{\alpha_c \alpha_w}{\hat{k}} \frac{\partial}{\partial x}[\alpha_c \Lambda(a)] \end{aligned} \tag{2.47}$$

where

$$\hat{k} = k \frac{\alpha_c \alpha_w \rho_c \rho_w}{\alpha_c \rho_c + \alpha_w \rho_w}. \tag{2.48}$$

Hence,

$$\begin{aligned} u_c &= -\left(\frac{\alpha_c}{\rho_w} + \frac{\alpha_w}{\rho_c}\right) \frac{\alpha_w}{k \alpha_c} \frac{\partial}{\partial x}[\alpha_c \Lambda(a)] \\ u_w &= \left(\frac{\alpha_c}{\rho_w} + \frac{\alpha_w}{\rho_c}\right) \frac{1}{k} \frac{\partial}{\partial x}[\alpha_c \Lambda(a)] \end{aligned} \tag{2.49}$$

Using the expression for u_c found in (2.49), in combination with the first equation of (2.44), we get

$$\frac{\partial \alpha_c}{\partial t} - \frac{\partial}{\partial x}\left(\left[\frac{\alpha_c}{\rho_w} + \frac{\alpha_w}{\rho_c}\right] \frac{\alpha_w}{k} \frac{\partial}{\partial x}[\alpha_c \Lambda(a)]\right) = 0 \tag{2.50}$$

where $\alpha_w = 1 - \alpha_c$. The model is in other words of the form

$$\begin{aligned} &\frac{\partial \alpha_c}{\partial t} - \frac{\partial}{\partial x}\left(g(\alpha_c) \frac{\partial}{\partial x}[\alpha_c \Lambda(a)]\right) = 0, \qquad g(\alpha_c) = \left[\frac{\alpha_c}{\rho_w} + \frac{1-\alpha_c}{\rho_c}\right] \frac{1-\alpha_c}{k}, \\ &\frac{\partial a}{\partial t} = D_a \frac{\partial^2 a}{\partial x^2} + s_0 n - s_1 a, \end{aligned} \tag{2.51}$$

which also can be written as

$$\begin{aligned}\frac{\partial \alpha_c}{\partial t} &= \frac{\partial}{\partial x}\left(g(\alpha_c)\Lambda(a)\frac{\partial \alpha_c}{\partial x} - \lambda\Lambda_1 g(\alpha_c)e^{-\lambda a}\alpha_c\frac{\partial a}{\partial x}\right),\\ \frac{\partial a}{\partial t} &= D_a\frac{\partial^2 a}{\partial x^2} + s_0 n - s_1 a.\end{aligned} \tag{2.52}$$

As we can see, this model is clearly within the class of general Keller-Segel type of models of the form

$$\begin{aligned}\frac{\partial u}{\partial t} &= \frac{\partial}{\partial x}\left(k_1(u,v)\frac{\partial u}{\partial x} - k_2(u,v)u\frac{\partial v}{\partial x}\right) + k_3(u,v),\\ \frac{\partial v}{\partial t} &= D_v\frac{\partial^2 v}{\partial x^2} + k_4(u,v) - k_5(u,v)v,\end{aligned} \tag{2.53}$$

where it also is clear that u plays the role of α_c and v plays the role of a.

Chapter 3

Numerical Solutions

In this chapter, the steps and procedures for numerically solving the models derived in Chapter 2 are outlined. The different methods used to solve these models are then compared to each other, using an appropriate chosen base case.

3.1 Solution methods and steps in the numerical solution

3.1.1 Discretization of space and time

Before starting to solve the discretized equations of the models presented in Chapter 2, we must divide the domains in both space and time into smaller units as illustrated in Fig. 3.1. The spatial domain, $[0,0] \times [L_x, L_y]$, is divided into smaller units know as *grid blocks* (see Fig. 3.1a), while the domain in time, $[0,T]$, is divided into a finite number of intervals known as *time steps* (see Fig. 3.1b). In this thesis, all the grid blocks are of the same size, and the length of each time step is constant. In other words, Δx, Δy and Δt are constants.

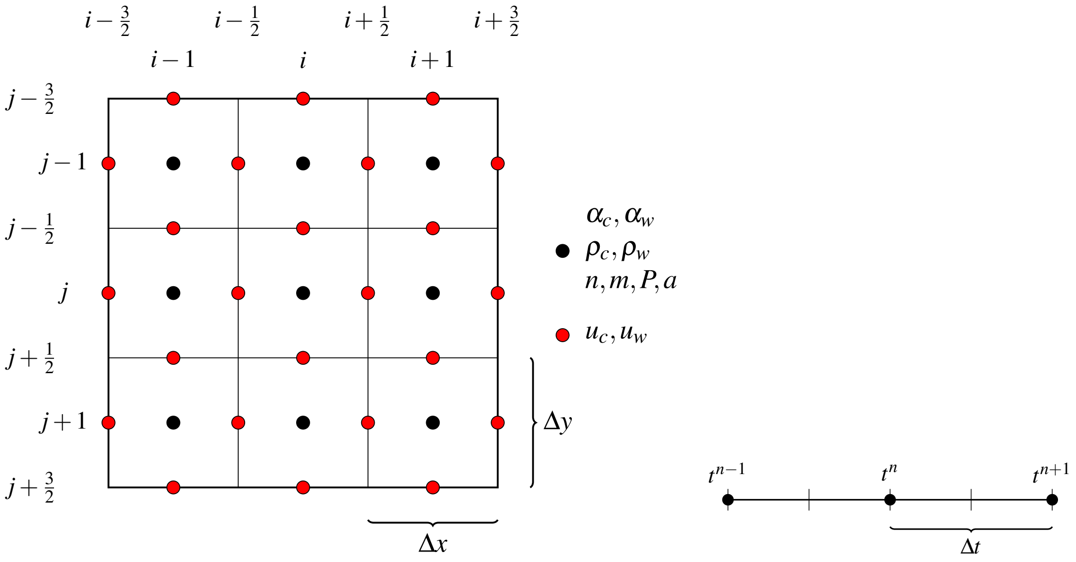

(a) Grid in space. **(b)** Grid in time.

Fig. 3.1. Illustration of the domain in both space (a) and time (b) divided into smaller grid blocks.

As illustrated in Fig. 3.1a, it has been chosen to use a staggered type of grid, where the phase velocities (u_c and u_w) are computed at the edges (red dots), while all the other variables are computed at the center of each grid block (black dots).

3.1.2 Steps in the numerical procedure

In order to best describe the steps in a numerical solution procedure, we define a 5×5 grid in space, denoting N_x as the number of blocks in the x-direction and N_y as the number of blocks in the y-direction, as illustrated in Fig. 3.2. The grid blocks has been numbered using ordinary ordering along lines, which by ordering along the x-direction gives rise to the relation

$$t = i + (j-1)N_x, \qquad \text{for } i = 1, \dots, N_x,\ j = 1, \dots, N_y,$$

where t represents the grid block number (see Fig. 3.2a). Regarding phase velocities, they are located at grid block interfaces as shown in Fig. 3.1a, and thus need their own separate numbering illustrated in Fig. 3.2b. The numbering in this figure has been obtained by assigning the number $t_{i,j}$ to velocities located at position (i, j) according to the following

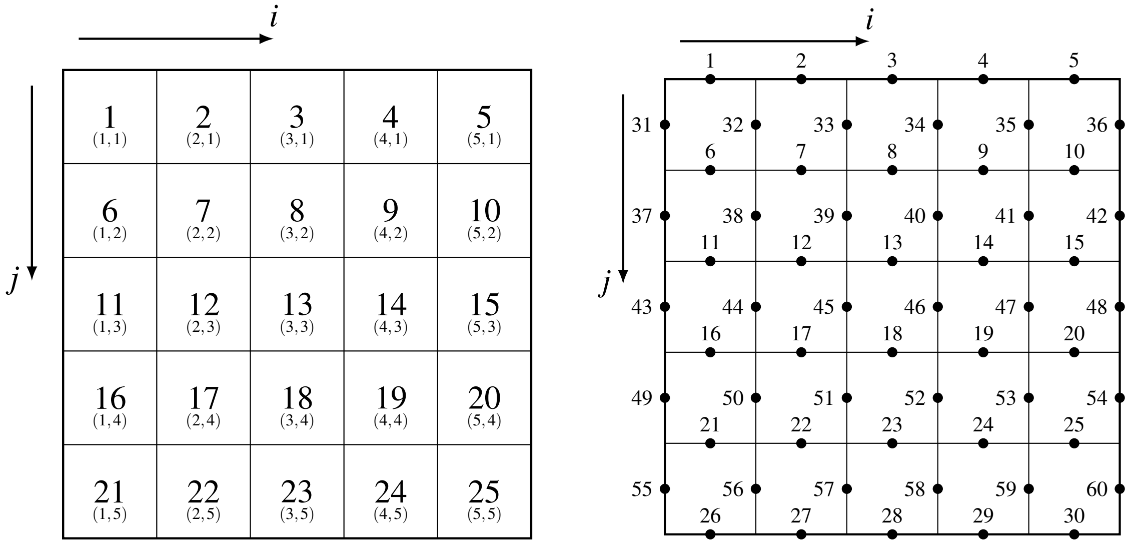

(a) Numbering of grid blocks with corresponding (i,j) coordinates.

(b) Numbering of phase velocities.

Fig. 3.2. Figures illustrating the numbering of **(a)** grid blocks, and **(b)** phase velocities.

relations:

$$\begin{aligned}
t_{i,j-1/2} &= i+(j-1)N_x, \\
t_{i,j+1/2} &= i+jN_x, \\
t_{i-1/2,j} &= N_x(N_y+j)+i+j-1, \\
t_{i+1/2,j} &= N_x(N_y+j)+i+j, \qquad i=1,\dots,N_x, \quad j=1,\dots,N_y.
\end{aligned}$$

Having defined a grid in both space and time, along with the corresponding numbering routine, the next step in the solution procedure is to replace the differential equations in (2.30) with algebraic difference equations. The details of this procedure is further addressed in the following subsections.

Momentum equations

The first step is to calculate the phase velocities using the momentum equations. As the velocities have a fixed value equal to zero at the boundaries according to (2.28), it is sufficient to solve equations for velocities positioned at the interior part of the domain.

Before writing out the discretized equations, we note that in order to ensure a lower bound for n and m, and in addition increase the stability properties of the model, we will introduce *regularization parameters* in the viscous terms of these equations, namely $\varepsilon_{c,reg}$ and $\varepsilon_{w,reg}$.

These constants will be implemented in the model simply by rewriting the expressions for the masses as: $n \to n + \varepsilon_{c,reg}$ and $m \to m + \varepsilon_{w,reg}$. For instance, the second term on the right hand side of $(2.30)_3$ will then be written as

$$2\varepsilon_c \frac{\partial}{\partial x}\left(n\frac{\partial u_c^x}{\partial x}\right) \to 2\varepsilon_c \frac{\partial}{\partial x}\left([n + \varepsilon_{c,reg}]\frac{\partial u_c^x}{\partial x}\right),$$

and similarly for the other terms containing n or m.

Introducing standard notations

$$\begin{aligned}\Delta_x f_{i,j} &= \frac{1}{\Delta x}\left(f_{i+1/2,j} - f_{i-1/2,j}\right)\\ \Delta_y f_{i,j} &= \frac{1}{\Delta y}\left(f_{i,j+1/2} - f_{i,j-1/2}\right)\end{aligned}$$

and correspondingly

$$\begin{aligned}\Delta_x f_{i+1/2,j} &= \frac{1}{\Delta x}\left(f_{i+1,j} - f_{i,j}\right)\\ \Delta_y f_{i+1/2,j} &= \frac{1}{\Delta y}\left(f_{i+1/2,j+1/2} - f_{i+1/2,j-1/2}\right)\end{aligned}$$

where $f_{i,j}$ is any function evaluated at position (i,j), the discretized versions of equations $(2.30)_3$ and $(2.30)_5$ at point $(i+1/2,j)$ can be written

$$\begin{aligned}\Delta_x\left[\alpha_c\Lambda\right]_{i+1/2,j} + \alpha_{c,i+1/2,j}\Delta_x P_{i+1/2,j} = {}& \hat{k}_{i+1/2,j}\left(u^x_{w,i+1/2,j} - u^x_{c,i+1/2,j}\right)\\ &+ 2\varepsilon_c\Delta_x\left(\left[n_{i+1/2,j} + \varepsilon_{c,reg}\right]\Delta_x u^x_{c,i+1/2,j}\right)\\ &+ \varepsilon_c\Delta_y\left(\left[n_{i+1/2,j} + \varepsilon_{c,reg}\right]\Delta_y u^x_{c,i+1/2,j}\right)\\ &+ \varepsilon_c\Delta_y\left(\left[n_{i+1/2,j} + \varepsilon_{c,reg}\right]\Delta_x u^y_{c,i+1/2,j}\right) \qquad (3.1)\end{aligned}$$

$$\begin{aligned}\alpha_{w,i+1/2,j}\Delta_x P_{i+1/2,j} = {}& -\hat{k}_{i+1/2,j}\left(u^x_{w,i+1/2,j} - u^x_{c,i+1/2,j}\right)\\ &+ 2\varepsilon_w\Delta_x\left(\left[m_{i+1/2,j} + \varepsilon_{w,reg}\right]\Delta_x u^x_{w,i+1/2,j}\right)\\ &+ \varepsilon_w\Delta_y\left(\left[m_{i+1/2,j} + \varepsilon_{w,reg}\right]\Delta_y u^x_{w,i+1/2,j}\right)\\ &+ \varepsilon_w\Delta_y\left(\left[m_{i+1/2,j} + \varepsilon_{w,reg}\right]\Delta_x u^y_{w,i+1/2,j}\right) \qquad (3.2)\end{aligned}$$

Similarly, the discretized versions of equations $(2.30)_4$ and $(2.30)_6$ at point $(i,j+1/2)$ takes the form

$$\begin{aligned}\Delta_y\left[\alpha_c\Lambda\right]_{i,j+1/2}+\alpha_{c,i,j+1/2}\Delta_y P_{i,j+1/2}=\;&\hat{k}_{i,j+1/2}\left(u^y_{w,i,j+1/2}-u^y_{c,i,j+1/2}\right)\\&+2\varepsilon_c\Delta_y\left(\left[n_{i,j+1/2}+\varepsilon_{c,reg}\right]\Delta_y u^y_{c,i,j+1/2}\right)\\&+\varepsilon_c\Delta_x\left(\left[n_{i,j+1/2}+\varepsilon_{c,reg}\right]\Delta_x u^y_{c,i,j+1/2}\right)\\&+\varepsilon_c\Delta_x\left(\left[n_{i,j+1/2}+\varepsilon_{c,reg}\right]\Delta_y u^x_{c,i,j+1/2}\right)\end{aligned}\tag{3.3}$$

$$\begin{aligned}\alpha_{w,i,j+1/2}\Delta_y P_{i,j+1/2}=\;&-\hat{k}_{i,j+1/2}\left(u^y_{w,i,j+1/2}-u^y_{c,i,j+1/2}\right)\\&+2\varepsilon_w\Delta_y\left(\left[m_{i,j+1/2}+\varepsilon_{w,reg}\right]\Delta_y u^y_{w,i,j+1/2}\right)\\&+\varepsilon_w\Delta_x\left(\left[m_{i,j+1/2}+\varepsilon_{w,reg}\right]\Delta_x u^y_{w,i,j+1/2}\right)\\&+\varepsilon_w\Delta_x\left(\left[m_{i,j+1/2}+\varepsilon_{w,reg}\right]\Delta_y u^x_{w,i,j+1/2}\right)\end{aligned}\tag{3.4}$$

As the terms $\alpha_{c,i+1/2,j}$, $\alpha_{c,i,j+1/2}$, $\hat{k}_{i+1/2,j}$, and $\hat{k}_{i,j+1/2}$ are not defined using the grid defined in Fig. 3.2, they are approximated as the average value of neighboring blocks, i.e.

$$\begin{aligned}\alpha_{c,i+1/2,j}&=\frac{\alpha_{c,i+1,j}+\alpha_{c,i,j}}{2}, &\qquad \alpha_{c,i,j+1/2}&=\frac{\alpha_{c,i,j+1}+\alpha_{c,i,j}}{2},\\ \hat{k}_{i+1/2,j}&=\frac{\hat{k}_{i+1,j}+\hat{k}_{i,j}}{2}, &\qquad \hat{k}_{i,j+1/2}&=\frac{\hat{k}_{i,j+1}+\hat{k}_{i,j}}{2}.\end{aligned}\tag{3.5}$$

Other terms that needs specification are $n_{i+1/2,j+1/2}$, $n_{i+1/2,j-1/2}$, and $n_{i-1/2,j+1/2}$ arising from $\Delta_y n_{i+1/2,j}$ and $\Delta_x n_{i,j+1/2}$ on the right hand side of (3.1) and (3.3), in addition to similar terms for the water mass m in (3.2) and (3.4). Consistent with the approach used in (3.5), these terms have been approximated by averaging of intersecting blocks

$$\begin{aligned}n_{i+1/2,j+1/2}&=\frac{n_{i,j}+n_{i+1,j}+n_{i,j+1}+n_{i+1,j+1}}{4},\\ n_{i+1/2,j-1/2}&=\frac{n_{i,j-1}+n_{i+1,j-1}+n_{i,j}+n_{i+1,j}}{4},\\ n_{i-1/2,j+1/2}&=\frac{n_{i-1,j}+n_{i,j}+n_{i-1,j+1}+n_{i,j+1}}{4}.\end{aligned}$$

With regards to boundary conditions, it is clear that any terms multiplied with $u_{l,1/2,j}$, $u_{l,N_x+1/2,j}$, $u_{l,i,1/2}$, or $u_{l,i,N_y+1/2}$ (where $l=c,w$) becomes zero, and drop out of the equations naturally. However, the terms $u_{l,i+1/2,0}$ and $u_{l,0,j+1/2}$ for $l=c,w$ appear when solving equations for blocks $i=1,\dots,N_x-1$, $j=1$, and $i=1$, $j=1,\dots,N_y-1$, respectively. By choosing to define these terms as

$$u_{l,i+1/2,0} = u_{l,i+1/2,1}, \quad u_{l,0,j+1/2} = u_{l,1,j+1/2}, \quad l = c, w,$$

we simply make sure that for the blocks in mention, the second to last term on the right hand side of (3.1) to (3.4) will become zero.

By evaluating equations (3.1) and (3.2) for $i = 1, \ldots, Nx-1$, $j = 1, \ldots, Ny$, and equations (3.3) and (3.4) for $i = 1, \ldots, Nx$, $j = 1, \ldots, Ny-1$ we get a system of linear equations of the form $A\vec{x} = \vec{b}$, where the number of equations to be solved equals $2N_x(Ny-1) + 2N_y(N_x-1)$.

By first ordering the equations (3.3) and (3.4) every other for the cell and water phase, evaluated at values of i and j as described above, and then continue in the same manner for equations (3.1) and (3.2), the coefficient matrix A becomes diagonal and symmetric as illustrated in Fig. 3.3, where the sparsity pattern of A has been plotted for the 5×5 grid defined in Fig. 3.2.

Correspondingly, $\vec{x}$ and $\vec{b}$ takes the form

$$\vec{x} = \begin{pmatrix} u_{c,1,3/2} \\ u_{w,1,3/2} \\ \vdots \\ u_{c,N_x,N_y-1/2} \\ u_{w,N_x,N_y-1/2} \\ u_{c,3/2,1} \\ u_{w,3/2,1} \\ \vdots \\ u_{c,N_x-1/2,N_y} \\ u_{w,Nx-1/2,N_y} \end{pmatrix}, \qquad \vec{b} = \begin{pmatrix} \Delta_y \left[\alpha_c \Lambda\right]_{1,3/2} + \alpha_{c,1,3/2} \Delta_y P_{1,3/2} \\ \alpha_{w,1,3/2} \Delta_y P_{1,3/2} \\ \vdots \\ \Delta_y \left[\alpha_c \Lambda\right]_{N_x,N_y-1/2} + \alpha_{c,N_x,N_y-1/2} \Delta_y P_{N_x,N_y-1/2} \\ \alpha_{w,N_x,N_y-1/2} \Delta_y P_{N_x,N_y-1/2} \\ \Delta_x \left[\alpha_c \Lambda\right]_{3/2,1} + \alpha_{c,3/2,1} \Delta_x P_{3/2,1} \\ \alpha_{w,3/2,1} \Delta_x P_{3/2,1} \\ \vdots \\ \Delta_x \left[\alpha_c \Lambda\right]_{N_x-1/2,N_y} + \alpha_{c,N_x-1/2,N_y} \Delta_x P_{N_x-1/2,N_y} \\ \alpha_{w,N_x-1/2,N_y} \Delta_x P_{N_x-1/2,N_y} \end{pmatrix}.$$

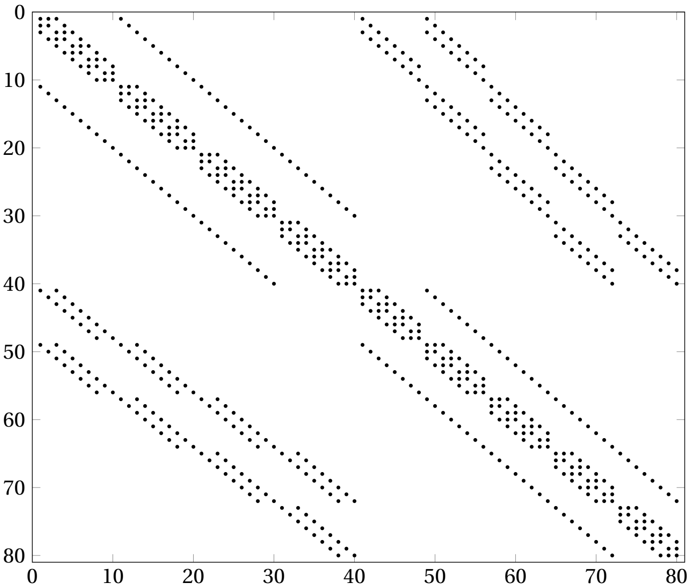

Fig. 3.3. Sparsity pattern of the coefficient matrix A for the momentum equations.

Mass balance equations

The next step is then to explicitly calculate the masses n and m at a new time step, t^{n+1}, using $(2.30)_1$ and $(2.30)_2$. Using explicit discretization in time, the discretized mass balance equations takes the form

$$\frac{f_{i,j}^{n+1}-f_{i,j}^{n}}{\Delta t}+\left(\frac{F_{i+1/2,j}^{n}-F_{i-1/2,j}^{n}}{\Delta x}\right)+\left(\frac{F_{i,j+1/2}^{n}-F_{i,j-1/2}^{n}}{\Delta y}\right)=0, \qquad f=m,n$$

where we by defining

$$\begin{aligned}
F_{i+1/2,j}^{n} &= u_{l,i+1/2,j}^{n}\left(\frac{f_{i+1,j}^{n}+f_{i,j}^{n}}{2}\right)-|u_{l,i+1/2,j}^{n}|\left(\frac{f_{i+1,j}^{n}-f_{i,j}^{n}}{2}\right),\\
F_{i-1/2,j}^{n} &= u_{l,i-1/2,j}^{n}\left(\frac{f_{i,j}^{n}+f_{i-1,j}^{n}}{2}\right)-|u_{l,i-1/2,j}^{n}|\left(\frac{f_{i,j}^{n}-f_{i-1,j}^{n}}{2}\right),\\
F_{i,j+1/2}^{n} &= u_{l,i,j+1/2}^{n}\left(\frac{f_{i,j+1}^{n}+f_{i,j}^{n}}{2}\right)-|u_{l,i,j+1/2}^{n}|\left(\frac{f_{i,j+1}^{n}-f_{i,j}^{n}}{2}\right),\\
F_{i,j-1/2}^{n} &= u_{l,i,j-1/2}^{n}\left(\frac{f_{i,j}^{n}+f_{i,j-1}^{n}}{2}\right)-|u_{l,i,j-1/2}^{n}|\left(\frac{f_{i,j}^{n}-f_{i,j-1}^{n}}{2}\right), \qquad f=m,n, \quad l=c,w
\end{aligned} \tag{3.6}$$

ensure an upwind evaluation of the flux terms, relative to u_c and u_w.

With regards to boundary conditions, this scheme holds for any $i = 1,\dots,N_x$, $j = 1,\dots,N_y$, as terms multiplied by $u_{l,1/2,j}$, $u_{l,N_x+1/2,j}$, $u_{l,i,1/2}$ or $u_{l,i,N_y+1/2}$ for $l = c,w$ becomes zero according to (2.28).

Diffusion equation for the chemical agent

After the masses has been calculated, the last step in the solution procedure is to calculate the chemical agent a at time level t^{n+1}.

Using implicit discretization in time, we get

$$\frac{a_{i,j}^{n+1} - a_{i,j}^{n}}{\Delta t} = D_a \left(\frac{a_{i+1,j}^{n+1} - 2a_{i,j}^{n+1} + a_{i-1,j}^{n+1}}{\Delta x^2} + \frac{a_{i,j+1}^{n+1} - 2a_{i,j}^{n+1} + a_{i,j-1}^{n+1}}{\Delta y^2} \right) + s_0 n_{i,j}^{n+1} - s_1 a_{i,j}^{n}.$$

which by reordering of variables results in

$$\begin{aligned}\left(s_0 n_{i,j}^{n+1} - s_1 a_{i,j}^{n}\right) \Delta t + a_{i,j}^{n} = -\gamma_y D_a a_{i,j-1}^{n+1} - \gamma_x D_a a_{i-1,j}^{n+1} + (1 + 2\gamma_x D_a + 2\gamma_y D_a)\, a_{i,j}^{n+1} \\ - \gamma_x D_a a_{i+1,j}^{n+1} - \gamma_y D_a a_{i,j+1}^{n+1}, \qquad \text{where } \gamma_x = \frac{\Delta t}{\Delta x^2},\ \gamma_y = \frac{\Delta t}{\Delta y^2}.\end{aligned} \tag{3.7}$$

We then proceed by evaluating this equation *only* for grid blocks located at the interior part of the domain (i.e. blocks not in contact with any boundaries), which for the 5×5 grid in Fig. 3.2a corresponds to blocks $7-9$, $12-14$, and $17-19$. The system consisting of $(N_x - 2)(Ny - 2)$ linear equations can then be written as $A\vec{x} = \vec{b}$, where the coefficient matrix A is pentadiagonal and symmetric. The sparsity pattern of A has been plotted in Fig. 3.4. Also, note that we evaluate the term $-\Delta t s_1 a_{i,j}^{n}$ which appear on the left hand side of (3.7) at time levevel t^n instead of t^{n+1}, a choice that causes all non-zero elements in A to be constant along the diagonals, simplifying the computations to some extent, without having a noticeable effect on the computed solution.

The resulting elements on the bands of A are: $1 + 2\gamma_x D_a + 2\gamma_y D_a$ for the main diagonal, $-\gamma_x D_a$ for the diagonals directly above and below the main diagonal, and $-\gamma_y D_a$ for the two diagonals furthest away from the main diagonal.

When evaluating (3.7) for the grid blocks mentioned above, we get terms on the right hand side corresponding to variables located outside of the domain for which we compute solutions. For the 5×5 this will be the case for all of the interior grid blocks, except block number 13. By choosing to evaluate these terms at time level t^n instead of t^{n+1}, we can move

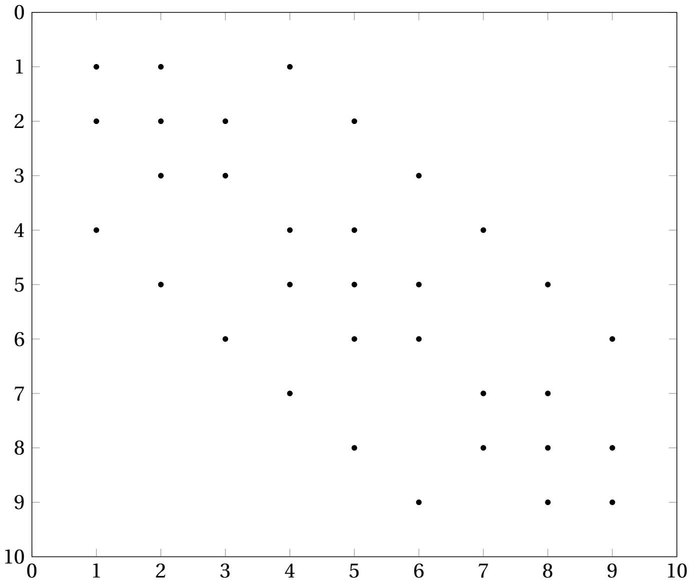

Fig. 3.4. Sparsity pattern of the coefficient matrix A for the diffusion equation.

them to the left hand side of the equation, and hence $\vec{x}$ and $\vec{b}$ can be written as

$$\vec{x} = \begin{pmatrix} a_7^{n+1} \\ \vdots \\ a_9^{n+1} \\ a_{12}^{n+1} \\ \vdots \\ a_{14}^{n+1} \\ a_{17}^{n+1} \\ \vdots \\ a_{19}^{n+1} \end{pmatrix}, \qquad \vec{b} = \begin{pmatrix} \left(s_0 n_7^{n+1} - s_1 a_7^n\right)\Delta t + a_7^n + \gamma_x D_a a_6^n + \gamma_y D_a a_2^n \\ \left(s_0 n_8^{n+1} - s_1 a_8^n\right)\Delta t + a_8^n + \gamma_y D_a a_3^n \\ \left(s_0 n_9^{n+1} - s_1 a_9^n\right)\Delta t + a_9^n + \gamma_x D_a a_{10}^n + \gamma_y D_a a_4^n \\ \left(s_0 n_{12}^{n+1} - s_1 a_{12}^n\right)\Delta t + a_{12}^n + \gamma_x D_a a_{11}^n \\ \left(s_0 n_{13}^{n+1} - s_1 a_{13}^n\right)\Delta t + a_{13}^n \\ \left(s_0 n_{14}^{n+1} - s_1 a_{14}^n\right)\Delta t + a_{14}^n + \gamma_x D_a a_{15}^n \\ \left(s_0 n_{17}^{n+1} - s_1 a_{17}^n\right)\Delta t + a_{17}^n + \gamma_x D_a a_{16}^n + \gamma_y D_a a_{22}^n \\ \left(s_0 n_{18}^{n+1} - s_1 a_{18}^n\right)\Delta t + a_{18}^n + \gamma_y D_a a_{23}^n \\ \left(s_0 n_{19}^{n+1} - s_1 a_{19}^n\right)\Delta t + a_{19}^n + \gamma_x D_a a_{20}^n + \gamma_y D_a a_{24}^n \end{pmatrix},$$

where the indices (i, j) has been replaced with t.

Applying *Neumann* (or *second-type*) boundary conditions according to (2.28), the blocks outside of the interior take the values

$$\begin{aligned} a_{1,j}^{n+1} &= a_{2,j}^{n+1} \\ a_{N_x,j}^{n+1} &= a_{N_x-1,j}^{n+1} \\ a_{i,1}^{n+1} &= a_{i,2}^{n+1} \\ a_{i,N_y}^{n+1} &= a_{i,N_y-1}^{n+1}, \qquad i = 1,\dots,N_x,\ j = 1,\dots,N_y. \end{aligned}$$

Numerical solution of the simplified K-S model

A solution of the simplified Keller-Segel type of model in (2.44) is obtained by first solving $(2.49)_1$ for the cell phase velocities, then compute α_c from $(2.44)_1$, and finally solve $(2.44)_5$ for the chemical agent.

By taking use of the function $g(\alpha_c)$ in (2.51), we can rewrite $(2.49)_1$ as

$$u_c = -\frac{g(\alpha_c)}{\alpha_c}\frac{\partial}{\partial x}\left[\alpha_c \Lambda(a)\right].$$

The discretized version of this equation at point $i+1/2$ then becomes

$$u_{c,i+1/2} = -\frac{g(\alpha_c)_{i+1/2}}{\alpha_{c,i+1/2}}\left(\frac{[\alpha_c\Lambda(a)]_{i+1} - [\alpha_c\Lambda(a)]_i}{\Delta x}\right).$$

Similarly as in (3.5), we choose to approximate $\alpha_{c,i+1/2}$ by

$$\alpha_{c,i+1/2} = \frac{\alpha_{c,i+1} + \alpha_{c,i}}{2},$$

and in addition

$$g(\alpha_c)_{i+1/2} \approx g(\alpha_{c,i+1/2}).$$

Using explicit discretization in time, the mass balance equation $(2.44)_1$ can be written as

$$\frac{\alpha_{c,i}^{n+1} - \alpha_{c,i}^{n}}{\Delta t} + \left(\frac{(\alpha_c u_c)_{i+1/2}^{n} - (\alpha_c u_c)_{i-1/2}^{n}}{\Delta x}\right) = 0,$$

where we similarly to (3.6) use an upwind evaluation of the flux terms, according to

$$\begin{aligned}
(\alpha_c u_c)_{i+1/2}^{n} &= u_{c,i+1/2}^{n}\left(\frac{\alpha_{c,i+1}^{n} + \alpha_{c,i}^{n}}{2}\right) - |u_{c,i+1/2}^{n}|\left(\frac{\alpha_{c,i+1}^{n} - \alpha_{c,i}^{n}}{2}\right),\\
(\alpha_c u_c)_{i-1/2}^{n} &= u_{c,i-1/2}^{n}\left(\frac{\alpha_{c,i}^{n} + \alpha_{c,i-1}^{n}}{2}\right) - |u_{c,i-1/2}^{n}|\left(\frac{\alpha_{c,i}^{n} - \alpha_{c,i-1}^{n}}{2}\right).
\end{aligned}$$

At last, the calculation of the chemical agent is done using the same approach as outlined in the previous subsection, except that the domain is now one-dimensional.

3.1.3 Solution methods

When solving the model in one dimension, the solution procedure follows the steps outlined in Subsections 3.1.1 and 3.1.2. For the model in two dimensions however, there are three different approaches/methods considered in this thesis.

Method I

The first solution method is a standard dimensional splitting approach [33, 47], where the single problem in two dimensions is divided into multiple one-dimensional problems.

First, we denote $U(x,y,t^n)$ as the solution of the model problem in (2.30) at time level t^n, and then assume that the approximation U^n is given by $U^n(x,y) \approx U(x,y,t^n)$.

Then, in order to construct an approximation U^{n+1} at new time level t^{n+1}, such that

$$U^{n+1} \approx U(x,y,t^{n+1}),$$

we introduce the one-dimensional operators T_x^t and T_y^t associated with the one-dimensional models:

$$T_x^t : \begin{cases} \partial_t n + \partial_x (n u_c^x) = 0, \\ \partial_t m + \partial_x (m u_w^x) = 0, \\ \partial_x [\alpha_c \Lambda(a)] + \alpha_c \partial_x P = \hat{k}(u_w^x - u_c^x) + 2\varepsilon_c \partial_x (n \partial_x u_c^x), \\ \alpha_w \partial_x P = -\hat{k}(u_w^x - u_c^x) + 2\varepsilon_w \partial_x (m \partial_x u_w^x), \\ \partial_t a = D_a \partial_x^2 a + \frac{1}{2} S_a(a,n), \end{cases}$$

and

$$T_y^t : \begin{cases} \partial_t n + \partial_y (n u_c^x) = 0, \\ \partial_t m + \partial_y (m u_w^x) = 0, \\ \partial_y [\alpha_c \Lambda(a)] + \alpha_c \partial_y P = \hat{k}(u_w^y - u_c^y) + 2\varepsilon_c \partial_y \left(n \partial_y u_c^y\right), \\ \alpha_w \partial_y P = -\hat{k}(u_w^y - u_c^y) + 2\varepsilon_w \partial_y \left(m \partial_y u_w^y\right), \\ \partial_t a = D_a \partial_y^2 a + \frac{1}{2} S_a(a,n). \end{cases}$$

Note here that we have multiplied the source term $S_a(a,n)$ with $1/2$, in order to account for the fact that it appears twice, both in T_x^t and in T_y^t. In other words, we simply think of this as a splitting of $S_a = 1/2 S_a + 1/2 S_a$.

The approximated solution U^{n+1} is then obtained by the following sequence of operators:

$$U^{n+1} = \left(T_y^{\Delta t} T_x^{\Delta t}\right) U^n,$$

which in other words express that we first compute $T_x^{\Delta t}$ using the solution U^n as initial data, and then proceed to compute $T_y^{\Delta t}$ using the calculated $T_x^{\Delta t}U^n$ as initial data.

This approach has been illustrated using a 4 × 4 grid in Fig. 3.5, where the arrows in Fig. 3.5a represents the one-dimensional problems solved by T_x^t, and the arrows in Fig. 3.5a represents the one-dimensional problems solved by T_y^t.

The benefit of adapting such an approach is that the computational time is reduced without necessarily affecting the solution to any significant extent, compared to a non-split method. Some of the draw backs, however, are that the cross partial derivatives in the momentum equations (i.e. shear stresses) are neglected, and that the source term $S_a(a,n)$ is approximated by $S_a = 1/2S_a + 1/2S_a$.

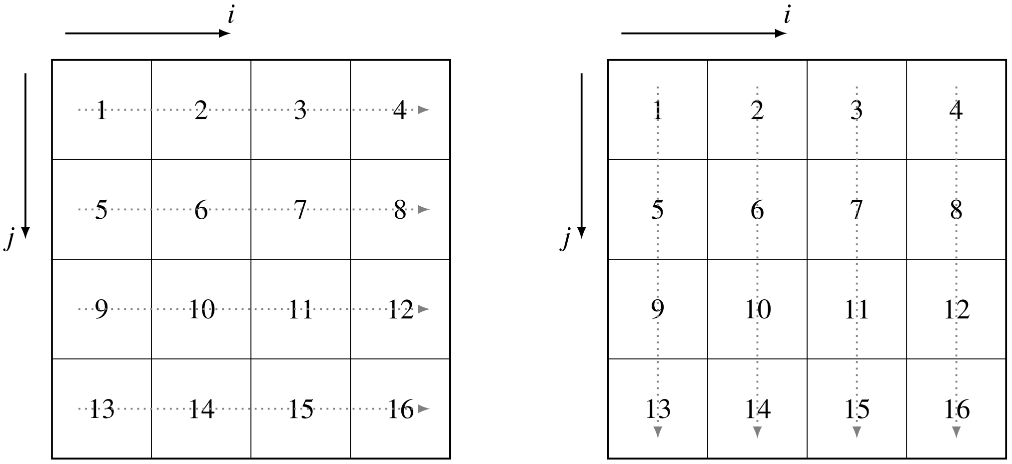

(a) Solving one-dimensional problems for blocks in the x-direction.

(b) Solving one-dimensional problems for blocks in the y-direction.

Fig. 3.5. Illustration of the solution procedure for the dimensional splitting method.

Method II

The second method is to solve for all variables in both spatial directions simultaneously, i.e. no splitting of dimensions. Using a similar analogy to that of Method I, we set $T_{2\mathrm{D}}^t$ equal to the model given in (2.30), and hence obtain a solution at time level t^{n+1} according to

$$U^{n+1} = T_{2\mathrm{D}}^{\Delta t}U^n.$$

This method requires the most amount of computational resources, and hence takes most time to compute. The main reason being that the system of linear equations arising from the momentum equations becomes quite large and more difficult to solve. This has been illustrated in Fig. 3.3 and Fig. 3.4, where the coefficient matrix A is much larger for the momentum equations (Fig. 3.3) than for the chemical agent (Fig. 3.4), even for a relatively small amount of grid blocks. Some of the benefits of using this method compared to Method I, are that the shear stress terms are included, and that the source term in $(2.30)_7$ is treated more correctly (i.e. no splitting of this term).

Method III

The third, and last method, is a mix of the two methods above. Here, we first solve the momentum equations using the dimensional splitting method described in Method I, but remain to solve equations for mass and chemical agent as described in Method II (i.e. no splitting).

Expressed by analogy similar to that used in Method I and II, we define

$$T_x : \begin{cases} \partial_x \left[\alpha_c \Lambda(a)\right] + \alpha_c \partial_x P = \hat{k}(u_w^x - u_c^x) + 2\varepsilon_c \partial_x \left(n \partial_x u_c^x\right), \\ \alpha_w \partial_x P = -\hat{k}(u_w^x - u_c^x) + 2\varepsilon_w \partial_x \left(m \partial_x u_w^x\right), \end{cases}$$

$$T_y : \begin{cases} \partial_y \left[\alpha_c \Lambda(a)\right] + \alpha_c \partial_y P = \hat{k}(u_w^y - u_c^y) + 2\varepsilon_c \partial_y \left(n \partial_y u_c^y\right), \\ \alpha_w \partial_y P = -\hat{k}(u_w^y - u_c^y) + 2\varepsilon_w \partial_y \left(m \partial_y u_w^y\right), \end{cases}$$

and

$$T_{2\text{D}}^t : \begin{cases} \partial_t n + \nabla \cdot (n \vec{u}_c) = 0, \\ \partial_t m + \nabla \cdot (m \vec{u}_w) = 0, \\ \partial_t a = D_a \nabla^2 a + S_a(a,n). \end{cases} \tag{3.8}$$

The solution at $t = t^{n+1}$ is then calculated according to

$$U^{n+1} = \left(T_{2\text{D}}^{\Delta t} T_y T_x\right) U^n.$$

The benefits of using this method is that the computational time is reduced compared to Method II (by a factor ~ 10, depending on, among other things, the number of grid blocks), while still being able to avoid splitting of the source term $S_a(a,n)$. On the other hand, this method does not include shear stress terms in the momentum equations, and hence, any information related to these terms will be lost.

In order to more carefully investigate the different properties of the methods described, a base case is established in the next section, also making it possible to compare these methods to the simulated results in one dimension.

3.2 Base Case

In this section a one-dimensional base case will be defined. A two-dimensional equivalent to this case is then defined in section 3.2.2, making it possible to compare the one and two-dimensional solutions to each other.

The domain considered in one dimension is $[0,L] \times [0,T]$, where $L = 100\,\mathrm{m}$ and $T = 10\,000\,\mathrm{s}$. With regards to the number of grid blocks and time steps, we have divided the domain $[0,L]$ into 100 grid cells, and $[0,T]$ into $1.25 \cdot 10^6$ time steps. The input parameters for this case are listed in Table 3.1.

Table 3.1. Input parameters for the base case:

Parameter	Description	Value	Unit
k	Interface friction constant in (2.14)	25	s^{-1}
Λ_0	Parameter in (2.36)	$5 \cdot 10^3$	Pa
Λ_1	Parameter in (2.36)	$1 \cdot 10^6$	Pa
λ	Parameter in (2.36)	25	$\mathrm{m}^3\,\mathrm{mol}^{-1}$
s_0	Parameter in (2.37)	0.1	$\mathrm{mol}\,\mathrm{kg}^{-1}\,\mathrm{s}^{-1}$
s_1	Parameter in (2.37)	0.2	s^{-1}
C_w	Compressibility factor (water) in (2.33)	10^6	$\mathrm{m}^2\,\mathrm{s}^{-2}$
C_c	Compressibility factor (cell) in (2.33)	10^5	$\mathrm{m}^2\,\mathrm{s}^{-2}$
$\tilde{\rho}_{w0}$	Water density constant in (2.33)	999.9	$\mathrm{kg}\,\mathrm{m}^{-3}$
$\tilde{\rho}_{c0}$	Cell density constant in (2.33)	800	$\mathrm{kg}\,\mathrm{m}^{-3}$
D_a	Diffusion coefficient	0.4	$\mathrm{m}^2\,\mathrm{s}^{-1}$
ε_c	Kinematic viscosity (cell)	$1 \cdot 10^4$	$\mathrm{m}^2\,\mathrm{s}^{-1}$
ε_w	Kinematic viscosity (water)	$1 \cdot 10^4$	$\mathrm{m}^2\,\mathrm{s}^{-1}$
$\varepsilon_{c,reg}$	Viscosity regularization parameter (cell)	500	$\mathrm{kg}\,\mathrm{m}^{-3}$
$\varepsilon_{w,reg}$	Viscosity regularization parameter (water)	500	$\mathrm{kg}\,\mathrm{m}^{-3}$

The initial data used is:

$$P_0 = 2 \cdot 10^5\ \mathrm{Pa}, \qquad \rho_{w0} = \frac{P_0}{C_w} + \tilde{\rho}_{w0}, \qquad \rho_{c0} = \frac{P_0}{C_c} + \tilde{\rho}_{c0}$$

and

$$\alpha_{c0}(x) = 0.2 + 0.01 \cos\left(\frac{2\pi x}{\omega L}\right), \qquad \omega = 0.1$$

From these we can compute the initial state $n_0(x)$ and $m_0(x)$. The initial concentration of the chemical agent $a_0(x)$ is given by

$$a_0(x) = \frac{1}{2L}\int_0^L \alpha_{c0}(x)\,dx,$$

whereas the initial velocities are set to

$$u_{c0}(x) = u_{w0}(x) = 0.$$

3.2.1 Simulated results in one dimension

Cartesian coordinate system

The result plotted in Fig. 3.6 is obtained by solving the model in (2.31) using the steps outlined above. Here, we clarely see that a pattern starts to form approximately after $t = 3000\,\mathrm{s}$, resulting in two distinct peaks at the end of the simulation.

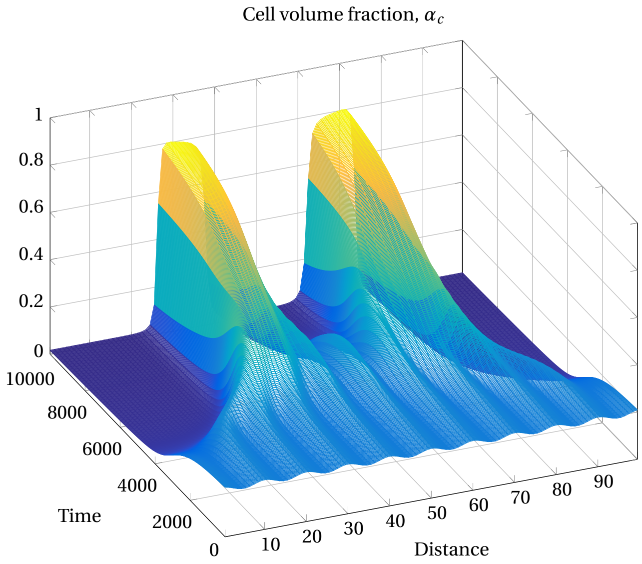

Fig. 3.6. A plot of the cell volume fraction (α_c) for the base case.

We then proceed to investigate the effects caused by viscous terms in the momentum equations and treating the cell and water phase as weakly compressible fluids, by comparing the results in Fig. 3.6 to the results of the simplified Keller-Segel type of model in (2.44) on page 17. Following the solution procedure outlined on page 30, we obtain the results presented in Fig. 3.7 for this model. Here, we see that a pattern with several peaks is formed almost instantaneously, before grouping together into two peaks, similarly to the solution in

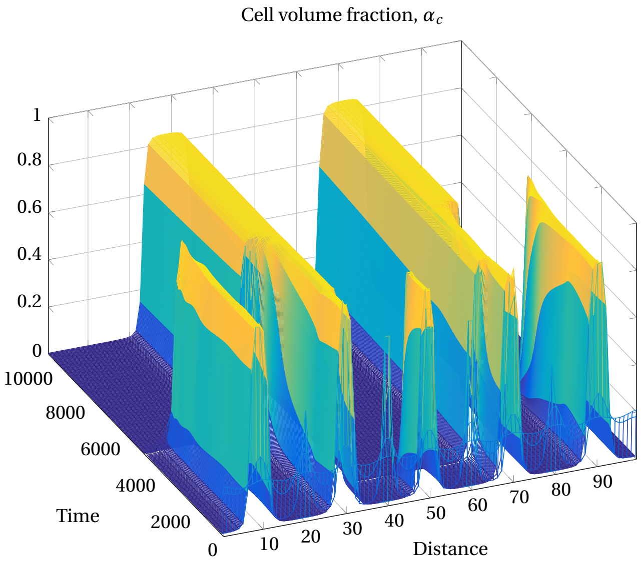

Fig. 3.7. A plot of the base case for the simplified Keller-Segel version of (2.31), found in (2.44).

Fig. 3.6.
This coincides well with the expectation that a non-viscous fluid would deform at a higher rate than a viscous fluid, as viscosity itself is a measure of the internal friction opposing deformation of the fluid [2].

In order to get some information about the role played by the regularization parameters that were introduced in Section 3.1.2, we ran a new simulation of the base case where $\varepsilon_{c,reg}$ and $\varepsilon_{w,reg}$ were set equal to zero. In addition, the time step length had to be reduced by a factor 10 in order to avoid numerical instabilities. The result obtained is shown in Fig. 3.8.

In this figure we clearly see the same type of behavior as seen in Fig. 3.6, where the initial ripples eventually group together and form a pattern with two peaks. However, the reduced viscosity effect results in a steady-state-like behavior being reached at a much earlier stage in the simulation, and the two peaks are also located further apart from each other than what is observed in Fig. 3.6. On the other hand, the quick response is more similar to that of the simplified Keller-Segel type of model in Fig. 3.7 which has no viscous effects, strengthening the claim that the majority of the differences observed in Figures 3.6 and 3.7 are indeed caused by the viscous terms in the momentum equations.

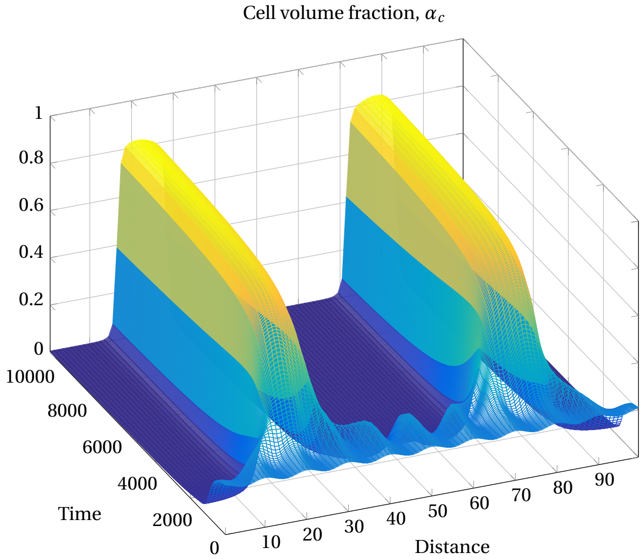

Fig. 3.8. A plot of α_c for the base case where $\varepsilon_{c,reg} = \varepsilon_{w,reg} = 0$, and where the number of time steps is $1.25 \cdot 10^7$.

Polar coordinate system

For a case in the polar coordinate system, the solutions are computed using the reduced cylindrical model given in (2.32), only expressing solutions that depend on r. The spatial domain for this case is $[\delta, R]$, where δ is a lower limit greater than zero, in these simulations set equal to 0.5 m, while $R = 100\,\text{m}$. This domain has then been divided into 100 grid blocks, consistent with the base case in Cartesian coordinates.

The input parameters used are listed in Table 3.1, while the initial cell volume fraction is given by

$$\alpha_{c0}(r) = 0.2 + 0.01 \cos\left(\frac{2\pi(r-\delta)}{\omega(R-\delta)}\right), \tag{3.9}$$

and the concentration of the chemical agent is given by

$$a_0(r) = \frac{1}{2(R-\delta)} \int_{\delta}^{R} \alpha_{c0}(r)\, dr. \tag{3.10}$$

The solutions obtained has then been plotted for values of θ ranging from 0 to 2π, which results in the symmetrical 2D plots presented in Fig. 3.9. As we can see, already in Fig. 3.9a cells has started to migrate from the center and outwards. This behavior continues in Fig. 3.9b and 3.9c eventually leading to the forming of a single peak, stretching around the outer

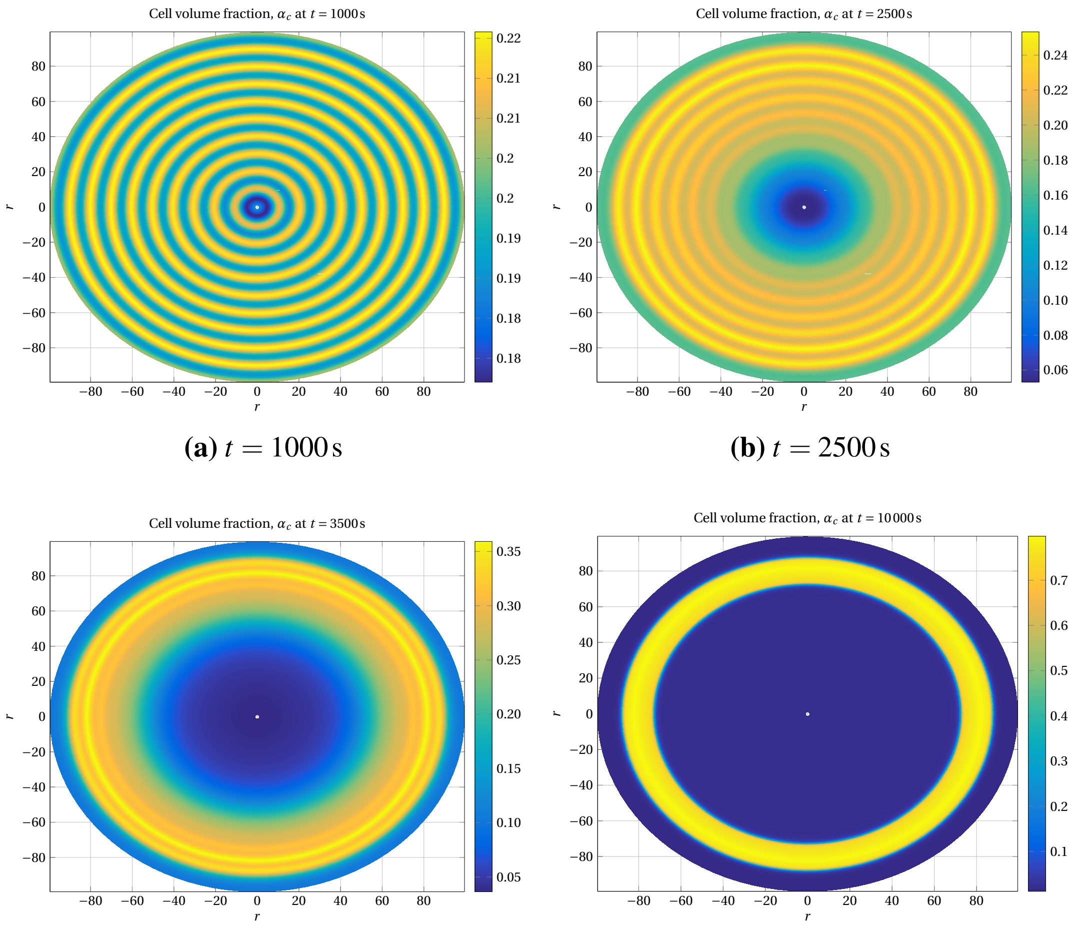

(a) $t = 1000\,\mathrm{s}$ **(b)** $t = 2500\,\mathrm{s}$

(c) $t = 3500\,\mathrm{s}$ **(d)** $t = 10\,000\,\mathrm{s}$

Fig. 3.9. Figures showing the evolution of α_c using the model in polar coordinates.

part of the domain, as seen in Fig. 3.9d. Although the case in polar coordinates not directly compares to the Cartesian base case, we clearly see that the smaller ripples in the initial data will group together and form a pattern.

3.2.2 Base case in two dimensions

As stated above, the two-dimensional base case with domain $[0,0] \times [L_x, L_y]$ in space and $[0,T]$ in time should be equivalent to the case defined in one dimension. This is achieved by setting $L_x = L_y = L = 100\,\mathrm{m}$ and dividing the domain into 100 grid blocks in each spatial direction, yielding a 100×100 grid. In addition, the same time step length as for the one-dimensional case is used, and we assume that all functions are independent of y, i.e. that $\alpha_{c0}(x,y) = \alpha_{c0}(x)$, $a_0(x,y) = a_0(x)$, $n_0(x,y) = n_0(x)$ and $m_0(x,y) = m_0(x)$.

The corresponding initial state for the cell volume fraction in two dimensions is shown in Fig. 3.10.

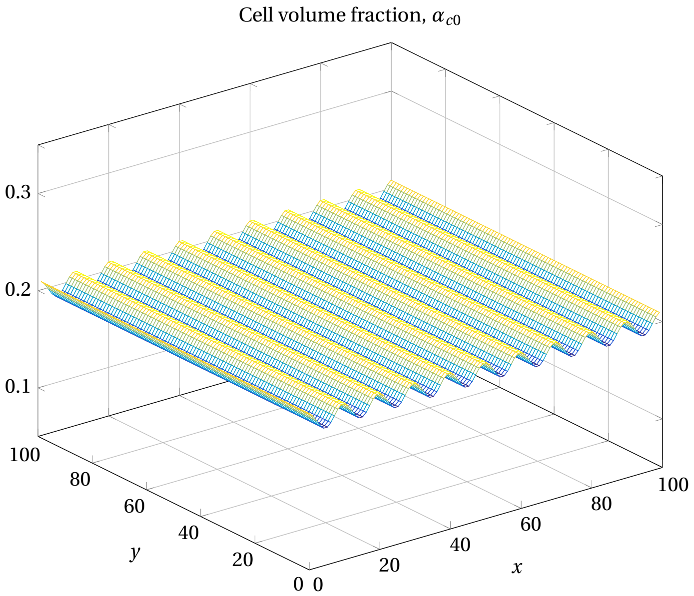

Fig. 3.10. A plot of the initial data (α_{c0}) for the two-dimensional base case.

Method I

The solution obtained using the first method (dimensional splitting) is shown for four different times in Fig. 3.11. Comparing this solution to the one-dimensional case in Fig. 3.6, we clearly see a similarity, where two distinct peaks eventually arise, reaching a value close to 0.8 for α_c at $t = 10\,000\,\text{s}$.

However, unwanted effects can be seen, especially for times $t = 7500\,\text{s}$ and $t = 10\,000\,\text{s}$ (figures 3.11c and 3.11d). In Fig. 3.11c we see a small peak appearing in the middle of the two larger peaks, approximately at $x = 50$, $y = 0$ (and also one at $x = 50$, $y = 100$) which ideally should not be there. This peak also causes ”bumps” to appear at the ends of the larger peaks (by ends meaning $y = 0$ and $y = 100$), an effect that also remain present after this smaller peak has disappeared (see Fig. 3.11d).

A possible cause to this unwanted effect could be explained by how we chose to treat the source term S_a when numerically solving $(2.30)_7$ (see page 31 for details). Using Method I, the source term was computed as $S_a = 1/2S_a + 1/2S_a$, an approximation that, as we can see, gave good results for the interior part of the domain, but could be the cause of unwanted effects appearing at the ends, especially seen for later times.

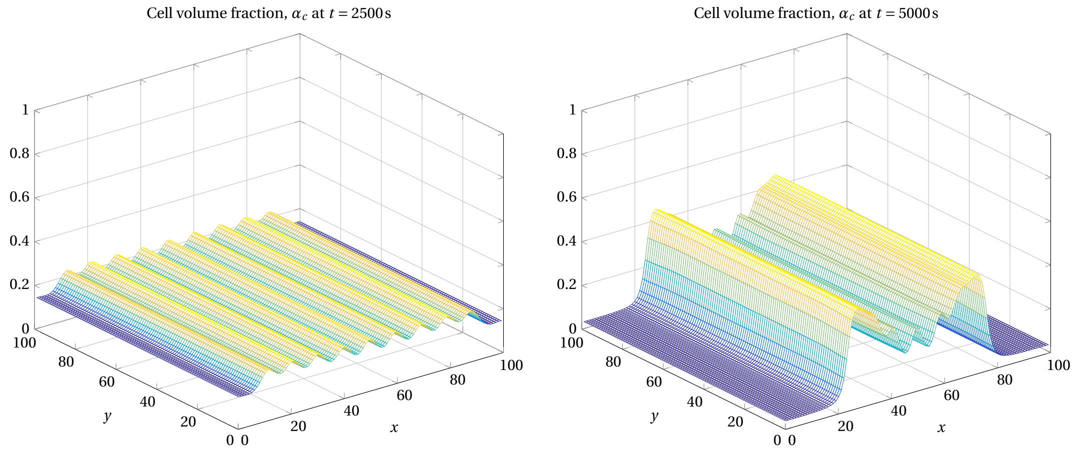

(a) $t = 2500\,\mathrm{s}$ **(b)** $t = 5000\,\mathrm{s}$

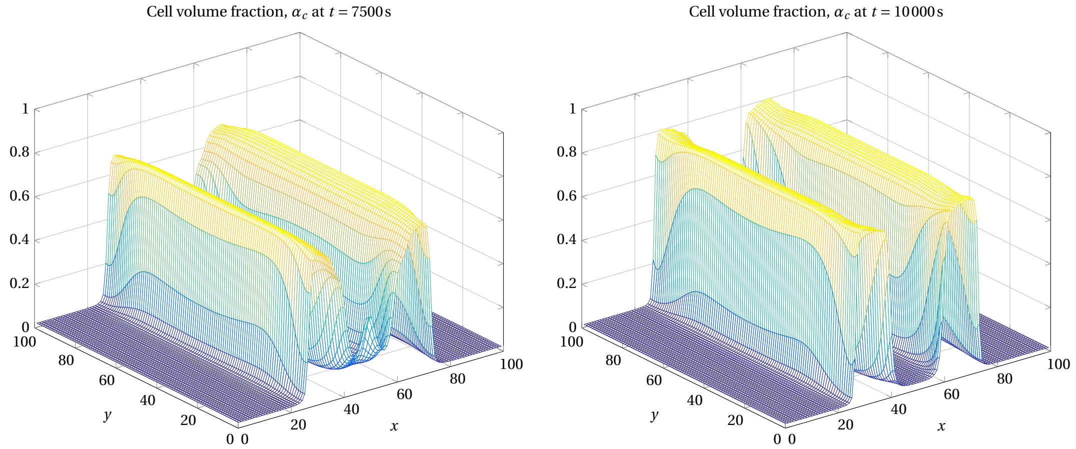

(c) $t = 7500\,\mathrm{s}$ **(d)** $t = 10\,000\,\mathrm{s}$

Fig. 3.11. Figures showing the evolution of α_c in two dimensions using Method I.

Method II

The simulated results using the Method II are shown in Fig. 3.12. Here, we see that although we include the shear stress terms in the momentum equations, the solution obtained using Method II is almost identical to that of Method I, except that the unwanted effects seen in Fig. 3.11c and 3.11d has vanished. This suggests that for the chosen base case, the role played by the shear stresses are negligible, and that by solving equations for both spatial directions simultaneously is benificial with regards to source terms.

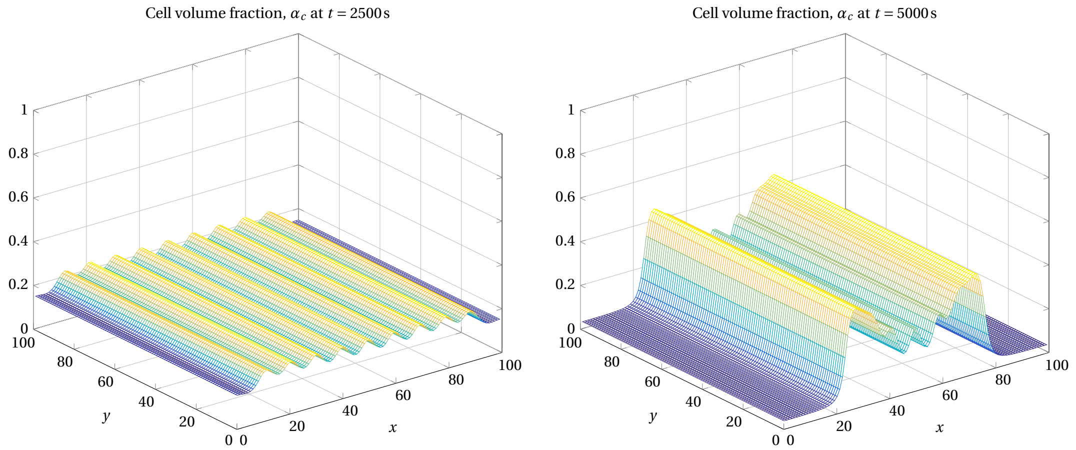

(a) $t = 2500$ s **(b)** $t = 5000$ s

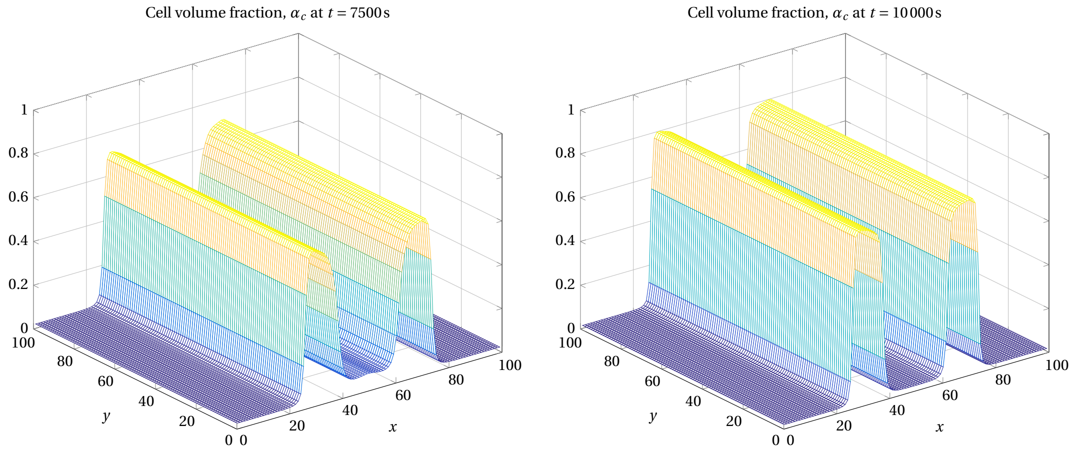

(c) $t = 7500$ s **(d)** $t = 10\,000$ s

Fig. 3.12. Figures showing the evolution of α_c in two dimensions using Method II.

Method III

By solving the base case using Method III, we get the solutions plotted in Fig. 3.13. The behavior observed in this figure is more or less identical to that of Method II in Fig. 3.12, substantiating the claim that the shear stress terms indeed are negligible for the chosen base case, and that it is the treatment of the source term S_a in Method I that induces the unwanted effect seen in Figures 3.11c and 3.11d.

Hence, methods II and III should be used in situations where the solution is expected to be sensitive to source terms, while Method II should be used when shear stresses are expected to be present.

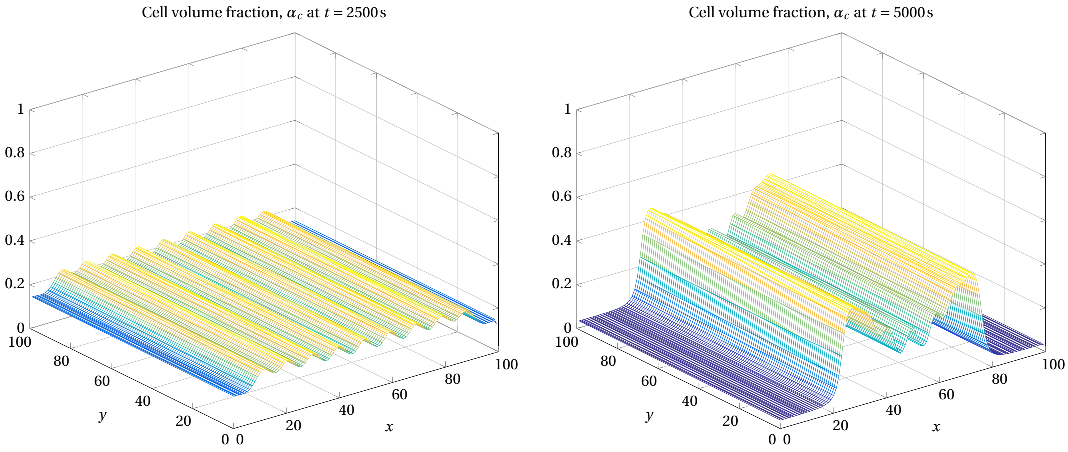

(a) $t = 2500\,\mathrm{s}$ **(b)** $t = 5000\,\mathrm{s}$

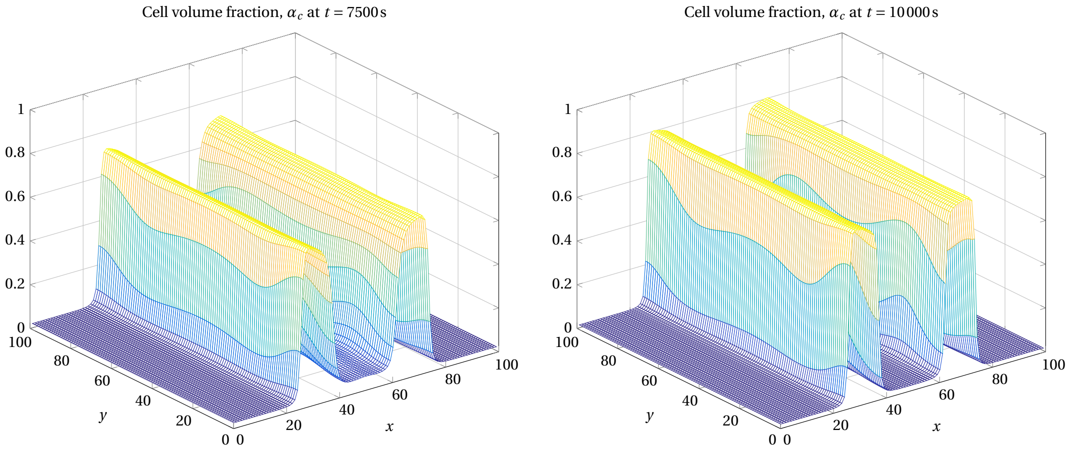

(c) $t = 7500\,\mathrm{s}$ **(d)** $t = 10\,000\,\mathrm{s}$

Fig. 3.13. Figures showing the evolution of α_c in two dimensions using Method III.

Chapter 4

Characteristic behavior of the model

In the previous chapter, the reason for developing a base case was to see to what degree the choice of solution method for the 2D model did affect the computed results, and to be able to compare results from the 2D model to the 1D model.

In this chapter, however, the aim is to do a more in-depth investigation of the behavior of the model, by looking at the response to change in parameters such as viscosity, shear stresses, boundary geometry, and initial data. The results will then be discussed in more detail in Chapter 6.

Unless stated otherwise, all simulations in this chapter are run with the input parameters listed in Table 3.1 on page 34 with boundary conditions and initial data as given in (2.28) and (2.29). Also, the initial concentration of the chemical agent has been set to $a_0(x,y) = 0.1$ for all simulations. The domain in space, $[0,0] \times [L_x, L_y]$, is divided into 100×100 grid blocks, and $L_x = L_y = L = 100\,\mathrm{m}$. The domain in time, $[0,T]$ is divided into $1.25 \cdot 10^6$ time steps, where $T = 10\,000\,\mathrm{s}$.

4.1 Effect of shear stress

When introducing the full model in 2D, extra terms arise in the momentum equations due to shear stress, compared to the 1D model. To investigate the effect of these terms, the initial data in the following case has been chosen with the purpose of invoking movement in both spatial directions simultaneously, in order to make sure that the cross derivatives in the momentum equations become non-zero. The proposed case has then been simulated using both Method II (with shear stress) and Method III (without shear stress) from Chapter 3. The initial cell volume fraction is given by

$$\alpha_{c0}(x,y) = 0.2 + 0.005\cos\left(\frac{2\pi x}{\omega L}\right) + 0.005\cos\left(\frac{2\pi y}{\omega L}\right), \tag{4.1}$$

and has been plotted in Fig. 4.1.

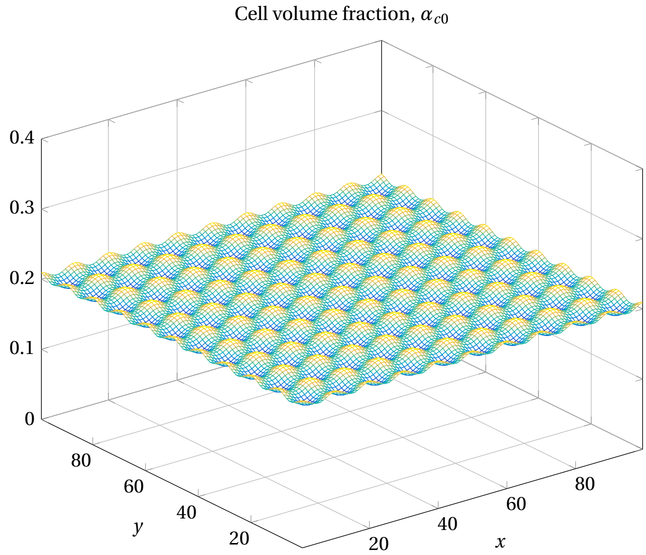

Fig. 4.1. A plot of the initial cell volume fraction given by (4.1).

The results obtained using Method III have been plotted in Fig. 4.2, while the results using Method II have been plotted in Fig. 4.3. For both these methods, the overall trend is more or less the same, with cells migrating towards the center of the domain, grouping together and forming one large cluster. However, for $t = 4000\,\mathrm{s}$ (Figures 4.2b and 4.3b) we can start to observe differences in the solution behavior of the two methods. The solution in Fig. 4.2b has more rounded corners and a relatively sharp transition in the cell volume fraction from $\alpha_c \approx 0.35$ to $\alpha_c = 0$, while the solution in Fig. 4.3b has formed a square shape with more distinct corners and a smoother transition between $\alpha_c \approx 0.35$ to $\alpha_c = 0$.

Moving forward in time, the shape of the solution in Fig. 4.2c has changed additionally compared to the initial square, while the solution in Fig. 4.3c has maintained its shape, only reducing in size.

At the end of the simulation, the solution using Method III has formed a more compact, 16-sided cluster (see Fig. 4.2d), while the solution using Method III only has compacted more towards the center of the domain, maintaining the square shape (see Fig. 4.3d).

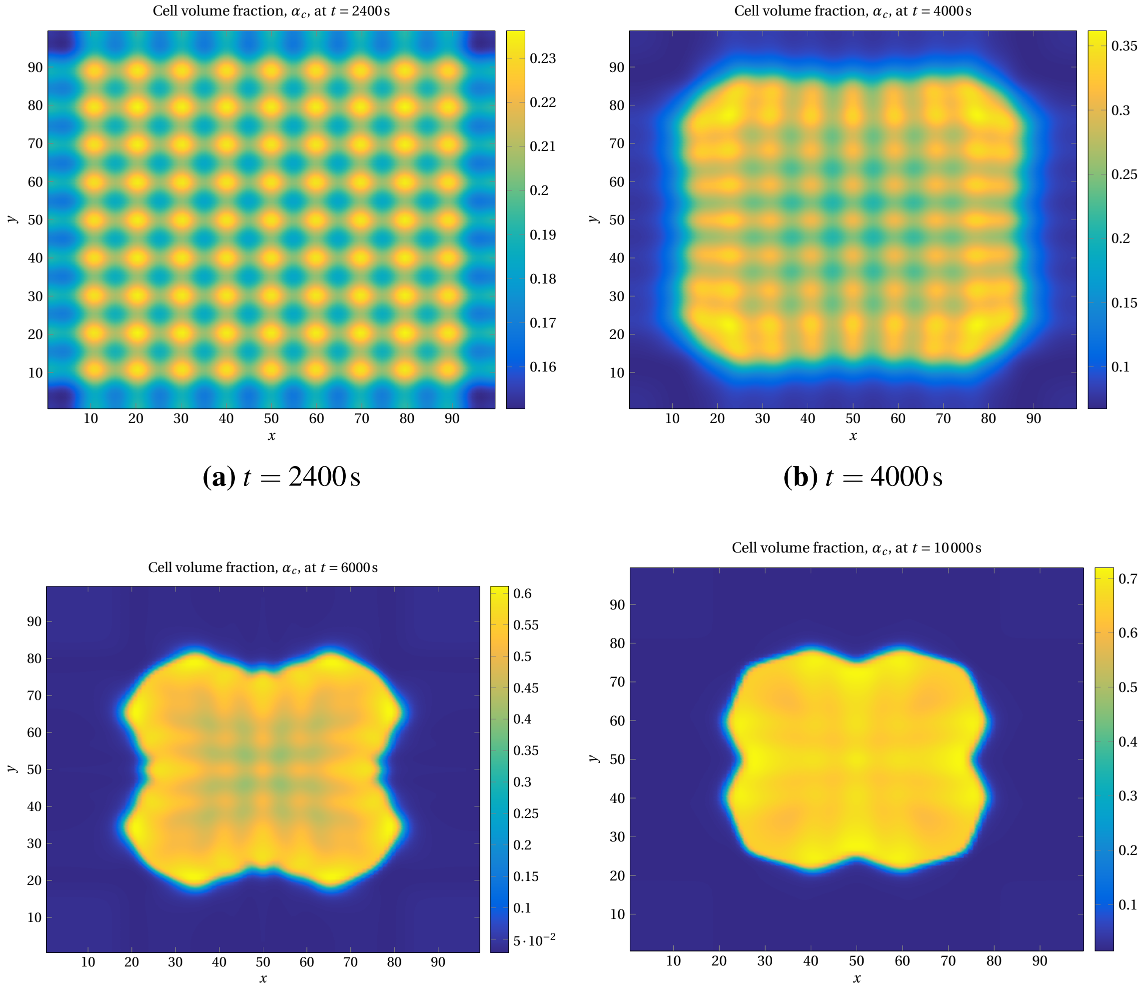

(a) $t = 2400\,\text{s}$ **(b)** $t = 4000\,\text{s}$

(c) $t = 6000\,\text{s}$ **(d)** $t = 10000\,\text{s}$

Fig. 4.2. Figures showing the evolution of α_c using Method III (no shear stresses present).

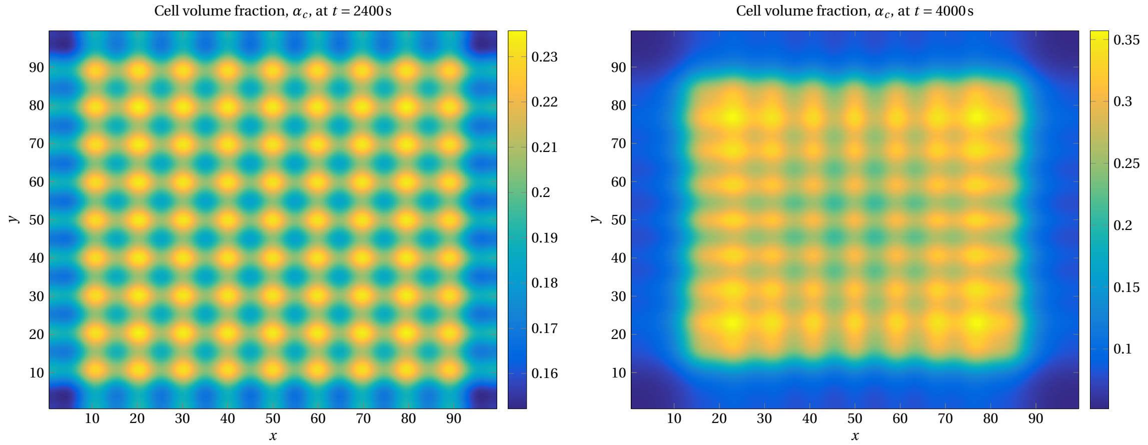

(a) $t = 2400\,\mathrm{s}$ **(b)** $t = 4000\,\mathrm{s}$

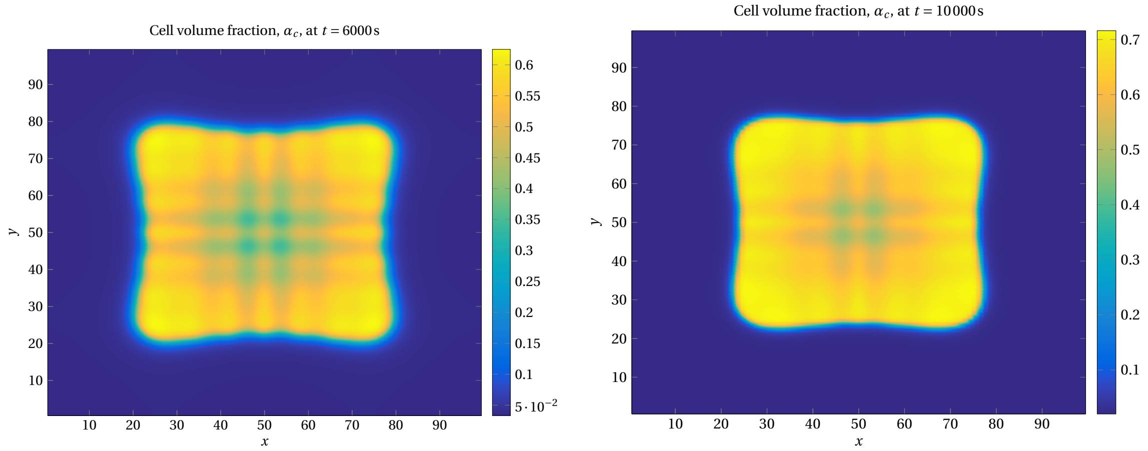

(c) $t = 6000\,\mathrm{s}$ **(d)** $t = 10\,000\,\mathrm{s}$

Fig. 4.3. Figures showing the evolution of α_c using Method II (with shear stress).

4.2 Effects of boundary geometry

The fact that in most physical cases, tumors or groups of cells take a more circular shape, while the standard boundary in Cartesian coordinates is square, causes the distance between tumor and boundary to vary, as illustrated in Fig. 4.4. Since the momentum equations are PDEs of elliptic type, the difference in distance to boundary could impact the solution already from the starting point of the simulation. For instance, consider the following elliptic boundary value problem:

$$\begin{aligned} \frac{\partial^2 u}{\partial x^2} &= 0, \qquad x \in [0, L], \\ u(0,t) &= T_1, \quad u(L,t) = T_2. \end{aligned}$$

When solving this problem we get

$$u(x,t) = T_1 + \left(\frac{T_2 - T_1}{L} \right) x,$$

and as we clearly can see, the solution is directly affected by the conditions imposed on the boundaries and the distance to these.

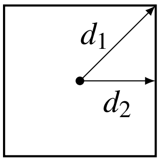

Fig. 4.4. Distance between circular shaped data and square boundary, where $d_1 > d_2$.

In order to investigate how this affects the solution, the initial cell volume fraction has been chosen to take a circular shape, given by the function

$$\alpha_{c0}(x,y) = \begin{cases} 0.2 + 0.01 \cos\left(\frac{2\pi\sqrt{(x-L/2)^2+(y-L/2)^2}}{\omega L} \right), & 0 \le \sqrt{(x-L/2)^2+(y-L/2)^2} \le L/2, \\ 0, & \text{otherwise} \end{cases} \tag{4.2}$$

as seen in Fig. 4.5. Simulations are then performed on both a square domain as described above, and on a circular domain with radius equal to $L/2$. The idea here is that any difference in solution will solely be effects related to the boundary geometry, where the distance from center to boundary varies for the square domain, but remain constant for the circular domain. In both these cases, the model has been solved using Method I (dimensional splitting).

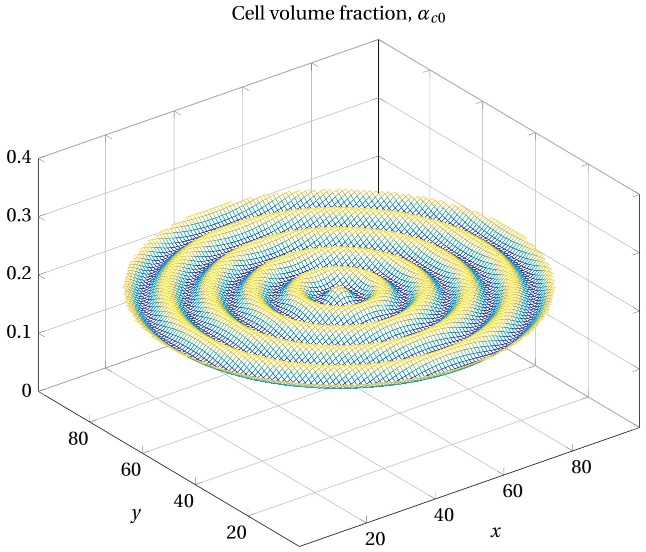

Fig. 4.5. A plot of the circular initial data given by (4.2).

The simulated results for a square domain has been plotted for α_c in Fig. 4.6 and for the chemical agent in Fig. 4.7.
For $t = 800\,\mathrm{s}$ we see some cells migrate towards the corners (light blue color in Fig. 4.6a), which initially had a cell volume fraction of 0. Then, at $t = 1600\,\mathrm{s}$, the movement has changed direction towards the center of the domain as a response to a positive gradient in the concentration of the chemical agent (see Fig. 4.7a), i.e. chemotaxis, but in a more square-like shape, rotated 45° relative to the boundary. In addition, cells located at the center of the domain has started to migrate outwards, similar to what was observed in Fig. 3.9 on page 38, when using the model in polar coordinates. A continuation of this behavior is seen in Fig. 4.6c for $t = 2400\,\mathrm{s}$, while for the final state at $t = 10\,000\,\mathrm{s}$, four connected peaks have formed, being located close to the midpoint of each side of the domain (see Fig. 4.6d).

By solving the exact same case on a circular shaped domain, we obtain the results shown in Fig. 4.8 Here, the main difference is that the initial cell volume fraction is spread over the entirety of the domain, so that there will not be any migration of cells towards empty areas as we saw happen in Fig. 4.6a. For $t = 1600\,\mathrm{s}$ (Fig. 4.8b) we see almost the same type of behavior as in Fig. 4.6b, where a square-like shape starts to evolve, now with the corners a little further away from the center. Also, cells initially located at the center of the domain migrate outwards, as previously seen in Fig. 4.6 and in Fig. 3.9 for the model in polar coordinates. In Fig. 4.8d we see that the four peaks from Fig. 4.8c has separated into four larger peaks located closer to the boundaries of the domain, and four smaller peaks positioned in the middle between these larger peaks.

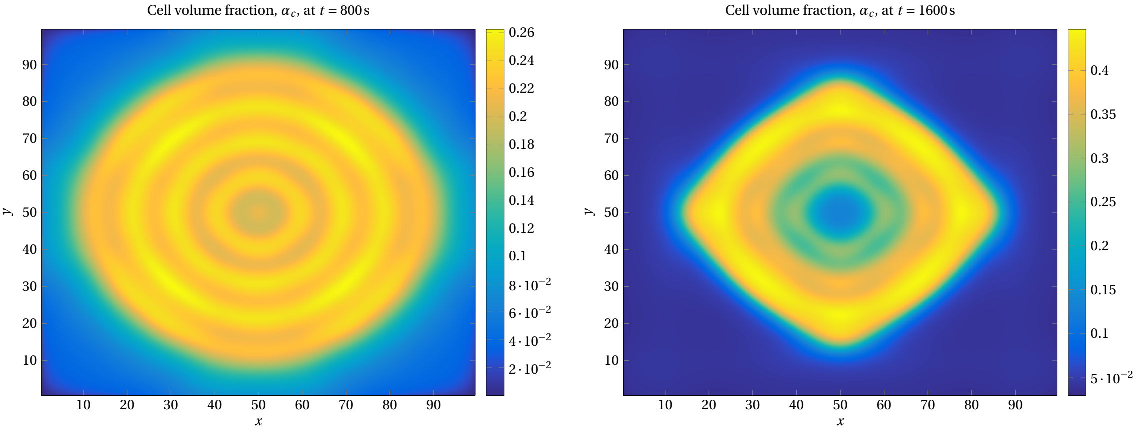

(a) $t = 800\,\mathrm{s}$ **(b)** $t = 1600\,\mathrm{s}$

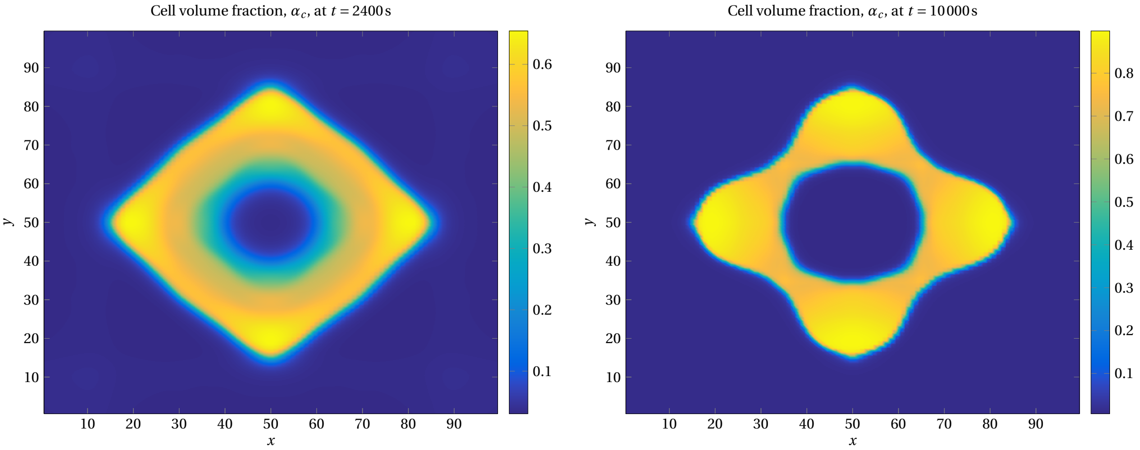

(c) $t = 2400\,\mathrm{s}$ **(d)** $t = 10\,000\,\mathrm{s}$

Fig. 4.6. Figures showing the evolution of α_c for the initial data given in (4.2) on a square boundary geometry.

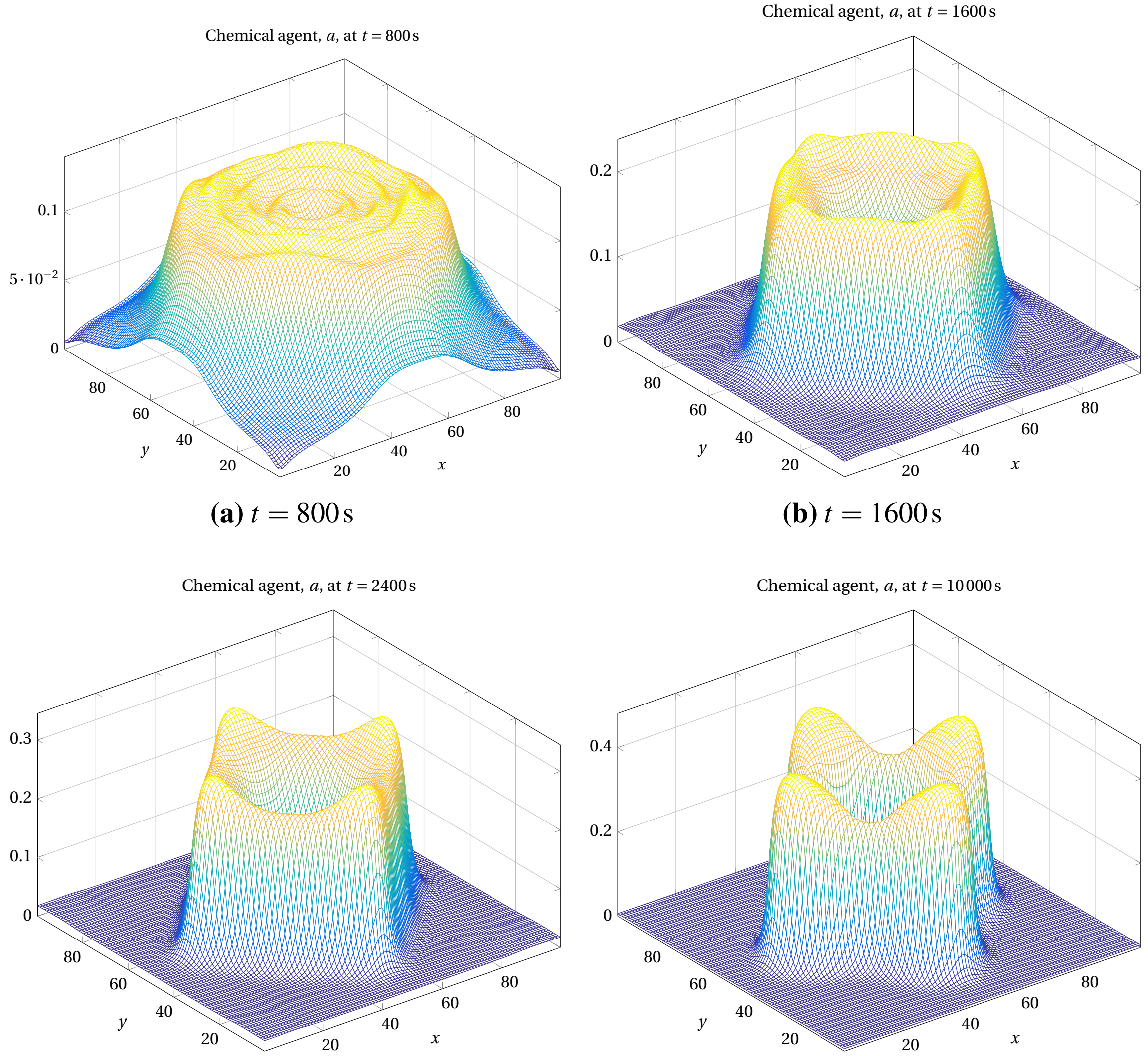

(a) $t = 800\,\text{s}$ **(b)** $t = 1600\,\text{s}$

(c) $t = 2400\,\text{s}$ **(d)** $t = 10000\,\text{s}$

Fig. 4.7. Figures showing the evolution in a for the initial data given in (4.2) on a square boundary geometry.

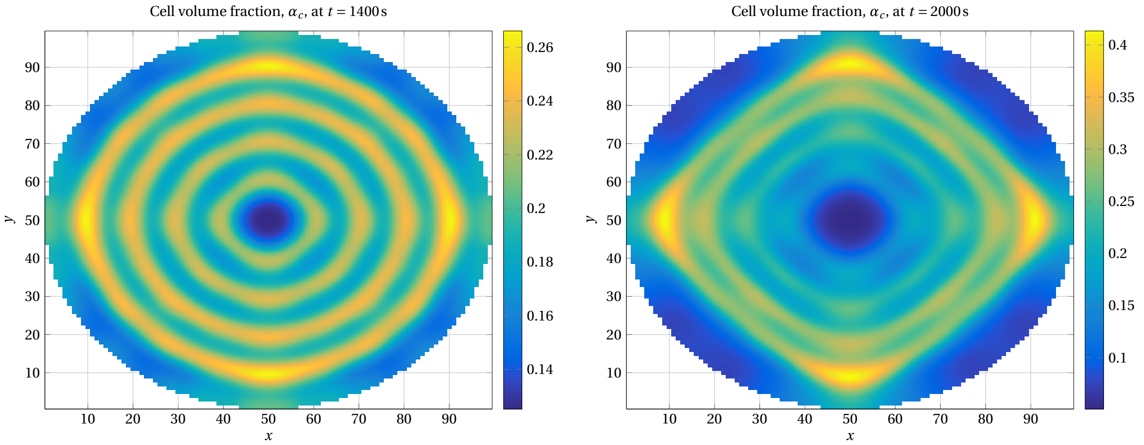

(a) $t = 1400\,\mathrm{s}$ **(b)** $t = 2000\,\mathrm{s}$

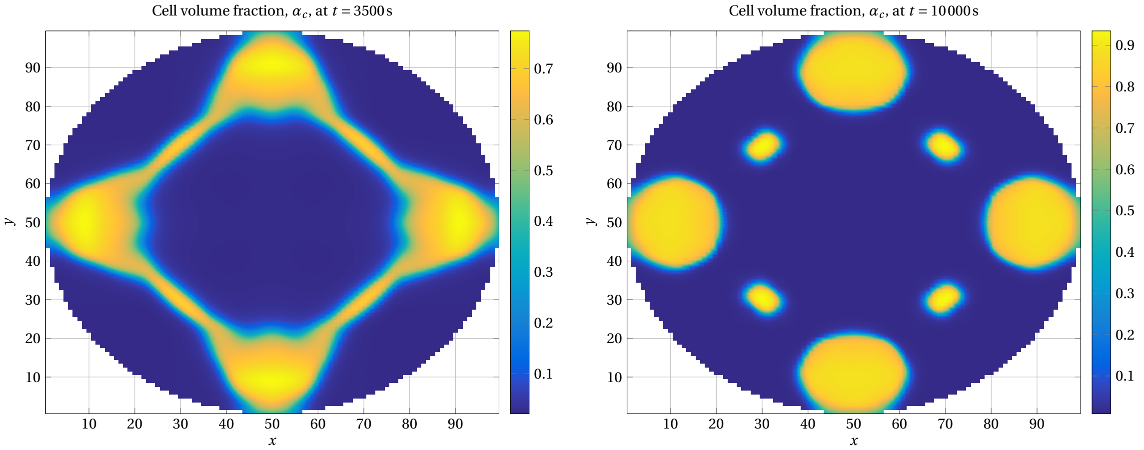

(c) $t = 3500\,\mathrm{s}$ **(d)** $t = 10\,000\,\mathrm{s}$

Fig. 4.8. Figures showing the evolution of α_c for the initial data given in (4.2) on a circular boundary geometry.

As the non-zero part of (4.2) was limited to $0 \le \sqrt{(x-L/2)^2+(y-L/2)^2} \le L/2$, we saw that for the square domain some of the cells first moved towards the corners before returning to the center. To see the effect of non-zero initial data being distributed over the entirety of the square domain, a new simulation was run where

$$\alpha_{c0}(x,y) = 0.2 + 0.01\cos\left(\frac{2\pi\sqrt{(x-L/2)^2+(y-L/2)^2}}{\omega L}\right). \tag{4.3}$$

This initial data has been plotted in Fig. 4.9, while the computed results are shown in Fig. 4.10.

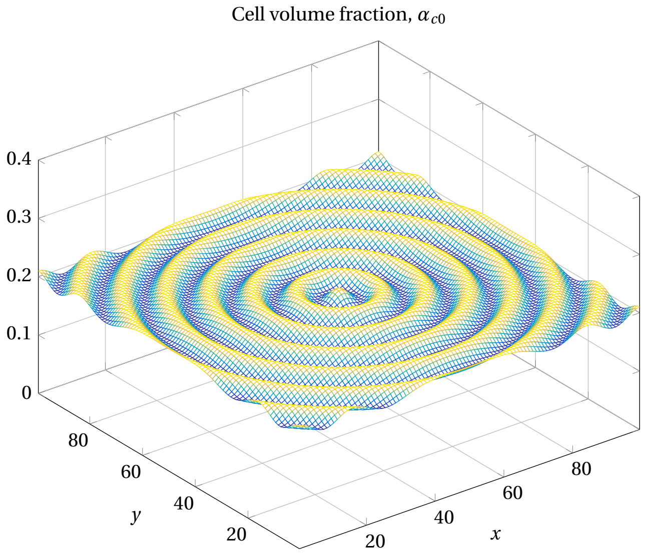

Fig. 4.9. A plot of the initial cell volume fraction given in (4.3).

The results in this figure shows a quite significant difference in behavior from that of Fig. 4.6 and Fig. 4.8, even though the initial data is relatively similar. In Fig. 4.6 and Fig. 4.8 we saw that at some time all the cells formed a more square shape (see Fig. 4.6b and Fig. 4.8c), a behavior that was not observed in Fig. 4.10, where the cells started grouping together into several smaller clusters (see Fig. 4.10c,4.10d). These clusters then continues to grow as shown in Fig. 4.10e and Fig. 4.10f, without changing shape or orientation to any significant extent.

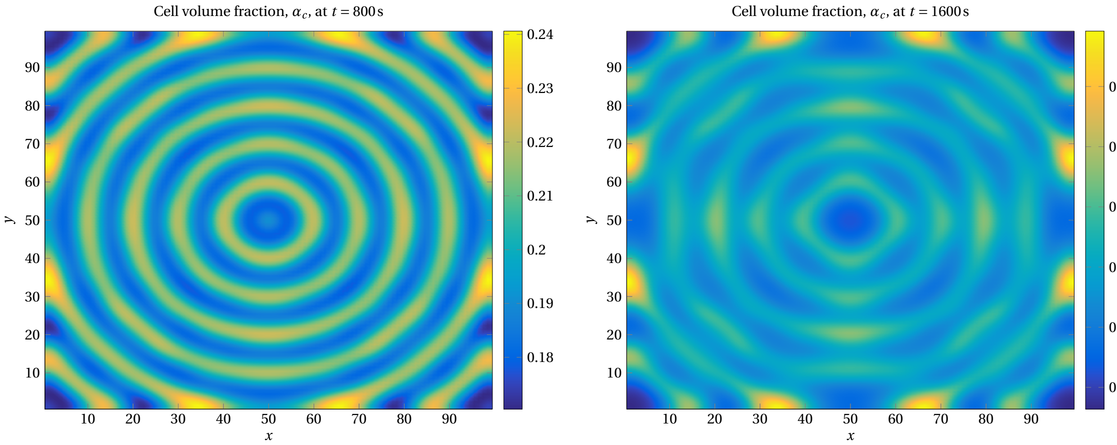

(a) $t = 800\,\mathrm{s}$ **(b)** $t = 1600\,\mathrm{s}$

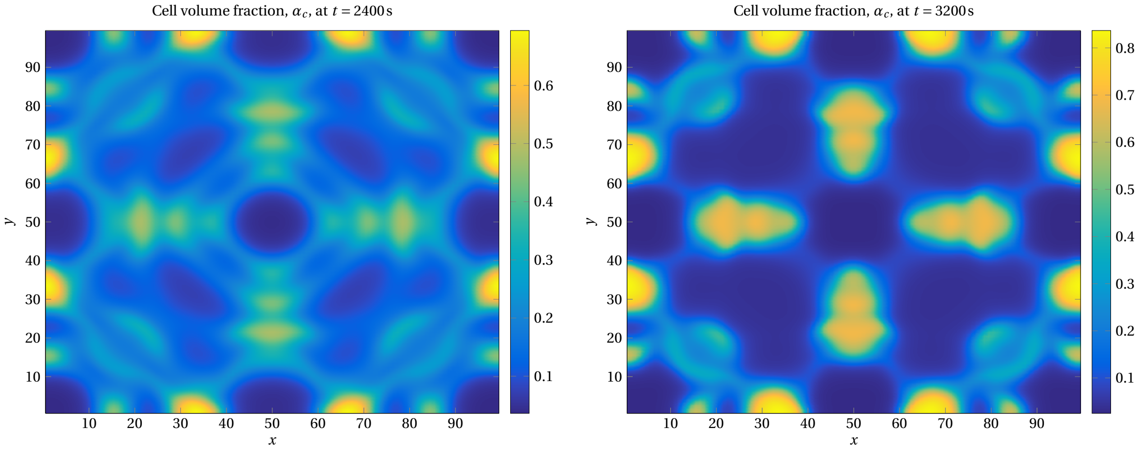

(c) $t = 2400\,\mathrm{s}$ **(d)** $t = 3200\,\mathrm{s}$

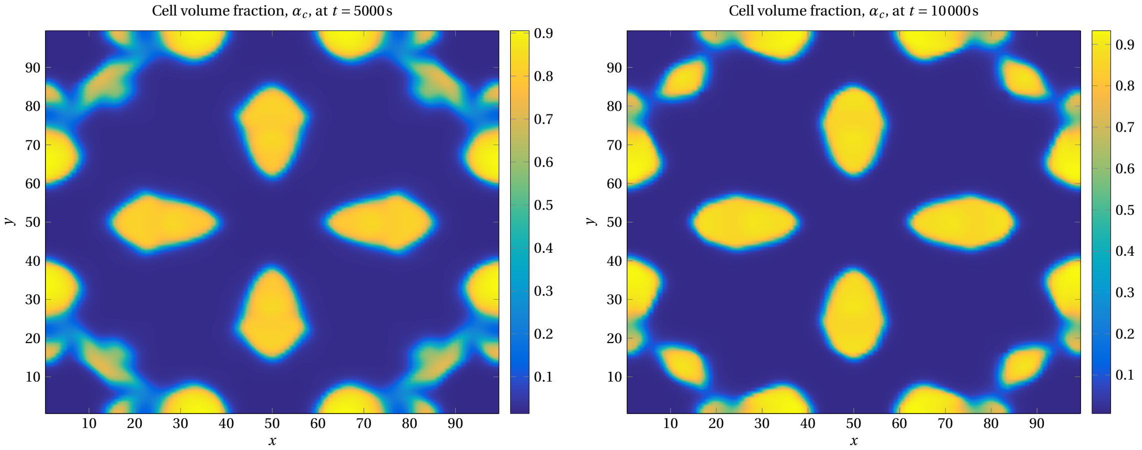

(e) $t = 5000\,\mathrm{s}$ **(f)** $t = 10\,000\,\mathrm{s}$

Fig. 4.10. Figures showing the evolution of α_c in for the initial data given in (4.3) using Method I.

4.3 Effect of viscosity

In the previous sections we have looked at the effects of shear stress and boundary geometry using two separate cases, in this section however, we will use a single case to further investigate these effects in addition to the effect of viscosity. The spatial domain is the same as described in the beginning of this chapter, while the domain in time $[0,T]$ now has been divided into 375000 time steps, where $T = 3000\,\mathrm{s}$, maintaining the same time step length as for the other cases in this chapter.

The behavior of the chosen case is more similar to that of a growing tumor, with an initial cell volume fraction that takes the shape of half an ellipsoid, given by

$$\alpha_{c0}(x,y) = \begin{cases} 0.35\left(1-\left(\frac{x-50}{15}\right)^2-\left(\frac{y-50}{15}\right)^2\right), & 0 \leq \sqrt{(x-L/2)^2+(y-L/2)^2} \leq 15, \\ 0, & \text{otherwise}, \end{cases} \tag{4.4}$$

as seen in Fig. 4.11.

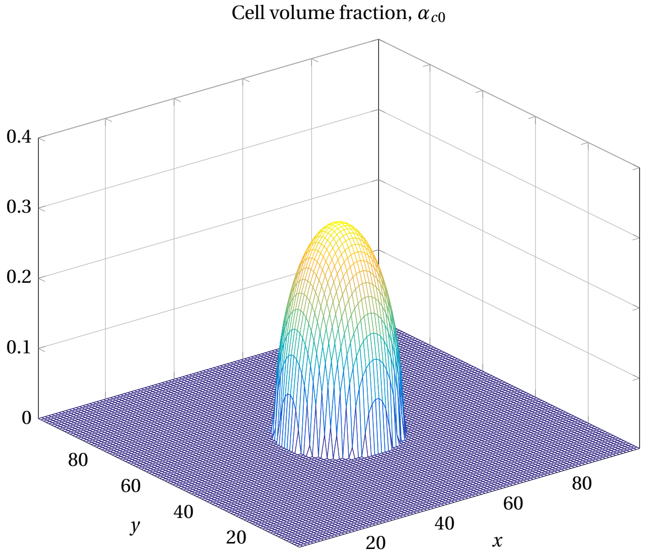

Fig. 4.11. A plot of the initial cell volume fraction for the circular case.

As for the mass balance equations, we will for this case assume that cells (or cell phase) grow logistically, i.e. that the rate of which cells are produced (growth) is proportional to both the existing cell population and the amount of available resources, which in this case corresponds to areas where the population density of cells is low [50]. Hence, the mass balance equations take the form

$$
\begin{aligned}
&\frac{\partial n}{\partial t} + \nabla \cdot (n\vec{u}_c) = S_c(\alpha_c), \\
&\frac{\partial m}{\partial t} + \nabla \cdot (m\vec{u}_w) = -S_c(\alpha_c),
\end{aligned}
\tag{4.5}
$$

where the source term $S_c(\alpha_c)$ is given by

$$
S_c(\alpha_c) = c_1(1-\alpha_c)\alpha_c, \tag{4.6}
$$

in which c_1 is a constant.

Here, $c_1(1-\alpha_c)$ corresponds to the proliferation rate of the cells, and thus we expect cells to grow at a higher rate in areas where α_c is low, and at a lower rate in areas where α_c is high.

As for the input parameters, some of them has been slightly changed compared to the base case values in Table 3.1 (page 34), in order to make sure that the spatial radius of the initial data will increase with time. In Table 4.1 these changed input parameters have been listed along with the value of c_1, while other parameters take the values given in Table 3.1. This case has then been solved using different solution methods, as well as different boundary geometries and viscosity values. The results obtained has then been plotted at times for which the tumor radius is of similar magnitude, in order to better be able to compare the results.

Table 4.1. Input parameters:

Parameter	Value	Unit
k	5	s^{-1}
λ	15	$\mathrm{m}^3\,\mathrm{mol}^{-1}$
c_1	0.8	$\mathrm{kg}\,\mathrm{m}^{-3}\,\mathrm{s}^{-1}$
D_a	0.8	$\mathrm{m}^2\,\mathrm{s}^{-1}$
ε_c	$5 \cdot 10^4$	$\mathrm{m}^2\,\mathrm{s}^{-1}$
ε_w	$5 \cdot 10^4$	$\mathrm{m}^2\,\mathrm{s}^{-1}$

In Fig. 4.12, the result has been obtained using Method I. As we clearly can see, the initial circular shape has become more square, similar to the shape of the boundary. This is the case both for $t = 1500\,\mathrm{s}$ and $t = 2100\,\mathrm{s}$ (see Fig. 4.12).

In the next figure, Fig. 4.13 we have used the same solution method as in Fig. 4.12, but here the viscosities ε_c and ε_w have been reduced by a factor 10, i.e. $\varepsilon_c = \varepsilon_w = 5 \cdot 10^3\ \mathrm{m}^2\,\mathrm{s}^{-1}$. The solution for $t = 180\,\mathrm{s}$ and $t = 240\,\mathrm{s}$ has been plotted in Fig. 4.14. In this figure, the first

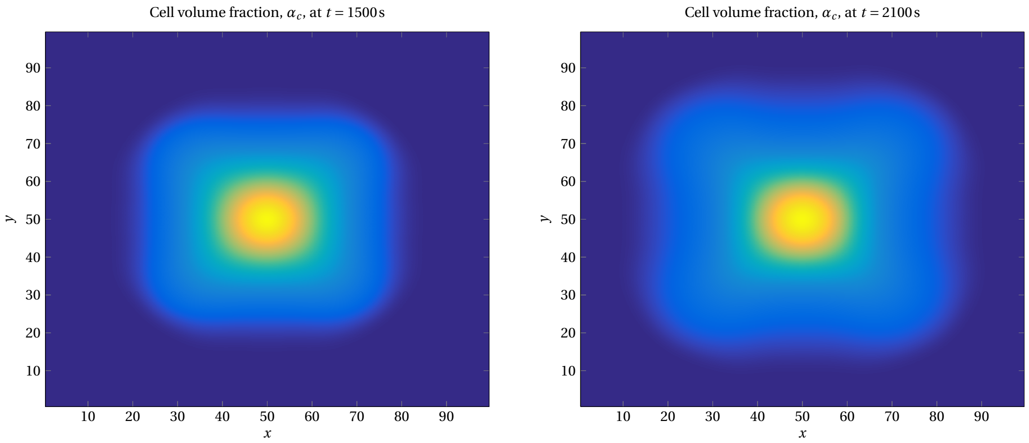

Fig. 4.12. Plots for times $t = 1500$ s (left) and $t = 2100$ s (right) using Method I on a square domain.

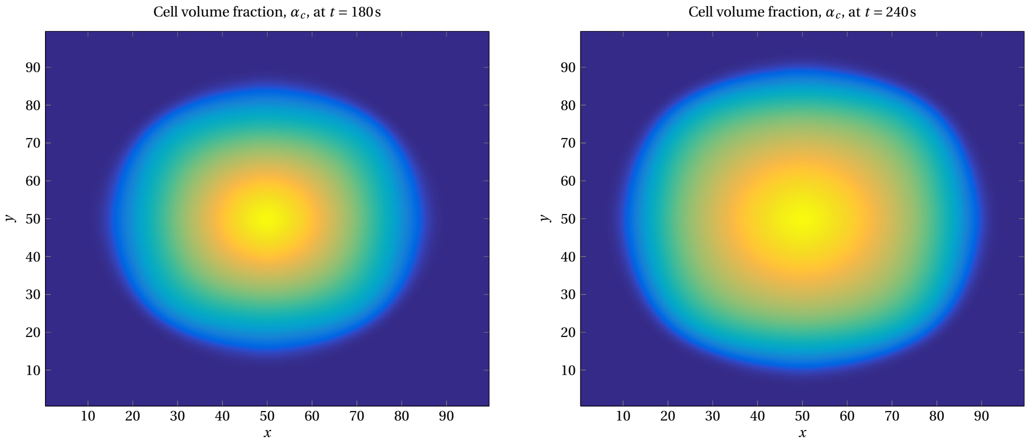

Fig. 4.13. Plots for times $t = 180$ s (left) and $t = 240$ s (right) using Method I with reduced viscosity on a square domain with.

thing to note is that the cell phase has almost reached the boundary after only 240 s, having grown at a rate approximately 10 times higher than in Fig. 4.12. Another observations is that the solution for both times plotted takes a more circular shape, closer to that of the initial data.

In Fig. 4.14 the case has been solved using Method I, but now on a circular domain with radius equal to $L/2$. Here we see that even though the domain is circular, the solution is more or less identical to that for a square domain, seen in Fig. 4.12.

The solutions plotted in Fig. 4.15 has been obtained by using Method II on a square domain. In this figure we see that the solution maintains a more or less completely circular shape, both for $t = 2400$ s and $t = 3000$ s (end of simulated period). We also note that the growth rate is ~ 0.8 of that in Fig. 4.12 where Method I was used.

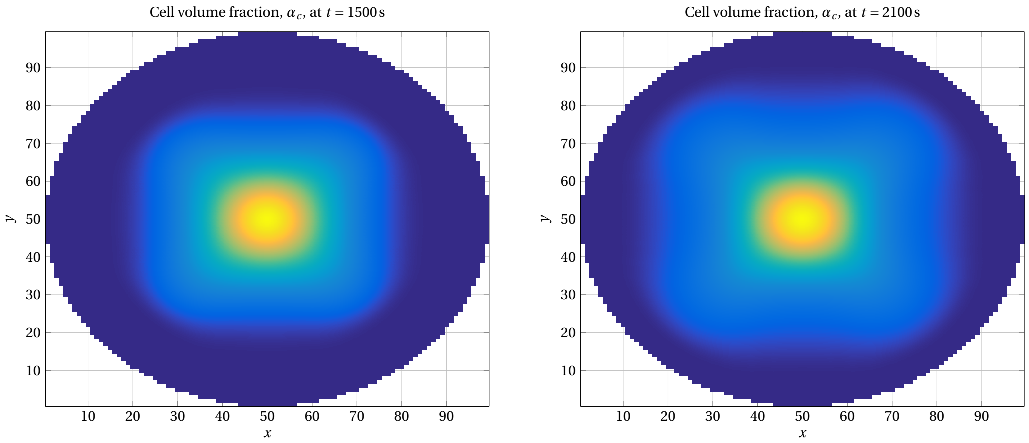

Fig. 4.14. Plots for times $t = 1500\,\mathrm{s}$ (left) and $t = 2100\,\mathrm{s}$ (right) using Method I on a circular domain.

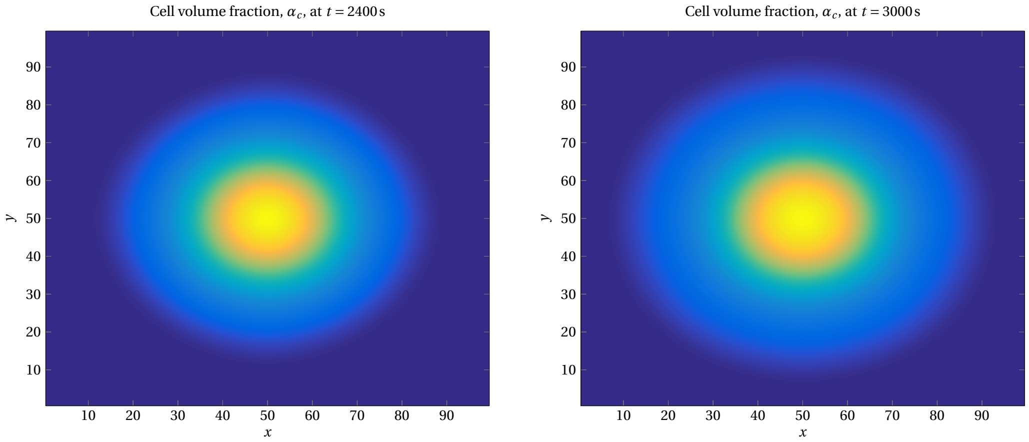

Fig. 4.15. Plots for times $t = 2400\,\mathrm{s}$ (left) and $t = 3000\,\mathrm{s}$ (right) using Method II on a square domain.

In order to more carefully investigate if the differences between solutions in Fig. 4.12 and Fig. 4.15 were caused by shear stresses, or if they rather were effects caused by the dimensional splitting approach used in Method I, a new simulation was run using Method II, where the shear stress terms had been taken out of the momentum equations. In other words, by using same analogy as in Section 3.1.3, we obtained an approximation $U^{n+1} \approx U(x,y,t^{n+1})$ by the following sequence of operators:

$$U^{n+1} = T_{2\mathrm{D}}^{\Delta t} U^n,$$

where the operator $T^{\Delta t}_{\mathrm{2D}}$ is associated with the following model

$$T^{t}_{\mathrm{2D}}:\begin{cases}\partial_t n+\nabla\cdot(n\vec{u}_c)=0,\\ \partial_t m+\nabla\cdot(m\vec{u}_w)=0,\\ \partial_x\left[\alpha_c\Lambda(a)\right]+\alpha_c\partial_x P=\hat{k}(u^x_w-u^x_c)+2\varepsilon_c\partial_x\left(n\partial_x u^x_c\right),\\ \partial_y\left[\alpha_c\Lambda(a)\right]+\alpha_c\partial_y P=\hat{k}(u^y_w-u^y_c)+2\varepsilon_c\partial_y\left(n\partial_y u^y_c\right),\\ \alpha_w\partial_x P=-\hat{k}(u^x_w-u^x_c)+2\varepsilon_w\partial_x\left(m\partial_x u^x_w\right),\\ \alpha_w\partial_y P=-\hat{k}(u^y_w-u^y_c)+2\varepsilon_w\partial_y\left(m\partial_y u^y_w\right),\\ \partial_t a=D_a\nabla^2 a+S_a(a,n).\end{cases}$$

The results from using this approach has been plotted in Fig. 4.16. As we can see, the square shaped results in Fig. 4.16 are more or less identical to those in Fig. 4.12 and Fig. 4.14 where Method I has been used, compared to the results in Fig. 4.15.

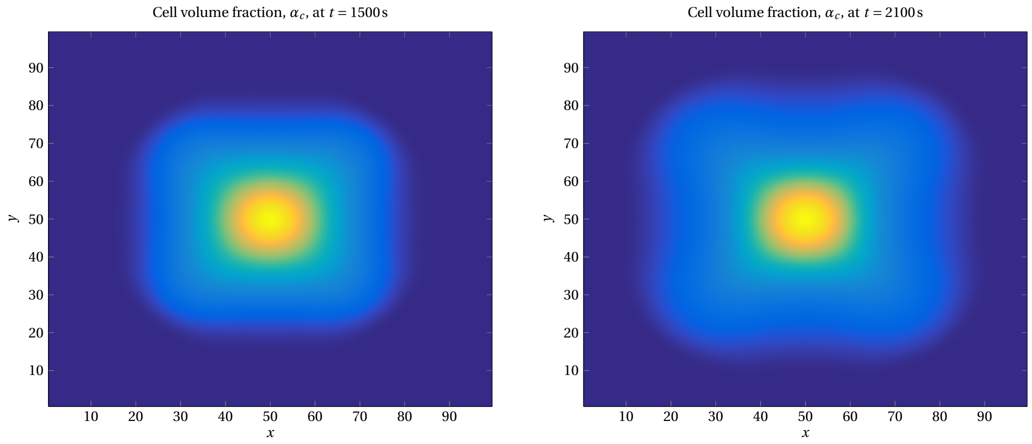

Fig. 4.16. Plots for times $t = 2400$ s (left) and $t = 3000$ s (right) using Method II without shear stress terms, on a square domain.

Chapter 5

Relating the mathematical model to physical experiments

In this chapter we investigate to what extent the model derived in Chapter 2 is able to replicate experimental behavior observed in [9], where, among other things, the growth of single cancer cells in 0.5% agarose gel was recorded over a time span of 30 days.

We start this chapter by presenting the most important observations made in [9] relative to our investigations, before continuing by rewriting the mathematical model in dimensionless form. The selected input parameters are then listed along with initial data, before presenting simulated results using both the 1D and 2D models, where methods II og III has been used for solving the latter of these. The discussion of the results will then take place in Chapter 6.

5.1 Key experimental observations

Fig. 5.1 shows the growth of a typical tumor spheroid (green) co-embedded with micro beads (red) in 0.5% agarose gel for 30 days, from experiments performed by Cheng et al. in [9]. The use of co-embedded micro-beads (diameter=1 μm) allows for the spatial distribution of compressive stress around the tumor to be estimated, based on changes in micro-bead density (consult [9] for more information about the experimental setup).

The focus in this chapter is to investigate to what extent the mathematical model can (i) replicate the evolution in tumor diameter with time, and (ii) model the corresponding pressure response, based on the observations made in [9].

With regards to tumor growth, they reported that the tumor had grown to a diameter of $\sim$ 150 μm after 17 days, and by day 30, the diameter had increased to $\sim$ 250 μm.

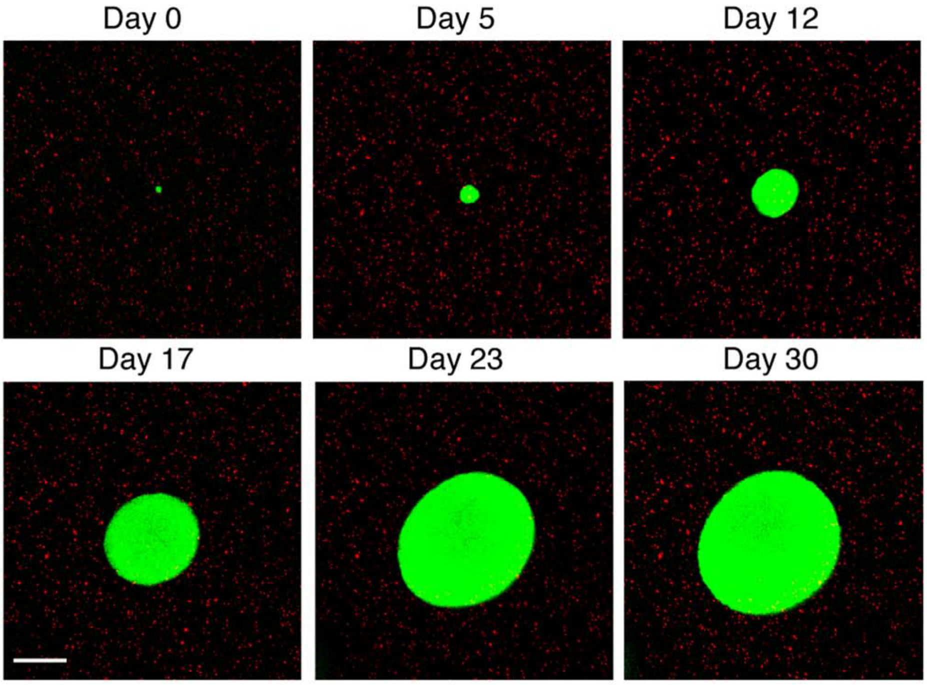

Fig. 5.1. A growing spheroid (green) and its surrounding micro-beads (red). Scale bar = 100 µm. Figure from [9].

For the pressures, it was estimated that the spheroid imposed ~ 28 mmHg (~ 3.7 kPa) of solid stress on the immediate adjacent matrix (day 30), and also that this was limited to the immediate vicinity of the spheroid, decreasing to its control level within ~ 50 µm from the spheroid surface.

It was also observed that cell proliferation (cell growth) was suppressed and that apoptotic cell death was induced in regions of high mechanical stress, suggesting that the stress level play an important role in tumor spheroid growth dynamics.

5.2 Non-dimensionalization

When relating the mathematical model to the experimental data in [9], it is beneficial to rewrite the model in dimensionless form in order to assess the relative importance of the different parameters, and to scale the simulated results such that they are of the same order of magnitude as the experimental data in [9]. In this section this is done for the 1D model, however the dimensionless model in 2D is obtained by using the same approach.

First, we introduce the dimensionless variables

$$\begin{aligned} \tilde{x} = \frac{x}{L_*}, \qquad \tilde{t} = \frac{t}{T_*}, \qquad \tilde{P} = \frac{P}{P_*}, \qquad \tilde{a} = \frac{a}{a_*}, \\ \tilde{\rho}_l = \frac{\rho_l}{\rho_*}, \qquad \tilde{u}_l = \frac{u_l}{u_*}, \qquad l = c, w \end{aligned} \tag{5.1}$$

where L_*, T_*, P_*, a_*, ρ_*, u_* are the characteristic length, time, pressure, concentration, density and velocity, respectively, with dimensions $[L_*] = L$, $[T_*] = T$, $[P_*] = ML^{-1}T^{-2}$, $[a_*] = NL^{-3}$, $[\rho_*] = ML^{-3}$, $[u_*] = LT^{-1}$. Further, the dimensionless masses, $\tilde{n}$ and $\tilde{m}$ takes the form $\tilde{n} = \alpha_c\tilde{\rho}_c$ and $\tilde{m} = \alpha_w\tilde{\rho}_w$.

Including the source term (4.6) that accounts for growth and death of cells, the mass balance equations can now be written as

$$\begin{aligned} \frac{\partial \tilde{n}}{\partial \tilde{t}} + \frac{T_* u_*}{L_*}\frac{\partial(\tilde{n}\tilde{u}_c)}{\partial \tilde{x}} &= \frac{T_*}{\rho_*}S_c(\alpha_c) \\ \frac{\partial \tilde{m}}{\partial \tilde{t}} + \frac{T_* u_*}{L_*}\frac{\partial(\tilde{m}\tilde{u}_w)}{\partial \tilde{x}} &= -\frac{T_*}{\rho_*}S_c(\alpha_c). \end{aligned}$$

To further simplify these equations, we introduce

$$\tilde{S}_c(\alpha_c) = \tilde{c}_1\alpha_c(1-\alpha_c), \qquad \text{where } \tilde{c}_1 = \frac{T_*}{\rho_*}c_1,$$

and choose $T_* = L_*/u_*$, so that

$$\begin{aligned} \frac{\partial \tilde{n}}{\partial \tilde{t}} + \frac{\partial(\tilde{n}\tilde{u}_c)}{\partial \tilde{x}} &= \tilde{S}_c(\alpha_c), \\ \frac{\partial \tilde{m}}{\partial \tilde{t}} + \frac{\partial(\tilde{m}\tilde{u}_w)}{\partial \tilde{x}} &= -\tilde{S}_c(\alpha_c), \qquad 0 \le \tilde{x} \le 1, \qquad \tilde{t} \ge 0. \end{aligned}$$

Performing the same type of routine on the momentum equations we get

$$\begin{aligned} \frac{1}{P_*}\frac{\partial}{\partial \tilde{x}}[\alpha_c\Lambda(a)] + \alpha_c\frac{\partial \tilde{P}}{\partial \tilde{x}} &= \frac{L_* u_*}{P_*}\hat{k}(\tilde{u}_w - \tilde{u}_c) + 2\varepsilon_c\frac{\rho_* u_*}{L_* P_*}\left(\tilde{n}\frac{\partial \tilde{u}_c}{\partial \tilde{x}}\right) \\ \alpha_w\frac{\partial \tilde{P}}{\partial \tilde{x}} &= -\frac{L_* u_*}{P_*}\hat{k}(\tilde{u}_w - \tilde{u}_c) + 2\varepsilon_w\frac{\rho_* u_*}{L_* P_*}\left(\tilde{m}\frac{\partial \tilde{u}_w}{\partial \tilde{x}}\right). \end{aligned}$$

These are further simplified by introducing

$$\tilde{\Lambda}(\tilde{a}) = \tilde{\Lambda}_0 + \tilde{\Lambda}_1 e^{-\tilde{\lambda}\tilde{a}}, \qquad \begin{cases} \tilde{\Lambda}_0 = \frac{\Lambda_0}{P_*} \\ \tilde{\Lambda}_1 = \frac{\Lambda_1}{P_*} \\ \tilde{\lambda} = a_*\lambda \end{cases}$$

$$\tilde{\tilde{k}}(\tilde{n},\tilde{m}) = \tilde{k}\frac{\tilde{n}\tilde{m}}{\tilde{n}+\tilde{m}}, \qquad \text{where } \tilde{k} = k\frac{\rho_* L_* u_*}{P_*}$$

and

$$\tilde{\varepsilon}_l = \varepsilon_l \frac{\rho_* u_*}{L_* P_*}, \qquad l = c, w$$

giving

$$\begin{aligned} \frac{\partial}{\partial \tilde{x}}\left[\alpha_c \tilde{\Lambda}(\tilde{a})\right] + \alpha_c \frac{\partial \tilde{P}}{\partial \tilde{x}} &= \tilde{\tilde{k}}\left(\tilde{u}_w - \tilde{u}_c\right) + 2\tilde{\varepsilon}_c\left(\tilde{n}\frac{\partial \tilde{u}_c}{\partial \tilde{x}}\right) \\ \alpha_w \frac{\partial \tilde{P}}{\partial \tilde{x}} &= -\tilde{\tilde{k}}\left(\tilde{u}_w - \tilde{u}_c\right) + 2\tilde{\varepsilon}_w\left(\tilde{m}\frac{\partial \tilde{u}_w}{\partial \tilde{x}}\right). \end{aligned}$$

The diffusion equation for the chemical agent takes the form

$$\frac{\partial \tilde{a}}{\partial \tilde{t}} = \frac{T_*}{L_*^2} D_a \frac{\partial^2 \tilde{a}}{\partial \tilde{x}^2} + \frac{T_*}{a_*} S_a(a,n),$$

and by letting

$$\tilde{D}_a = D_a \frac{T_*}{L_*^2} = \frac{D_a}{L_* u_*},$$

$$\tilde{S}_a(\tilde{a},\tilde{n}) = \tilde{s}_0\tilde{n} - \tilde{s}_1\tilde{a}, \qquad \text{where } \begin{cases} \tilde{s}_0 = s_0\frac{T_*\rho_*}{a_*} = s_0\frac{L_*\rho_*}{u_* a_*} \\ \tilde{s}_1 = s_1 T_* = s_1\frac{L_*}{u_*} \end{cases}$$

we get

$$\frac{\partial \tilde{a}}{\partial \tilde{t}} = \tilde{D}_a \frac{\partial^2 \tilde{a}}{\partial \tilde{x}^2} + \tilde{S}_a(\tilde{a},\tilde{n}).$$

Dropping tildes, the dimensionless model in 1D can be written as

$$
\begin{aligned}
\frac{\partial n}{\partial t}+\frac{\partial}{\partial x}(nu_c) &= S_c(\alpha_c)\\
\frac{\partial m}{\partial t}+\frac{\partial}{\partial x}(mu_w) &= -S_c(\alpha_c)\\
\frac{\partial}{\partial x}[\alpha_c\Lambda(a)]+\alpha_c\frac{\partial P}{\partial x} &= \hat{k}(u_w-u_c)+2\varepsilon_c\frac{\partial}{\partial x}\left(n\frac{\partial u_c}{\partial x}\right)\\
\alpha_w\frac{\partial P}{\partial x} &= -\hat{k}(u_w-u_c)+2\varepsilon_w\frac{\partial}{\partial x}\left(m\frac{\partial u_w}{\partial x}\right)\\
\frac{\partial a}{\partial t} &= D_a\frac{\partial^2 a}{\partial x^2}+S_a(a,n)
\end{aligned}
\tag{5.2}
$$

The solution procedure can then be summed up in three steps:

I. Perform simulations using the dimensionless model.

II. Choose appropriate values for the characteristic parameters based on the experimental data.

III. Rescale parameters and variables to physical quantities using the relations derived in this section.

5.3 Input parameters and initial data

The values of the characteristic parameters were chosen with data from the paper [9] in mind, and can be found in Table 5.1.

Table 5.1. Characteristic parameters:

Parameter	Value	Unit
L_*	$500\cdot 10^{-6}$	m
T_*	$24\cdot 3600$	s
P_*	10^4	Pa
a_*	1	$\mathrm{mol\,l^{-1}}$
ρ_*	1000	$\mathrm{kg\,m^{-3}}$
$u_*=\frac{L_*}{T_*}$	$5.787\cdot 10^{-9}$	$\mathrm{m\,s^{-1}}$

The physical input parameters that were found to give the best fit between simulated results and experimental observations, are given in Table 5.2. These parameters were chosen based on, (a) the fact that cells consist mostly of water, giving density and compressibility

Table 5.2. Physical input parameters:

Parameter	Value	Unit
k	1000	s^{-1}
Λ_0	1	Pa
Λ_1	$1 \cdot 10^4$	Pa
λ	10	$\mathrm{l\,mol}^{-1}$
s_0	$1 \cdot 10^{-5}$	$\mathrm{kmol\,kg}^{-1}\,\mathrm{s}^{-1}$
s_1	$2 \cdot 10^{-5}$	s^{-1}
c_1	$3.3 \cdot 10^{-3}$	$\mathrm{kg\,m}^{-3}\,\mathrm{s}^{-1}$
C_w	10^6	$\mathrm{m}^2\,\mathrm{s}^{-2}$
C_c	500	$\mathrm{m}^2\,\mathrm{s}^{-2}$
$\tilde{\rho}_{w0}$	999.9	$\mathrm{kg\,m}^{-3}$
$\tilde{\rho}_{c0}$	800	$\mathrm{kg\,m}^{-3}$
D_a	10^{-7}	$\mathrm{m}^2\,\mathrm{s}^{-1}$
ε_c	$2.25 \cdot 10^6$	$\mathrm{m}^2\,\mathrm{s}^{-1}$
ε_w	$2.25 \cdot 10^6$	$\mathrm{m}^2\,\mathrm{s}^{-1}$
$\varepsilon_{c,adv}$	500	$\mathrm{kg\,m}^{-3}$
$\varepsilon_{w,adv}$	500	$\mathrm{kg\,m}^{-3}$

values close to those of water, (b) values found in other published literature, where the choice of D_a is consistent with [30], and (c) by performing sensitivity analysis using the 1D model, where the parameters giving a best fit between numerical simulations and observations made in [9] were chosen.

The no-flux boundary conditions are given by (2.28), while the physical initial data is

$$P_0 = 101.325\,\mathrm{kPa}, \qquad \rho_{w0} = \frac{P_0}{C_w} + \tilde{\rho}_{w0}, \qquad \rho_{c0} = \frac{P_0}{C_c} + \tilde{\rho}_{c0}$$

Moving over to the dimensionless domain, the initial cell volume fraction is given by the function

$$\alpha_{c0}(x) = 0.7e^{-4000(x-0.5)^2}, \qquad 0 \le x \le 1,$$

and

$$\begin{aligned} a_0(x) &= 0, \\ u_{c0}(x) &= u_{w0}(x) = 0. \end{aligned}$$

5.4 Simulations in 1D

Using the one-dimensional model, we obtain the results for α_c plotted in Fig. 5.2 and for absolute pressure in Fig. 5.3. If we look at the growth in Fig. 5.2, we see that the simulated tumor diameter has reached $\sim$ 140 µm after 17 days, and by day 30 it has further increased to $\sim$ 275 µm, both values relatively close to the reported observations in [9].

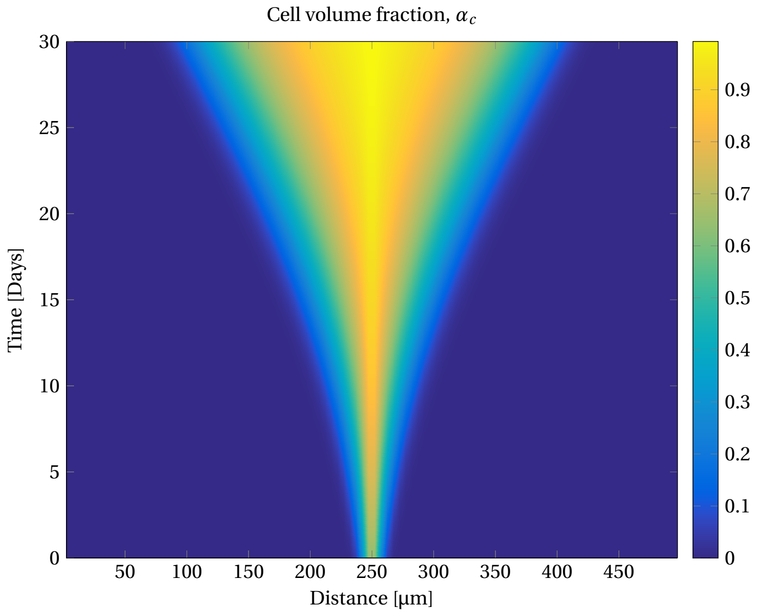

Fig. 5.2. Figure showing the evolution in α_c over a time span of 30 days.

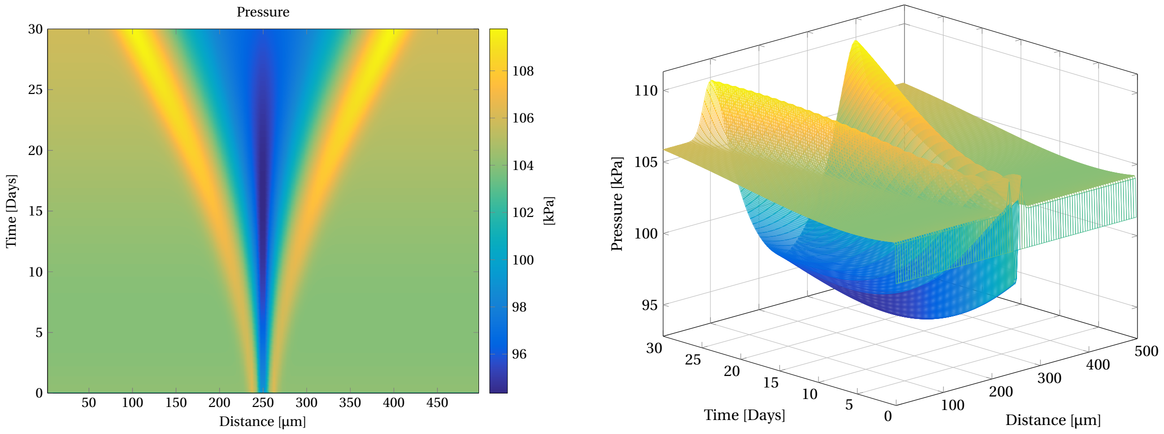

Fig. 5.3. Figures showing the evolution in pressure, visualized in 2D (left) and 3D (right).

Looking at the pressure response in Fig. 5.3, we clearly see a local pressure build-up in the immediate adjacent matrix of the tumor. The pressure value in this zone can at day 30 be read off to ~ 110 kPa, while the surrounding pressure takes a value close to 106 kPa. In other words, the tumor has induced a local pressure that is ~ 4 kPa higher than the surrounding matrix, which is in the same order of magnitude as observed in [9]. Also, the diameter of this zone with increased pressures is ~ 45 µm which also correlates very well with the observations. However, as the initial pressure for the entire domain was set to 101.325 kPa (1 atm), the total pressure increase is actually ~ 9 kPa in the zone closest to the tumor, and ~ 4 kPa in the surrounding matrix, deviating slightly from the observations.

We also note that even though the surrounding pressure increases with time, the cell growth rate keeps increasing, showing no sensitivity to the pressure, which was not the case in [9].

Also worth mentioning, even though it was not measured in [9], is that the pressure within the tumor itself quite rapidly dropped, not only below the values of the surrounding pressures, but also below the initial pressure of 101.325 kPa, before slowly starting to rise towards the end of the simulated period (see Fig. 5.3).

5.5 Simulations in 2D

In 2D, the simulations were run using solution methods II and III, with the same parameters as listed in Table 5.1 and 5.2, while the initial cell volume fraction was given by

$$\alpha_{c0}(x,y) = 0.7e^{-4000\left((x-0.5)^2+(y-0.5)^2\right)}, \qquad 0 \leq x,y \leq 1.$$

5.5.1 Method III

Fig. 5.4 and Fig. 5.5 shows the simulated results for α_c and pressure respectively, using Method III.

We clearly see that the cell growth in figures Fig. 5.4b and 5.4c takes a shape almost identical to that of a square, rotated 45° relative to the boundaries, although by day 30 (Fig. 5.4d) the sides are slightly more rounded. The diameter (measured as the diagonal of the square) is ~ 140 µm after 17 days, and ~ 290 µm after 30 days, and hence the growth rate seems to be slightly higher than for the 1D model (leaving some room for interpretation).

For the pressures in Fig. 5.5 we see the same behavior as for the 1D model, with zones of higher pressures in the close vicinity of the tumor, naturally also taking the shape of a square. Compared to the pressures at day 30 in Fig. 5.3 ranging from ~ 96 to ~ 108 kPa, the pressures in Fig. 5.5c is somewhat lower, ranging from ~ 94 to ~ 106 kPa. Another observation is that the surrounding pressures are lower in areas extending from the corners

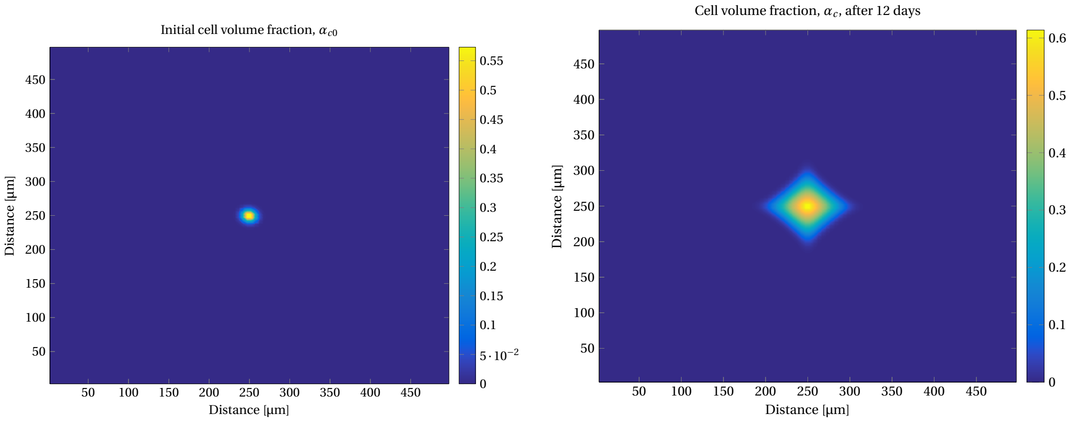

(a) $t = 0$ days **(b)** $t = 12$ days

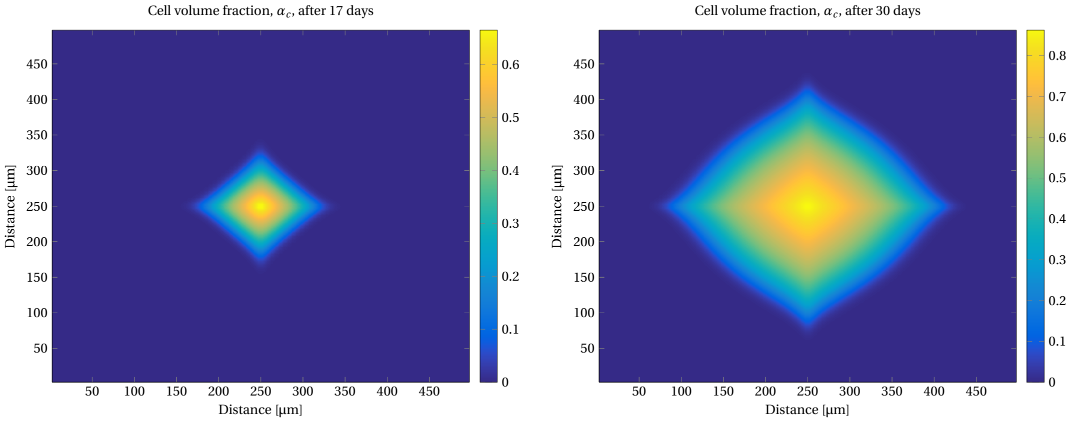

(c) $t = 17$ days **(d)** $t = 30$ days

Fig. 5.4. Figures showing cell migration over a time span of 30 days using Method III.

of the tumor, taking a value of $\sim$ 102 kPa here, while being $\sim$ 104 kPa in the remaining surroundings (values from day 30).

Regarding the pressure inside the tumor, we observe that it keeps decreasing throughout the simulated period, unlike the behavior of the 1D model, where it after some time started to rise.

5.5.2 Method II

Computing the results using Method II, we get the results shown in Fig. 5.6 for α_c and in Fig. 5.7 for the pressures.

We clarely see that α_c evolves much slower in Fig. 5.6 compared to both the 1D model and the 2D model when using Method III, only reaching a diameter of $\sim$ 100 μm after 17

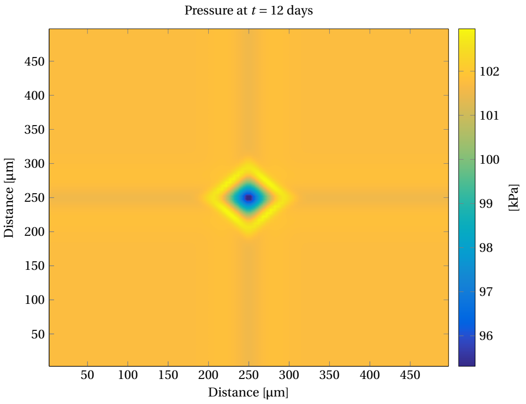

(a) $t = 12$ days

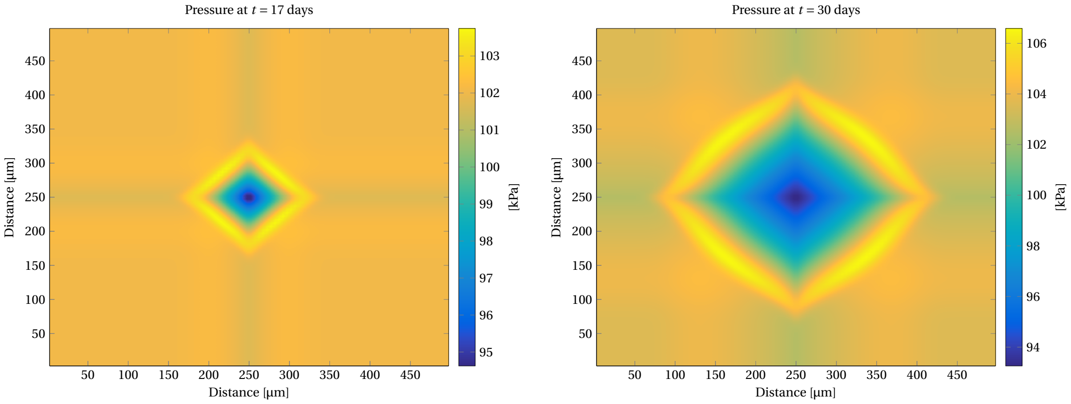

(b) $t = 17$ days **(c)** $t = 30$ days

Fig. 5.5. Figures showing the corresponding pressures after 12, 17, and 30 days using Method III.

days, and ~ 180 µm by day 30. The shape of the tumor is however much more circular than when using Method III, which is as expected based on the results from Chapter 4.

Looking at the pressures in Fig. 5.7, we see exactly the same type of response as for 1D model in Fig. 5.3 and for the 2D model using Method III in Fig. 5.5 with regards to shape and local pressure build-up in a zone close to the tumor. We also note that the pressure distribution seems to be homogeneous in the surrounding matrix, unlike what was observed in Fig. 5.5 using Method III, where the surrounding pressure was lower along the lines $(x, L/2)$ and $(L/2, y)$. In addition, at day 30 the zone with increased pressures only extend ~ 20 µm from the tumor surface, while for the 1D simulations in Fig. 5.3 this zone was approximately 50 µm.

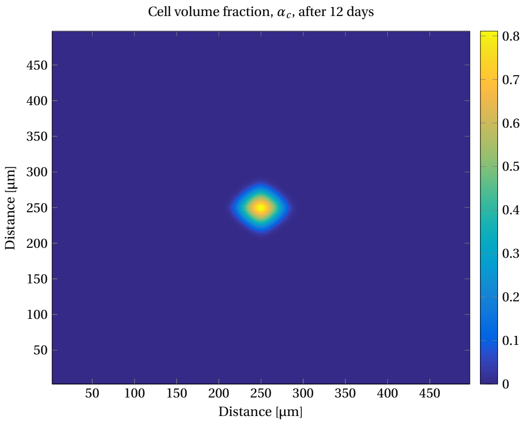

(a) $t = 12$ days.

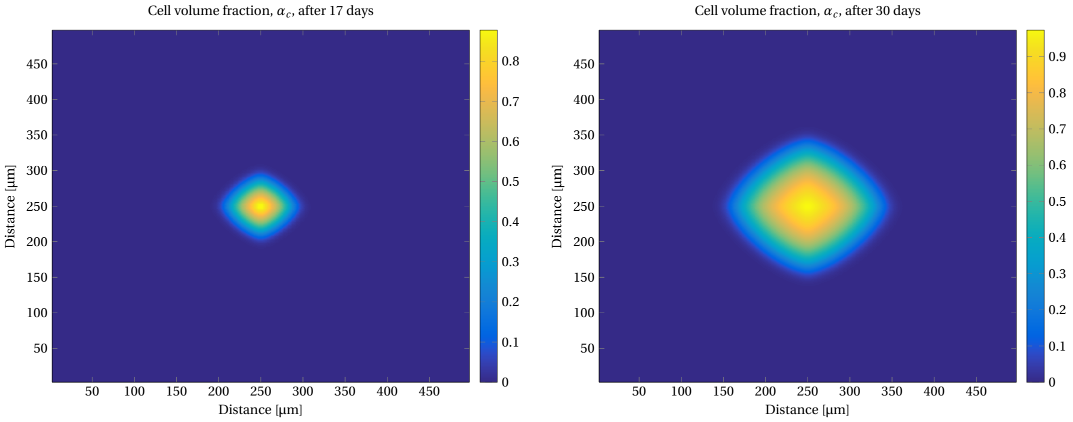

(b) $t = 17$ days.

(c) $t = 30$ days.

Fig. 5.6. Figures showing the evolution in α_c after 12, 17 and 30 days using Method II.

For the internal pressure of the tumor, it has also in this case dropped below values of the surroundings, but similarly to the simulations in 1D, it starts to increase slightly at the end of the simulated period.

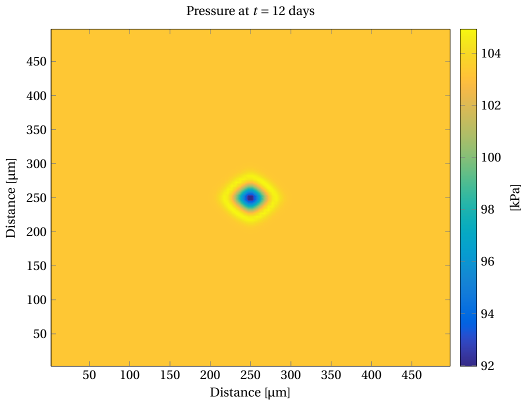

(a) $t = 12$ days.

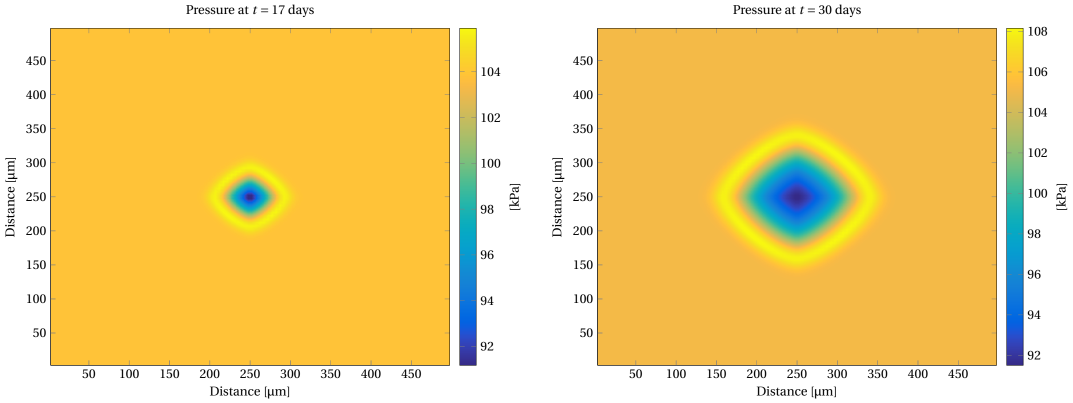

(b) $t = 17$ days.

(c) $t = 30$ days.

Fig. 5.7. Figures showing the corresponding pressures after 12, 17, and 30 days using Method II.

Chapter 6

Discussion

This chapter has been divided into two parts. In the first part we discuss model characteristics based on the observations made in Chapters 3 through 5, while we in the second part take a closer look at the results in Chapter 5, and try to explain some of the observed behavior based on knowledge about the model characteristics.

6.1 Model characteristics

6.1.1 Viscous effects

With regards to viscous effects, one of the observations made when reducing the value of the kinematic viscosities ε_c and ε_w, was that the deformation rate increased. This can be seen in Fig. 4.13 where the values of ε_c and ε_w are of a factor 10 lower than in Fig. 4.12, and as a result, the solution with reduced viscosity (Fig. 4.13) progresses at a much higher rate (a factor ~ 10) than the case with higher viscosity (Fig. 4.12). Both cases were simulated using Method I.

A similar observation was made when running simulations of the base case in Chapter 3, where a steady-state situation was reached at a much earlier stage for the simplified Keller-Segel model in Fig. 3.7 (no viscous effects), compared to the result in Fig. 3.6 for the model in (2.31) (including viscous effects). As already mentioned in Chapter 3, this behavior could be explained by the fact that viscosity itself is a measure of the internal friction opposing deformation of the fluid [2].

Another observation made, was when running simulations with an initial cell volume fraction given by (4.4), using Method I. Here, we experienced that for higher values of ε_c and ε_w the solution more or less took the shape of a square (see Fig. 4.12), but when the viscosity was reduced by a factor 10 however, the solution became more circular (see Fig. 4.13). In other words, reducing the viscosity resulted in a more uniform deformation with respect to spatial directions.

By looking at the components of the stress tensor (see (2.8) and (2.9)), we notice that when reducing the viscosity, the pressure function $P(m,n)$ will become more dominant, along with the function $\Lambda(a)$ (only for the cell phase). As these functions are isotropic, i.e. they do not depend directly on x or y, it might explain to some degree that the evolution of α_c is more uniform with respect to spatial directions when the viscosities are reduced.

The last observation with regards to viscosity, is its effect on the stability properties of the model. By decreasing the viscosity by a factor 10, we had to decrease time step length by a factor ~ 3 for the base case in Chapter 3, in order to avoid that the coefficient matrix for the momentum equations became singular. We also observed that this matrix easily becomes ill-conditioned for a relatively small decrease in either ε_l or $\varepsilon_{l,reg}$ $(l = c, w)$, showing most sensitivity to the regularization parameters. This was also illustrated for the base case in Chapter 3, where we for the 1D model had to reduce the time step length by a factor 10 when reducing $\varepsilon_{l,reg}$ $(l = c, w)$ from 500 to 0, in order to avoid the coefficient matrix from becoming singular (see Fig. 3.8).

6.1.2 Shear stress

Similar to observations in the previous subsection, we observed that when including extra viscous effects in the form of shear stresses, the rate of which the solution changed with time would decrease, compared to when using solution methods where these terms had been neglected, i.e. Method I and Method III. This was illustrated in Section 4.3 where the solution in Fig. 4.12 using Method I developed ~ 1.3 times faster than the solution in Fig. 4.15 where Method II had been used. The explanation for this follows the same reasoning as in the subsection above, where it was stated that since viscosity is a measure of the internal friction opposing deformation of the fluid, an increase in such effects would result in lower deformation rates.

For the case in Section 4.1, we saw that when including shear stresses by using Method II, the shape of the solution did remain more or less constant throughout the simulated period, only varying in size (see Fig. 4.3). When simulating the same case using Method I (no shear stresses), we did however observe that the solution to a much larger extent did change its shape, as seen in Fig. 4.2.

Similar behavior was also observed for the case in Section 4.3 and for the case in Chapter 5, where compared to methods where shear stresses were neglected, the solution using Method II maintained a more circular shape, consistent with that of the initial data.

In order to get more information about whether the observed effects could be attributed to the shear stress terms, or simply were effects introduced by the dimensional splitting approach, we ran a simulation using Method II where the shear stress terms had been zeroed out (see Section 4.3 for details). The results obtained, shown in Fig. 4.16, clearly shows that the solution where shear stresses were neglected takes a more square shape, compared to Fig. 4.15 where shear stresses were included, suggesting that solutions change shape more easily due to the fact that shear stresses are neglected, rather than being an effect induced by the dimensional splitting approach.

Recalling from the previous subsection that the solution evolved more uniformly with respect to spatial directions when reducing the viscosities, i.e. when reducing the term

$$2\varepsilon_c \frac{\partial}{\partial x_i}\left(f\frac{\partial u_l^i}{\partial x_i}\right), \qquad f = m,n,\ l = c,w,$$

using Method I, and in this subsection observing a similar behavior when introducing

$$\varepsilon_c \frac{\partial}{\partial x_i}\left(f\left(\frac{\partial u_l^i}{\partial x_j} + \frac{\partial u_l^j}{\partial x_i}\right)\right), \qquad f = m,n,\ l = c,w,$$

using Method II, indicates that it is the viscous part of the normal stresses, i.e. $2\varepsilon_l \partial_{x_i}\left(f\partial_{x_i}u_l^i\right)$ $(f = n,m,\ l = c,w)$ that to a large extent governs how the solutions will change in shape.

6.1.3 Effect of boundary geometry

In Section 4.2 it was suggested that the boundary geometry might effect the computed solution, even for early stages of the simulated period, due to the fact that the momentum equations are PDEs of elliptic type. Hence, simulations were carried out both in Section 4.2 and in Section 4.3 using Method I, on square and circular domains. For the case in Section 4.2 we clearly see differences between the results in Fig. 4.6 and Fig. 4.8. These differences are to a large extent believed to be caused by the fact that for the results in Fig. 4.6, the non-zero part of the initial data only affected a circular part of the square domain, such that cells could migrate towards corners as seen in Fig. 4.6a, unlike the case in Fig. 4.8, where non-zero initial data was distributed over the entirety of the domain. However, we also noted that even relatively small changes in the initial data gave quite different results, as was illustrated in Fig. 4.6 compared to Fig. 4.10, where for Fig. 4.6 the initial cell volume fraction was distributed over a circular part of the domain, as seen in Fig. 4.5, while it was distributed over the entire square domain as shown in Fig. 4.9, for the result in Fig. 4.10.

For the results in Section 4.3, there were no visible differences whether a square (Fig. 4.12) or circular (Fig. 4.14) domain was used. This suggest that the difference between the solutions in Fig. 4.6 and Fig. 4.10 was a result of α_c being in contact with the boundary, while for cases where the computed solution not comes in direct contact with the boundary, any effect caused by the geometry of the boundary will be negligible.

6.1.4 Solution methods for the 2D model

With respect to solution methods for the 2D model, it was observed that for the base case in Chapter 3, unwanted effects did occur close to the boundary when using Method I (see Fig. 3.11), and it was further suggested that this effect had to do with the inclusion of a correction factor when treating the source term $S_a(a,n)$ (see Section 3.2.2 for details), as this could be considered as the most significant difference between Method I and Method III. However, when using Method I for the cases in Chapter 4, no unwanted effects were observed, suggesting that for situations where most of the changes occur at the interior part of the domain, Method I gives acceptable results.

We would further like to note that any differences between solutions obtained using Method II, and Methods I and III, has in this thesis been attributed to the inclusion of the shear stress terms in Method II, and not due to possible effects introduced by the dimensional splitting approach used in Method I and Method III. The reasoning behind this is that there are not observed any differences between the solution in Fig. 4.16 where Method II without shear stress terms has been used, and the solution in Fig. 4.12 Method I was used.

Based on the observations made in this subsection and the ones above, the use of Method I and Method III should be limited to cases where the viscous effects are low, i.e. cases where ε_c and ε_w are low, in order for any differences between Method II and Methods I and III to become small.

6.2 Observations relative to Chapter 5

6.2.1 Cell volume fraction

For the simulations in Chapter 5, the viscosity parameters had to be chosen large enough in order to avoid numerical instabilities, without having to use an unreasonably large amount of time steps when running simulations. The values chosen by far exceed those of e.g. water, which at 20 °C has a dynamic viscosity of $\sim 10^{-6}\ \mathrm{m^2\,s^{-1}}$ [29]. However, it can be argued that for a gel that also exhibits properties more similar to those of solids (see e.g. [43], where the stiffness properties of, amongst others, 0.5% agarose gel has been measured), the viscosity will be high.

For the simulations in 2D, it was observed that the shape of the solution in Fig. 5.6 is much more square, compared to the solution of the somewhat similar case in Fig. 4.15 (both computed using Method II). A proposed explanation to this, is that the initial data of the solution in Fig. 5.6, plotted in Fig. 5.4a, only affects a very few grid blocks, and as a result, the shape of the initial data is not well defined. By using a finer grid, or by selecting initial data that affects a larger number of grid blocks, a more well defined shape of the initial data could be established, and based on the results in Fig. 4.15, the tumor would grow more uniformly, similar to the experimental results from [9], shown in Fig. 5.1.

With respect to the evolution of α_c, in both 1D and 2D the cells seem to grow at a higher rate along the periphery of the tumor, where the values of α_c are low (see e.g. Fig. 5.2). This behavior is as expected, based on the predictions made in Section 4.3 with respect to the source term $S_c(\alpha_c)$. However, as the tumor growth rate shows no sign of being affected by the increasing pressures (see Fig. 5.3), while Cheng et al. observed a reduction in cell proliferation, and an increase in apoptotic cell death in regions of high mechanical stress in [9], we could argue that the respective source term also should be a function of pressure.

The last observation with respect to α_c, is that when we performed sensitivity analysis using the 1D model for the case in Chapter 5 (in order to select suitable input parameters), we observed that the interfacial friction constant k only had a negligible effect on the growth rate of the cells, compared to the kinematic viscosities. As the phase velocities for the reduced Keller-Segel model, given in (2.49), are functions that depend directly on k, it is not obvious that when introducing viscous effects, that these should become far more dominant than the interfacial friction. In order to illustrate this, a simulations was run using the 1D model with parameters from Table 5.2, only changing the value of k from $k = 10^3$ to $k = 10^{15}$. The corresponding result has then been plotted in Fig. 6.1, where in addition the solution from Chapter 5 has been included for comparison ($k = 10^3$ for that case). As we can see, there are only small differences between the growth rates for $k = 10^3$ (left) and for $k = 10^{15}$ (right), which for the reduced Keller-Segel model would result in phase velocities close to zero.

The question to why this seems to be the case is not entirely clear but we note that in the coefficient matrix for the momentum equations, the parameters ε_c and ε_w are present to a much higher degree in the diagonals than k, as illustrated in Fig. 6.2, where elements containing ε_c or ε_w are marked using crosses, and elements containing k are marked using circles, except for the main diagonal which contains both parameters.

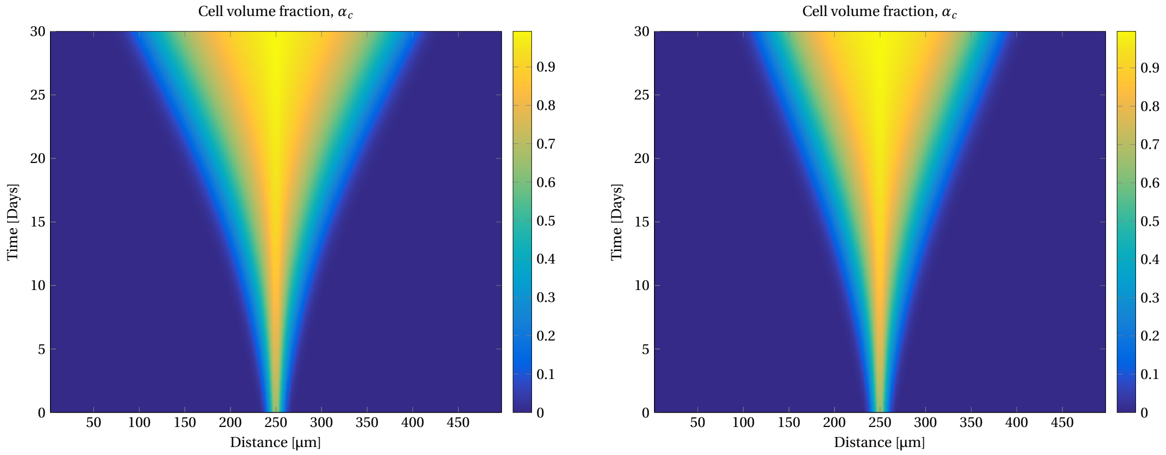

Fig. 6.1. Figures where $k = 10^3$ (left) and $k = 10^{15}$ (right).

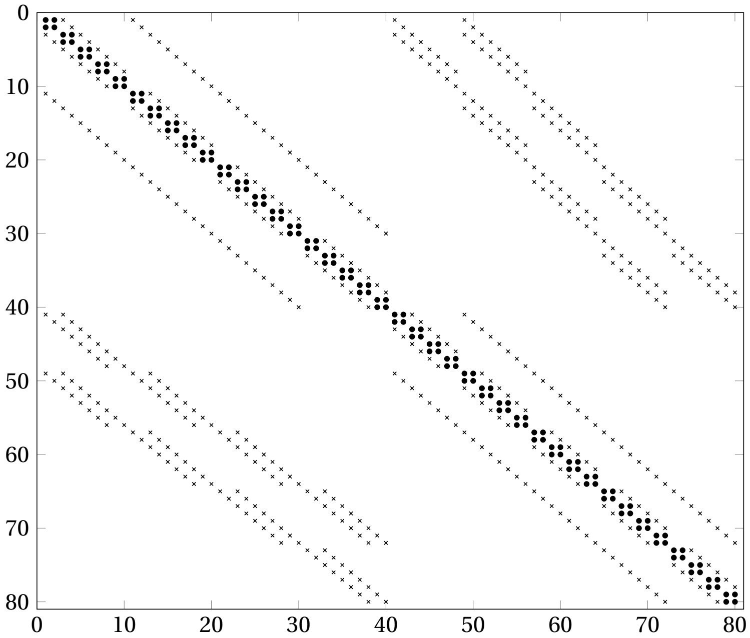

Fig. 6.2. Sparsity pattern of the momentum coefficient matrix, where the crosses represents elements containing ε_c or ε_w, and circles represent elements containing k.

6.2.2 Pressure

With regards to pressures, we note that the compressibility coefficient C_c had to be chosen small in order for the pressures vary in the range of a few kilopascals from the initial data, as was reported in [9].

From physical measurements of cell compressibility conducted in [20] and [48], the compressibility was found to be in the range of $\sim 4 \cdot 10^{-10}$ Pa^{-1}, corresponding to a value of

C_c in the range of $\sim 2.5 \cdot 10^6\ \mathrm{m}^2\,\mathrm{s}^{-2}$ by the use of (2.34) and (2.35), exceeding the chosen value of $C_c = 500\ \mathrm{m}^2\,\mathrm{s}^{-2}$ found in Table 5.2, by far.

Another observation made, was that the simulated pressure distribution takes a similar shape to that of the cell volume fraction (see e.g. Fig. 5.2 and Fig. 5.3). This can be explained by the fact that the equations in (2.30) are coupled, where for instance the pressure is found to be a function depending on phase densities, which again depend on m and n (see Equations (2.38) and (2.43)), while the cell volume fraction is related to n by $\alpha_c = \frac{n}{\rho_c}$ (see Section 2.1).

The last observation made, although not measured in [9], was that the simulated results showed a pressure decrease in the interior of the tumor, which eventually would start to rise towards the end of the simulated period (see Fig. 5.3). The physical interpretation of this behavior is that the tumor grows at a higher rate along the outer periphery, which causes the tumor to stretch. As the tumor is stretched, the density of the tumor will decrease, which again leads to a decrease in pressure, according to (2.38).

Chapter 7

Conclusion

7.1 Concluding remarks

The concluding remarks of this thesis has been summarized in the following points:

- In order for the model behavior to match the experiments in [9], parameters like kinematic viscosity and cell compressibility had to be chosen unrealistically large, and small, respectively, compared to values presented in published literature.
- The use of solution Methods I and III should be limited to cases where the viscous effects are low, in addition to that for Method I, the dynamics of the model should be limited to the interior of the domain, so that unwanted effects close to the boundary are avoided.
- For any case where the cell phase avoids direct contact with the boundary throughout the simulated period (i.e. where $\alpha_c = 0$ close to the boundary for all times), there are no indications that the geometry of the boundary affects the computed solution.
- In addition to being able to generate spatial patterns, the model also shows a high sensitivity to initial data, where only small changes in such data can lead to vastly different results.
- With respect to deformation rates, it is observed that the internal friction, or viscosity, play a much more crucial role than that of the interfacial friction.
- Shear stress is found to act as a resisting force with respect to shape changes in the solutions.
- Regularization parameters are needed in order to avoid very strict limitations on time step length.

7.2 Suggestions for future work

In order to improve the matching between simulated and experimental results, we propose that the source term in (4.6) which governs the growth and death of cells, also should be a function of pressure and not only α_c. The reason for this is that it was observed a reduction in cell proliferation, and an increase in apoptotic cell death in regions of high mechanical stress in [9].

With regards to the choice of rheology model, it was in [17] argued that the choice of identifying the cell phase as a Newtonian fluid was arbitrary, and that other rheology models, e.g. the Bingham model might be more physically correct. Hence, it would be interesting to implement such a rheology model to see if this would further improve the simulated results.

As of now, there are fairly strict limitations on the choice of time step length, so another suggestion is to take measures so that the model will become more flexible with respect to Δt, making the model more practical to work with.

At last, since the migratory behavior of cells also is governed by other mechanisms than chemotaxis and random motion, for example *haptotaxis* and *cell-cell adhesion*, a suggestion is to implement such mechanisms into the mathematical model, in order to see if this will enhance the matching between simulated and experimental results.

References

[1] Alt, W. (1980). Biased random walk model for chemotaxis and related diffusion approximation. *J. Math. Biol.*, 9:147–177.

[2] Batchelor, G. K. (2000). *An Introduction to Fluid Dynamics*. Cambridge University Press.

[3] Bennet, N. T. and Shultz, G. S. (1993). Growth factors and wound healing: Part II role in normal and chronic wound healing. *Am. J. Surgery*, 166:74–81.

[4] Breward, C. J. W., Byrne, H. M., and Lewis, C. E. (2002). The role of cell-cell interactions in a two-phase of solid tumor growth. *J. Math. Biol.*, 45:125–152.

[5] Byrne, H. M., King, J. R., McElwain, D. L. S., and Preziosi, L. (2003). A two-phase model of solid tumor growth. *Appl. Math. Lett.*, 16:567–573.

[6] Byrne, H. M. and Owen, M. R. (2004). A new interpretation of the keller-segel model based on multiphase modelling. *J. Math. Biol.*, 49:604–626.

[7] Byrne, H. M. and Preziosi, L. (2003). Modelling solid tumour growth using the theory of mixtures. *Mathematical Medicine and Biology*, 20:341–366.

[8] Chaplain, M. A. (2000). Mathematical modelling of angiogenesis. *J. Neurooncol.*, 50(1-2):37–51.

[9] Cheng, G., Tse, J., Jain, R. K., and Munn, L. L. (2009). Micro-environmental mechanical stress controls tumor spheroid size and morphology by suppressing proliferation and inducing apoptosis in cancer cells. *PLoS ONE*, 4(2):e4632.

[10] Dallon, J. C. and Othmer, H. G. (1997). A discrete cell model with adaptive signalling for aggregation of dictyostelium discoideum. *Philos. Trans. R. Soc. B*, 352(391-417).

[11] Dormann, D. and Weijer, C. J. (2006). Chemotactic cell movement during Dictyostelium development and gastrulation. *Curr. Opin. Genet. Dev.*, 16(4):367–373.

[12] Drew, D. A. and Segel, L. A. (1971). Averaged equations for two-phase flows. *Studies in applied mathematics*, 50(3):205–231.

[13] Eisenbach, M. (2004). *Chemotaxis*. Imperial College Press, London.

[14] Evje, S. and Flåtten, T. (2003). Hybrid flux-splitting schemes for a common two-fluid model. *J. Comput. Phys.*, 192(1):175–210.

[15] Evje, S. and Wen, H. (2015a). Analysis of a compressible two-fluid Stokes system with constant viscosity. *J. Math. Fluid Mech.*, 17(3):423–436.

[16] Evje, S. and Wen, H. (2015b). Stability of a two-fluid model for cell migration.

[17] Fasano, A., Bertuzzi, A., and Sinisgalli, C. (2014). *Conservation Laws in Cancer Modeling*, pages 27–61. Springer Science and Business Media.

[18] Fjær, E., Holt, R. M., Horsrud, P., Raaen, A. M., and Risnes, R. (2008). *Petroleum Related Rock Mechanics*. Elsevier, 2nd edition.

[19] Folkman, J. and Brem, H. (1992). *Angiogenesis and inflammation. In: Inflammation: Basic Principles and Clinical Correlates. Second Edition.* Raven Press.

[20] Hartono, D., Liu, Y., Tan, P. L., Then, X. Y. S., Yung, L.-Y. L., and Lim, K.-M. (2011). On-chip measurements of cell compressibility via acoustic radiation. *Lab Chip*, 11(23):4072–4080.

[21] Hildebrand, E. and Kaupp, U. B. (2005). Sperm chemotaxis: a primer. *Annals of the New York Academy of Sciences*, 1061(1):221–225.

[22] Hillen, T. and Othmer, H. G. (2000). The diffusion limit of transport equations derived from velocity jump processes. *SIAM J. Appl. Math.*, 61(3):751–775.

[23] Hillen, T. and Painter, K. J. (2009). A user's guide to PDE models for chemotaxis. *J. Math. Biol.*, (58):183–217.

[24] Horstmann, D. (2003). From 1970 until present: the Keller–Segel model in chemotaxis and its consequences. *I. Jahresberichte DMV*, 105(3):103–165.

[25] Jabbarzadeh, E. and Abrams, C. F. (2005). Chemotaxis and random motility in unsteady chemoattractant fields: a computational study. *J. Theor. Biol.*, 235(2):221–232.

[26] Jackson, T. L. and Byrne, H. M. (2002). A mechanical model of tumor encapsulation and transcapsular spread. *Math. Biosci.*, 180:307–328.

[27] Keller, E. F. and Segel, L. A. (1970). Initiation of slime mold aggregation viewed as an instability. *J. Theoret. Biol.*, (26):399–415.

[28] Keller, E. F. and Segel, L. A. (1971). Model for chemotaxis. *J. Theoret. Biol.*, 30:225–234.

[29] Kestin, J., Sokolov, M., and Wakeham, W. A. (1978). Viscosity of liquid water in the range -8°C to 150°C. *J. Phys. Chem. Ref. Data*, 7(3):941–948.

[30] Kim, Y., Lawler, S., Nowicki, M. O., Chiocca, E. A., and Friedman, A. (2009). A mathematical model for pattern formation of glioma cells outside the tumor spheroid core. *J. Theoret. Biol.*, 260:359–371.

[31] Kirby, B. J. (2010). *Micro- and Nanoscale Fluid Mechanics: Transport in Microfluidic Devices*. Cambridge University Press.

[32] Landau, L. D. and Lifshitz, E. M. (1987). *Fluid Mechanics*, volume 6 (Course of Theoretical Physics). 2nd edition.

[33] LeVeque, R. J. (2002). *Finite Volume Methods for Hyperbolic Problems*. Cambridge University Press.

[34] Mantzaris, N. V., Webb, S., and Othmer, H. G. (2004). Mathematical modeling of tumor-induced angiogenesis. *J. Math. Biol.*, 49(2):111–187.

[35] Maree, A. F. and Hogeweg, P. (2001). How amoeboids self-organize into a fruiting body: multicellular coordination in dictyostelium discoideum. *Proc. Natl. Acad. Sci. USA*, 98(7):3879–3883.

[36] Mittal, N., Budrene, E. O., Brenner, M., and A. Van Oudenaarden, A. (2003). Motility of *Escherichia coli* cells in clusters formed by chemotactic aggregation. *Proc. Natl. Acad. Sci. USA*, 100(23):13259–13263.

[37] Othmer, H. G. and Stevens, A. (1997). Aggregation, blowup and collapse: The ABC's of taxis in reinforced random walks. *SIAM J. Appl. Math.*, 57:1044–1081.

[38] Owen, M. R. and Sherratt, J. A. (1997). Pattern formation and spatiotemporal irregularity in a model for macrophage-tumour interactions. *J. Theor. Biol.*, 189(1):63–80.

[39] Palsson, E. and Othmer, H. G. (2000). A model for individual and collective cell movement in Dictyostelium discoideum. *Proc. Natl. Acad. Sci. USA*, 97(19):10448–10453.

[40] Park, H. T., Wu, J., and Rao, Y. (2002). Molecular control of neuronal migration. *Bioessays*, 24(9):821–827.

[41] Patlak, C. S. (1953). Random walk with persistence and external bias. *Bull. Math. Biophys.*, 15:311–338.

[42] Perumpanani, A. J., Sherratt, J. A., Norbury, J., and Byrne, H. M. (1996). Biological inferences from a mathematical model for malignant invasion. *Invas. Metastas.*, 16(4-5):209–221.

[43] Scandiucci de Freitas, P., Wirz, D., Stolz, M., Göpfert, B., Friederich, N.-F., and Daniels, A. U. (2006). Pulsatile dynamic stiffness of cartilage-like materials and use of agarose gels to validate mechanical methods and models. *J. Biomed. Mater. Res. B. Appl. Biomater.*, 78:347–357.

[44] Sonin, A. A. (2001). *Equation of Motion for Viscous Fluids*. Massachusetts Institute of Technology, 8th edition.

[45] Stevens, A. (2000). The derivation of chemotaxis-equations as limit dynamics of moderately interacting stochastic many particle systems. *SIAM J. Appl. Math.*, 61(1):183–212.

[46] Tranquillo, R. T., Lauffenburger, D. A., and Zigmond, S. H. (1988). A stochastic model for leukocyte random motility and chemotaxis based on receptor binding fluctuations. *J. Cell Biol.*, 106(2):303–309.

[47] Tyson, R., Stern, L. G., and LeVeque, R. J. (2000). Fractional step methods applied to a chemotaxis model. *J. Math. Biol.*, 41:455–475.

[48] Wang, H., Liu, Z., Shin, D. M., Chen, G., Cho, Y., Kim, Y.-J., and Han, A. (2013). Acoustophoretic force-based compressibility measurement of cancer cells having different metastatic potential. *J. Acoust. Soc. Am.*, 133:3280.

[49] Ward, J. P. and King, J. R. (1997). Mathematical modelling of avascular-tumour growth. *IMA. J. Math. Appl. Med.*, 14:39–69.

[50] Wikipedia (2016a). Logistic function. https://en.wikipedia.org/wiki/Logistic_function. Accessed: 14 Jun 2016.

[51] Wikipedia (2016b). Stress (mechanics). https://en.wikipedia.org/wiki/Stress_(mechanics). Accessed: 14 Jun 2016.

[52] Wu, D. (2005). Signaling mechanisms for regulation of chemotaxis. *Cell Res.*, 15(1):52–56.